Portable Electromagnetic Induction Sensor with Integrated Positioning

MR-1712

Final Report

Submitted to

Strategic Environmental Research and Development Program (SERDP)

August 20, 2013

Revision **2.0**

By

U.S. Army Corps of Engineers Research and Development Center
Cold Regions Research and Engineering Laboratory (CRREL)
72 Lyme Road
Hanover, NH 03755

Principal Investigators
Drs. Ben Barrowes, David George, and Fridon Shubitidze
benjamin.e.barrowes@usace.army.mil

REPORT DOCUMENTATION PAGE

Form Approved
OMB No. 0704–0188

The public reporting burden for this collection of information is estimated to average 1 hour per response, including the time for reviewing instructions, searching existing data sources, gathering and maintaining the data needed, and completing and reviewing the collection of information. Send comments regarding this burden estimate or any other aspect of this collection of information, including suggestions for reducing this burden to Department of Defense, Washington Headquarters Services, Directorate for Information Operations and Reports (0704–0188), 1215 Jefferson Davis Highway, Suite 1204, Arlington, VA 22202–4302. Respondents should be aware that notwithstanding any other provision of law, no person shall be subject to any penalty for failing to comply with a collection of information if it does not display a currently valid OMB control number. **PLEASE DO NOT RETURN YOUR FORM TO THE ABOVE ADDRESS.**

1. REPORT DATE *(DD–MM–YYYY)*	2. REPORT TYPE	3. DATES COVERED *(From — To)*
06–25–2013	Final	05 January 2010 — 20 February 2013

4. TITLE AND SUBTITLE

Portable Electromagnetic Induction Sensor with Integrated Positioning

5a. CONTRACT NUMBER

W74RDV93148318

5b. GRANT NUMBER

5c. PROGRAM ELEMENT NUMBER

6. AUTHOR(S)

Barrowes, Benjamin E., George, David, and Shubitidze, Fridon

5d. PROJECT NUMBER

MR-1712

5e. TASK NUMBER

5f. WORK UNIT NUMBER

7. PERFORMING ORGANIZATION NAME(S) AND ADDRESS(ES)

U.S. Army Corps of Engineers, Engineer Research and Development Center
Cold Regions Research and Engineering Laboratory (CRREL)
72 Lyme Road
Hanover, NH 03755

8. PERFORMING ORGANIZATION REPORT NUMBER

9. SPONSORING / MONITORING AGENCY NAME(S) AND ADDRESS(ES)

SERDP Program Office
4800 Mark Center Drive, Suite 17D08
Alexandria, VA 22350-3605
(571) 372-6565

10. SPONSOR/MONITOR'S ACRONYM(S)

11. SPONSOR/MONITOR'S REPORT NUMBER(S)

12. DISTRIBUTION / AVAILABILITY STATEMENT

Approval for public release; distribution is unlimited.

13. SUPPLEMENTARY NOTES

The views, opinions and/or findings contained in this report are those of the authors and should not be construed as an official U.S. Government position, policy or decision, unless so designated by other documentation.

14. ABSTRACT

SERDP project MR-1712 entitled "Portable Electromagnetic Induction Sensor with Integrated Positioning" is complete. This report contains the final design, engineering challenges, modeling advancements, data analysis, and results from Aberdeen Proving Ground tests which resulted from this project. The instrument developed under this project is call Pedemis (PortablE Decoupled Electromagnetic Induction Sensor). The instrument was conceived of as a sensor which combined the advantages of both the larger cart mounted sensors and the smaller handheld sensors. Pedemis is transported by one or two people and has nine transmitters and nine triaxial receivers with the receiver array being physically decoupled from the transmitter array leading to deployment and operational flexibility. The controlling electronics of Pedemis are lighter and more efficient than prior advanced electromagnetic induction instruments. We applied the Orthonormalized Volume Magnetic Source method (ONVMS) technique and the Joint Diagonalization (JD) method to data acquired with Pedemis at Aberdeen proving ground. Aberdeen Proving Ground blind grid results are better than any previous results from any group and instrument at APG.

15. SUBJECT TERMS

keywords; electromagnetic induction, multiple targets, rigorous models, inversion, dipole model, joint diagonalization, ONVMS, multitarget, time domain

16. SECURITY CLASSIFICATION OF:			17. LIMITATION OF ABSTRACT	18. NUMBER OF PAGES	19a. NAME OF RESPONSIBLE PERSON
a. REPORT	b. ABSTRACT	c. THIS PAGE			Benjamin E. Barrowes
U	U	U	UU	181	19b. TELEPHONE NUMBER *(include area code)* (603)646-4822

Contents

1 Abstract **iii**
1.1 Objectives . . . iii
1.2 Technical Approach . . . iii
1.3 Results . . . iii
1.4 Benefits . . . iv

2 Objective **1**

3 Background **5**

4 Materials and Methods **10**
4.1 Pedemis Design . . . 10
4.1.a Pedemis Tx Array . . . 11
4.1.b Pedemis Rx Array . . . 17
4.1.c Pedemis Control Electronics . . . 19
4.2 Completed Pedemis Instrument . . . 21
4.3 Pedemis Rx Positioning . . . 25
4.3.a General Rx Array Positioning . . . 25
4.3.b Positioning Based on Mutual Inductance . . . 28
4.4 Background Subtraction . . . 43
4.5 Pedemis Operation Protocol . . . 45
4.6 ONVMS Applied to Pedemis . . . 50
4.6.a Pedemis and ONVMS Modeling . . . 52
4.6.b ONVMS Modeling Results . . . 54

5 Results and Discussion **55**
5.1 Pedemis DAQ Control Software . . . 55
5.2 Initial Data, November 2011 . . . 57
5.3 Hardware Challenges . . . 62
5.4 APG Deployment . . . 69
5.4.a Data Protocol and Acquisition at APG . . . 69
5.4.b APG Background and Site Description . . . 74
5.4.c APG Objectives . . . 78
5.4.d Data Analysis plan . . . 84
5.4.e APG Results . . . 86

6 Conclusion **101**

References **102**

APPENDICES

A Supporting Data **107**
A.1 G&G Sciences, Inc. Final Report . . . 107

B List of Scientific/Technical Publications **121**

C Other Supporting Materials **121**
C.1 Official APG Results 121

D Outbrief Slides **138**

1 Abstract

SERDP project MR-1712 entitled "Portable Electromagnetic Induction Sensor with Integrated Positioning" is complete. This report contains the final design, engineering challenges, modeling advancements, data analysis, and results from Aberdeen Proving Ground tests which resulted from this project.

1.1 Objectives

The objective of this work was to design and fabricate a novel time-domain bistatic advanced EMI sensor that allowed for the physical decoupling of the transmitter (Tx) and receiver (Rx) coil(s). This bistatic, physically decoupled, portable EMI instrument with precise positioning became a valuable research instrument for several reasons. First, there was a pressing need for portable EMI instruments deployable in adverse conditions where cart mounted systems could not function. Furthermore, a bistatic EMI instrument would deliver critical flexibility in operation and high fidelity data by allowing users to acquire sufficiently detailed data in one pass to satisfy inversion/discrimination routines. necessary in achieving this data quality was research into a more precise scheme for positioning the receiver assembly. We aimed to combine systematic modeling of the instrument geometry, flexible operation design, and highly precise positioning into a single, portable EMI instrument.

1.2 Technical Approach

This multimode bistatic portable array instrument, called Pedemis (PortablE Decoupled Electromagnetic Induction System), fulfillled these objectives based on research into the optimal size, constitution, and configuration of transmitters, receivers, and supporting hardware while also incorporating several improvements over existing sensors (Sec. 4.1). This new positioning method adds to the information content of the data, allowing more accurate inversions, without adding any hardware to the instrument itself. We incorporated instrument control software which can deliver some feedback to the operator regarding targets in real time (see Sec. 5.1). As well, the flexible operation of this instrument allows deployment in both cart-trafficable sites and more challenging sites.

1.3 Results

A photograph of the completed Pedemis sensor is shown in Fig. 4.10(a) showing the independent transmitter (Tx) and receiver (Rx) arrays. The coplanar 3×3 array of square coil transmitters is visible through the plastic cover, producing a total sensor size of about 121.5 cm $\times$ 121.5 cm. The square Rx array, with a side of about 56 cm, is shown in the top-left position with a vertical non-metallic handle meant to facilitate maneuverability. The sensor is here shown in a laboratory setting, mounted on sawhorses with a UXO underneath. In the field, poles are attached to the the front and back carrying straps for carrying by two operators during dynamic data collection as shown in Fig. 4.10(b). For static data collection Pedemis is laid on the ground and not carried (see Fig. 4.10(c)). The Tx and Rx arrays are schematically represented in Fig. 4.11, with the receivers also arranged in a 3×3 configuration with 20 cm center-to-center spacing. Each receiver

is a triaxial receiver similar to those on the MPV2 [1]. The default dataset is therefore composed of 9 transmitters $\times$ 9 receivers $\times$ 3 components, or 243 time signatures recording the secondary magnetic field between 100 μs and 25 ms.

Pedemis uses the National Instrument cDAQ and a small mini-pc for controlling the Tx and Rx arrays and associated circuitry. This represents a step forward from prior portable EMI systems like the MPV-II in terms of weight, power usage, and decreased complexity. The weight of the cDAQ chassis and modules is around 8 pounds compared to over 20 pounds for the full PXI chassis and related electronics. Instead of 3 lithium ion batteries and 3 hour swap intervals, we use only 2 of these batteries with a 5-6 hour swap interval. Also, the cDAQ chassis, with its integrated modules, is simpler and more robust than the prior full PXI chassis. The combined weight of the transmitter and receiver arrays is about 38 pounds (not including cabling or gurney poles) whereas the overall weight of the controlling electronics plus batteries is approximately 20 pounds.

Pedemis was deployed to Aberdeen Proving Ground UXO test site in November, 2012. Using Pedemis and data processing, we achieved the best score to date on the blind grid.

1.4 Benefits

Pedemis has been fabricated, tested, and deployed over the course of SERDP project MR-1712. Pedemis is a flexible platform that is man-portable, but also acquires high quality data is several interrogation modes. Specifically, Pedemis has the following advantages over other advanced EMI instruments:

- Potential one pass solution
- Hardware
  - 2-person portable design
  - Flexible (2-person portable, carted, sledded)
  - 1.2x1.2m, 3x3 Tx, 3x3 vector Rx (compromise between 2 and 5)
  - decoupled Rx (data diversity, spatial coverage)
  - Lighter, updated electronics
  - Integral positioning system
  - GPS and digital compass
  - Wide swath width and spatial coverage
- Software and processing
  - Real-time feedback to expert operators (field plots, arrows, and JD)
  - Data suited to advanced models (JD, ONVMS, MUSIC)
  - Flexible DAQ modes (detection, interrogation, deep detection, wide interrogation)
  - EM3D or LabVIEW interface

Results at Aberdeen Proving Ground demonstrated the capability of Pedemis to interrogate unknown anomalies. Pedemis is a new, advanced, EMI instrument with several deployment modes, data acquisition flexibility, lighter and less power hungry electronics, and achieves excellent results at standardized sites.

List of Acronyms (and page references to first use)

APG	Aberdeen Proving Ground – first used on page (1)
ATC	Aberdeen Test Center – first used on page (78)
BUD	Berkeley UXO Discriminator – first used on page (6)
CIM	cued interrogation mode – first used on page (25)
CRREL	Cold Regions Research and Engineering Lab – first used on page (1)
EMI	Electromagnetic Induction – first used on page (iii)
EMI	Electromagnetic Induction – first used on page (1)
ERDC	Engineering Research and Development Center – first used on page (1)
ESTCP	Environmental Security Technology Certification Program – first used on page (8)
FPGA	Field Programmable Gate Array – first used on page (55)
JD	Joint Diagonalization – first used on page (1)
MAS	Method of Auxiliary Sources – first used on page (16)
MPV	Man-Portable Vector – first used on page (2)
MR	Munitions Response – first used on page (iv)
NSMS	Normalized Surface Magnetic Source – first used on page (4)
ONVMS	Orthonormalized Volume Magnetic Source – first used on page (1)
Pedemis	PortablE Decoupled Electromagnetic Induction Sensor – first used on page (1)
RMS	Root Mean Squared – first used on page (8)
RT	Real Time – first used on page (55)
SERDP	Strategic Environmental Research and Development Program – first used on page (iv)
SNR	Signal-to-noise ratio – first used on page (8)
TEMTADS	Time domain ElectroMagnetic Towed Array Detection System – first used on page (3)
USACE	United States Army Corps of Engineers – first used on page (1)
VI	Virtual Instruments – first used on page (55)

Keywords: electromagnetic induction, handheld, time domain, rigorous models, inversion

Acknowledgments: This project was funded by the Strategic Environmental Research and Development Program (SERDP) under project MR-1712. We worked closely with G&G Sciences and Dartmouth College for the duration of the project. Drs. Jeff Marqusee, Anne Andrews, and Herb Nelson, and the review committee for SERDP, provided support and constructive reviews during the course of the project.

List of Figures

2.1 Pedemis Design 2
3.1 Examples of challenging terrain for which Pedemis could be deployed. 7
4.1 Pedemis Tx array 12
4.2 Pedemis Rx array 13
4.3 Pedemis control electronics 14
4.4 Possible design of Tx array. 15
4.5 Simulated 2x2 Tx array results 17
4.6 Simulated 3x3 + 4vertical Tx array results 18
4.7 Simulated 3x3 Tx array results 19
4.8 Pedemis receiver cubes 20
4.9 Pedemis control electronics 21
4.10 The Pedemis sensor in both laboratory and field settings. Total weight of the Tx and Rx arrays is 38 pounds, while the total weight for the backpack is 20 pounds. 23
4.11 Schematic representation of the Pedemis sensor. 24
4.12 Pedemis beacon example 26
4.13 Pedemis beacon example error 27
4.14 Pedemis beacon target induced error 28
4.15 Pedemis Beacon Inversion #1 29
4.16 Pedemis Beacon Inversion #2 32
4.17 Integration Comparison - Vertical Trajectory 33
4.18 Integration Comparison - Horizontal Trajectory 34
4.19 Geometry for (4.3.4). 35
4.20 Pairs of filaments 39
4.21 Data collection with Pedemis at the Aberdeen Proving Ground. Shown are two instances of static measurements taken at Position 2 (left) and Position 4 (right). 40
4.22 APG static measurement #00236: The program suggests Gate #7 (1324 µs) and predicts the Rx to be at Position 1. 40
4.23 APG static measurement #00237: The program suggests Gate #5 (826 µs) and predicts the Rx to be at Position 2. 41
4.24 APG static measurement #00238: The program suggests Gate #6 (1046 µs) and predicts the Rx to be at Position 3. 41

4.25 APG static measurement #00239: The program suggests Gate #6 (1046 µs) and predicts the Rx to be at Position 4. 42
4.26 APG static measurement #00240: The program suggests Gate #6 (1046 µs) and predicts the Rx to be at Position 5. 42
4.27 Pedemis Rx guides 43
4.28 Pedemis DAQ Position #1 46
4.29 Pedemis CIM2 Positions 47
4.30 Pedemis time domain waveform 49
4.31 Data acquisition flowchart for Pedemis operation. 50
4.32 Detection configuration 51
4.33 ONVMS model compared to Pedemis data 53
4.34 ONVMS-modeled (left) and measured (right) PEDEMIS data for a four inch diameter sphere at the 10th time channel. First row for Hy and second row for Hx magnetic fields. The sphere is placed at a depth of 36 cm to the PEDEMIS Tx array. 54
5.1 Pedemis RT control software 56
5.2 Pedemis FPGA control software 57
5.3 Initial Data Setup 58
5.4 Example data from Pedemis 60
5.5 Polarizabilities from data in Fig. 5.4. 61
5.6 81mm example setup 62
5.7 Example of “on” time data. 63
5.8 Example of “off” time data. 64
5.9 Example of “on” time bad data. 65
5.10 Example of unstable Tx currents. 66
5.11 Example of stable Tx currents. 67
5.12 Pedemis data residuals 68
5.13 Pedemis at the mogul area at APG. 69
5.14 Real-time arrow display from EM3D 70
5.15 JD of Pedemis dynamic data 71
5.16 CIM2 data acquisition 72
5.17 CIM 3, position 1 72
5.18 CIM 3, position 4 73
5.19 Map of APG USO Test Site 77
5.20 The vertical field strength of 6 different systems studied, measured as a function of depth beneath the center of the loops. . . . 81

5.21 Reporting Template for APG Blind Grid. 86
5.22 Reporting Template for APG Indirect Fire Area. 86
5.23 APG target comparison 90
5.24 APG detection results 92
5.25 APG detection stage results ROC curve. 93
5.26 Results for the blind grid for Pedemis at APG in November, 2012. Note that results numbers in the lower half of the table are one line too low. 94
5.27 APG discrimination stage results ROC curve. 95
5.28 APG classification results by ordnance type. 95
5.29 APG location error, mean and standard deviation. 96
5.30 TONVMS results for 81mm, 60mm, 37mm, and 25mm ordnance in the blind grid at APG. 96
5.31 TONVMS results for 105mm HE and 105mm HEAT ordnance in the blind grid at APG. 97
5.32 APG IDF detection contour map 98
5.33 APG IDF data shots 99
5.34 APG mogul data shots 100

List of Tables

1 Layout descriptions at APG as of August 2012. 76
2 Planned schedule of activities for the APG Pedemis test, Summer-Fall 2012 80
3 Errors in predicted positions for up to five targets simultaneously present under the Pedemis sensor. 88

2 Objective

The objective of this work was to design and fabricate a novel time-domain bistatic advanced EMI sensor that allowed for the physical decoupling of the transmitter (Tx) and receiver (Rx) coil(s). This bistatic, physically decoupled, portable EMI instrument with precise positioning became a valuable research instrument for several reasons. First, there was a pressing need for portable EMI instruments deployable in adverse conditions where cart mounted systems could not function. Furthermore, a bistatic EMI instrument would deliver critical flexibility in operation and high fidelity data by allowing users to acquire sufficiently detailed data in one pass to satisfy inversion/discrimination routines (see Sec. 4.5). Necessary in achieving this data quality was research into a more precise scheme for positioning the receiver assembly. We aimed to combine systematic modeling of the instrument geometry, flexible operation design, and highly precise positioning into a single, portable EMI instrument.

This bistatic configuration allowed greater positioning accuracy, improved depth detection, deployment flexibility, and deployment in difficult terrain. This sensor now has a built-in precise positioning system, can be operated in either a carted or man-portable mode, and features an array of vector (coil) receivers. Figure 2.1 provides a sketch of the design for the instrument which we call Pedemis.

In summary, the sensor consists of a movable coplanar set of transmitting coils, a movable detachable array of receiver coils, and supporting hardware (e.g. in a backpack, see see Sec. 4.1). The system can be used in either a bistatic mode, i.e. with Tx and Rx physically decoupled; or in a monostatic mode (Tx and Rx in a fixed geometry). Subcentimeter or even submillimeter positioning of the receivers has been achieved via receiver cube detection of the primary field during the "on" time of the transmitter (see Sec. 4.3 and Sec. 4.5). Transmitter and receiver geometries and characteristics were rigorously modeled in an effort to systematically determine optimal instrument configurations (see Sec. 4.1).

The specific objectives of this project are:

1. **Modeling of physically decoupled EMI instrument configurations (see Sec. 4.1)**
   We fabricated a bistatic instrument with the Tx and Rx coils physically decoupled and separately movable. This decoupling allows simpler data processing for some algorithms, while simultaneously allowing multiple operational modes (see Sec. 4.1), but will require precise positioning (see Sec. 4.3).

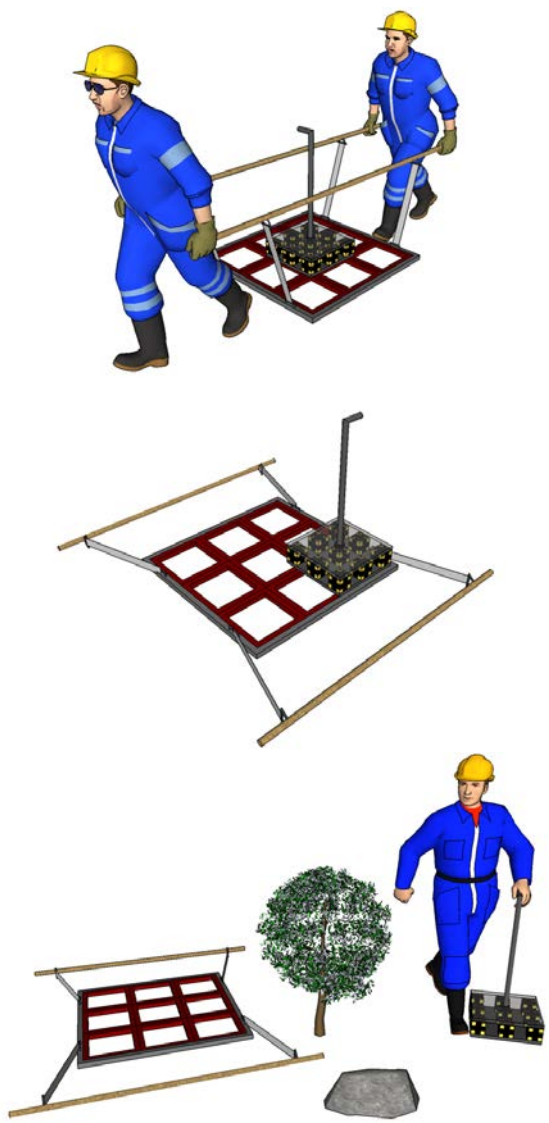

Figure 2.1: Pedemis design. Flexible modes of operation allow either cart mounted or man portable operation, static or dynamic data acquisition. This bistatic configuration allows greater positioning accuracy, improved depth detection, and deployment in difficult terrain. The nine red squares correspond to the Tx coils, while the receiver array is located on top of the Tx coils in the top figure.

The number, geometry, and arrangement of both the transmitters and receivers have been rigorously modeled and investigated with tools from prior SERDP projects for maximum data information given hardware constraints. The receivers are dB/dt vector coil receivers with a lighter core than those of the MPV (MR1443).

2. **Versatile instrument with multiple operational modes**

This instrument has two separate components: a square planar transmitting array consisting of nine coplanar 40cm TEMTADS size Tx coils, and a detachable 3x3 array of vector receivers which can be either placed to collect static data or moved around above the transmitting coils to obtain dynamic data (see Fig. 2.1). Both of these components can be affixed to a cart for larger scale detection surveys, or can be dismounted from the cart and carried by two people in a gurney like configuration for cued interrogation even in rugged and/or challenging terrain. In summary, the following operational modes were considered and evaluated during this project:

(a) Carted Mode (relative geometry fixed)

(b) Cued Interrogation Mode (receivers detached, transmitters stationary [with or without cart])

(c) Man-Portable Detection Mode

3. **Integrated positioning system (see Sec. 4.3)**
To use data from bistatic instruments, the local position of the sensor must be known with as high precision as possible. To this end, a novel beacon positioning system has been implemented into this instrument with the goal of attaining subcentimeter (possibly submillimeter) level positioning of the receiver coil assembly relative to the transmitters. The receivers detect the primary magnetic field during the "on" time of the (stationary) transmitter. Combining and averaging the data from each of the transmitters allows precise positioning of the receiver cubes by detecting the powerful and well known primary fields. These same receiver cubes collect EMI data during the transmitter "off" time.

This multimode bistatic portable array instrument, called Pedemis (PortablE Decoupled Electromagnetic Induction System), fulfillled these objectives based on research into the optimal size, constitution, and configuration of transmitters, receivers, and supporting hardware while also incorporating several improvements over existing sensors (Sec. 4.1). This new positioning method adds to the information content of the data, allowing more accurate inversions, without adding any hardware to the instrument itself. We incorporated instrument control software which can deliver some feedback to the operator regarding targets in real time (see Sec. 5.1). As well, the flexible operation of this instrument allows deployment in both cart-trafficable sites and more challenging sites.

Standard models such as the dipole model [2] and more rigorous models such as the Joint Diagonalization (JD) method [3], Orthonormalized Volume Magnetic Source Method (ONVMS, see Sec. 4.6) [4–6], NSMC [7–15], and analytical models [16–22] were applied to the data acquired from this instrument (Sec. 5.2). These models, in tandem with the diverse, extremely high quality data from this instrument resulted in more accurate discrimination capability and fewer false alarms at our deployment to Aberdeen Proving Ground (see Sec. 5.4).

The new Pedemis instrument is designed to attack successfully the task of close interrogation of signal anomalies, for discriminating UXO from clutter, in non-trafficable, rugged terrain.

3 Background

The identification of buried unexploded ordnance (UXO) and its discrimination from harmless clutter constitute a challenging problem that requires sophisticated sensing instruments[23, 24] and careful data modeling. In the Unites States alone, more than eleven million acres of land and many underwater sites are contaminated with the decades long remediation cost in the ten's of billions of dollars[25]. A wide range of different sensing technologies is being used or is in development for detecting and discriminating UXOs. Among these technologies, metal detectors have been identified as one of most promising technologies for detection as well as classification of subsurface metallic objects. There are two types of metal detectors. One, that is called magnetometers, detects anomalies in the earth's magnetic field caused by ferrous (iron-based) objects[26, 27]. The other, known as electromagnetic induction (EMI) sensing, transmits an electromagnetic field that can lead to the detection of both ferrous and non-ferrous metals. In this EMI frequency regime, displacement currents $\partial\overline{D}/\partial t$ are negligible relative to conduction current. The primary magnetic field penetrates inside the object to some degree and induces eddy currents within it. In return the induced currents produce secondary or scattered field outside that are measured by a receiver. Since these sensors can sense UXOs, they can detect everything else metallic in close proximity. Therefore, current discrimination techniques have great difficulties in distinguishing UXO from non-UXO metallic debris, found at most UXO sites. The high costs of excavating all geophysical anomalies are well known and are one of the greatest impediments to efficient clean-up of UXO contaminated lands at DoD and DoE sites. Innovative discrimination and classification techniques that can reliably distinguish between hazardous UXO and non-hazardous metallic items are required.

In order for these EMI metal detectors to penetrate the ground they must employ very low electromagnetic frequencies, ranging from tens of Hz to around one hundred kHz. As a consequence, it is not possible to image subsurface objects clearly due to the long wavelengths in the magnetoquasistatic regime. Instead, one must analyze recorded responses in search of some kind of telltale content or signature. This limitation is magnified by the low spatial diversity of the data: Many measurements involve only one component of the secondary field at each one of a limited set of points, and usually at only one instrument altitude. The forward models used for data analysis must be complete enough to provide rea-

sonable estimates of the location and orientation of a target and at the same time a reliable characterization of its properties. It is also desirable that they be fast enough to produce results in something approaching real time.

Discrimination of unexploded ordnance (UXO) is achieved by employing forward models to extracting physics-based electromagnetic parameters from geophysical data acquired over subsurface anomalies and using these parameters as inputs to either human experts or statistical classification methods which determine the likelihood that the target is, or is not, a UXO. In past years, various simple parametric modeling methods have been developed and applied to UXO discrimination problems using monostatic electromagnetic induction (EMI) data. Studies show that there is a need for high-quality vector data and rigorous forward modeling approaches to achieve a high probability of UXO discrimination. In addition to advances in hardware, models that can make use of the amount of high quality data produced by advanced EMI instruments are also needed. Current models include the dipole model [2] and more rigorous models such as the Joint Diagonalization (JD) method [3], Orthonormalized Volume Magnetic Source Method (ONVMS and see Sec. 4.6) [4–6], NSMC [7–15], and analytical models [16–22]. Results from an analysis of initial lab data using the standard dipole model are given in Sec. 5.2 while results of models being applied to APG data are given in Sec. 5.4.

Multi-axis sensors have achieved excellent discrimination performance at recent ESTCP demonstration sites such as Camps Beale and Butner [28, 29] when compared to older single axis sensors such as the Geonics EM63. At many DoD sites, however, terrain and/or vegetation prohibit the use of cart mounted EMI sensors such as the MetalMapper [30] and TEMTADS [31]. More portable instruments have recently been deployed such as the MPV2 [1], and the "Mini"-TEMTADS (MR-201165 [32]). However, these sensors also have drawbacks which need to be addressed in order to achieve a single system that is both portable and advanced enough to allow one instrument to survey, detect, and discriminate, even in difficult cases to avoid later reinterrogation or needless excavation.

The detection and discrimination of UXO depend on both realistic and rigorous modeling and high-quality, diverse data. Recently, several new electromagnetic induction (EMI) sensors have been developed including TEMTADS (MR-0601, MR-1315), MetalMapper (MR-0603), BUD (MR-0437), Geometrics integrated magnetometers (MR-1512), and our MPV (MR-1443 continued in MR-201005) and GEM-3$\mathscr{D}^+$(MR-1537 [33]). These sensors represent the state of the art in

the electromagnetic induction sensing. However, there is still significant room for improvement. For example, most of the recent sensors are cart based systems meant for rapid surveying of sites with benign terrain. As a result, the geometry of the sensor is fixed, which limits data diversity by limiting the collection of data at only fixed location(s) above a target. Inversion modeling is then based on a few data points and a limited look at each anomaly. If additional data points (i.e. different transmitter locations) are used in modeling an anomaly, geolocationing between data points becomes critical but is limited in accuracy by the geolocationing system itself and cart motion. In addition, if there are multiple targets (counting clutter) in the field of view of the sensor, the limited data collected at one location may not be sufficient to resolve multiple targets. Moreover, these carted sensors cannot be deployed at treed sites or sites with challenging terrain (see e.g. Fig. 3.1).

Figure 3.1: Examples of challenging terrain for which Pedemis could be deployed.

Recent man-portable sensors include the MPV [1, 34], GEM-3$\mathscr{D}^+$and the "mini-TEMTADS". The MPV shows promise with its five vector receivers, large sensor

head, excellent SNR, and good depth of detection. With it we have been able to show excellent discrimination results at the Camp Beale ESTCP demonstration site. Even with these encouraging results, the MPV has shown some weaknesses in the areas of positioning, data acquisition modes, and physical design. The beacon positioning system conceived in ESTCP MR-0738 and implemented in the new MPV2 is simpler to operate and works in treed and challenging sites. However, this positioning system adds to the overall complexity of the instrument, adds time to data acquisition procedures, and currently at best provides only 1 cm RMS positioning error. For high fidelity modeling and operational issues, a more accurate and less complicated positioning scheme is desired. Here we make the distinction between positioning, or knowing the position of the Rx coils locally relative to the Tx coil, and geolocationing, or knowing where the sensor is globally (using using e.g. GPS or RF).

All of the above mentioned sensors are monostatic or multistatic with the transmitter coil(s) either collocated with or physically attached to the receiver coils. While there are some advantages to this arrangement (not the least of which is ease of design), data from monostatic sensors are more difficult to model for some algorithms (e.g. upward continuation techniques from MR1590). The user is also typically forced into choosing either a carted sensor and its ability to stop and acquire a few high SNR data points, or a handheld sensor and its forte of acquiring copious data as it is dynamically moved about. A sensor which combines both operational modes would be a significant improvement over these existing sensors. In addition, in multi-static deployment of this proposed sensor, because the Rx coils are movable with respect to the Tx coils, various operational modes which reduce noise and increase data quality are possible (see Sec. 5.2). Our Rx coil array also has the ability to acquire spatial tensor gradients of the magnetic field which help in finding the location of dipolar sources [35, 36] (see Sec. 5.2).

The new Pedemis sensor [37, 38] (see Fig. 4.10 and Sec. 4.1 and Sec. 4.2) has been designed to be a flexible yet user friendly EMI instrument that can survey, detect and classify targets in a one pass solution. It accomplishes this by having several deployment modes (made possible by its decoupled geometry) as well as real time feedback during anomaly interrogation. Pedemis does not suffer from utilizing a complex, external, corded positioning system, but instead an integral positioning system. It is not held by the operator during data collection, and the control electronics are much lighter and consume less power than other portable EMI instruments. As well, Pedemis is carried, not wheeled thus giving it more de-

ployment options in challenging and/or vegetated sites. It has many more Tx/Rx combinations for greater data diversity, and a flexible user interface which provides real-time feedback to the user.

4 Materials and Methods

The initial phases of this project consisted of designing the sensor itself to achieve the objectives stated above in Sec. 2. The design of the sensor is detailed in Sec. 4.1 while the completed instrument is detailed in Sec. 4.2. As part of the design, we incorporated an integrated positioning system into Pedemis which relies only on the primary field of the sensor and no external hardware. We developed a general but slower method of finding the position of the Rx array (see Sec. 4.3). We also developed a faster but currently less general method for positioning the Rx array based on the mutual inductance of the Tx and Rx coils (see Sec. 4.3.b). The background subtraction used for Pedemis must be more general that for fixed geometry instruments, and the methods we considered are discussed in Sec. 4.4. The operation protocols and deployment options which enable Pedemis to be broadly applicable to a wide range of UXO remediation scenarios are explained in Sec. 4.5.

4.1 Pedemis Design

Pedemis is a flexible platform with two separate components: a square transmitting array consisting of nine coplanar 40cm TEMTADS size Tx coils [31], and a detachable 3×3 planar array of vector receivers (each receiver a reproduction of the MPV2 receivers [1]). The receivers can either be placed to collect static data or moved around above or near the transmitting coils to obtain dynamic data (see Fig. 4.10). Both of these components can be affixed to a cart for larger scale detection surveys. Pedemis is usually carried by two people in a stretcher-type arrangement for cued interrogation even in rugged and/or challenging terrain.

The Pedemis hardware can be considered in three major parts:

1. Tx array
2. Rx array
3. Controlling electronics

The following sections will describe the design considerations of each of these three aspects of the instrument. As we designed Pedemis, we kept in mind the following design objectives:

1. maintain physical decoupling of Tx and Rx arrays (see Sec. 4.1.a and Sec. 4.1.b)
2. high SNR data

3. the target should be illuminated from multiple look angles (see Sec. 4.1.a)
4. Tx weight plus Rx weight remain under 45 pounds (see below)
5. 2 minute or less primary data collection sequence (excludes a follow up interrogation for suspected deep targets, see Sec. 4.5)
6. controlling electronics be lighter weight than previous instruments (see Sec. 5.1)
7. flexible, simple, and robust user interface (see Sec. 5.1)
8. at most, two people required to operate
9. subcentimeter positioning of the Rx array (see Sec. 4.3)
10. be able to apply our advanced models at both the data acquisition stage and post processing stage

As of January, 2012, the Tx and Rx arrays have been fabricated as shown in Figs. 4.1–4.3. The combined weight of these arrays is about 38 pounds which does not include cabling or gurney poles. The Tx array is 1.2 meters on a side, while the Rx array is 50cm on a side. The overall weight of the controlling electronics (NI cRIO) plus batteries is approximately 20 pounds. The mostly fabricated Pedemis instrument described herein fulfills the above design goals, resulting in an advanced and effective EMI instrument capable of acquiring high quality data from a flexible platform.

4.1.a Pedemis Tx Array

We considered various designs for the Pedemis Tx array. Here is a list of the designs considered:

1. 4 or 9 horizontal coplanar coils
2. 4 vertical side coils or not
3. 1 large encompassing coil or not

Together there were 8 possible base configurations not counting sizing of the coils. Figure 4.4 shows some possibilities we considered during the design phase of Pedemis.

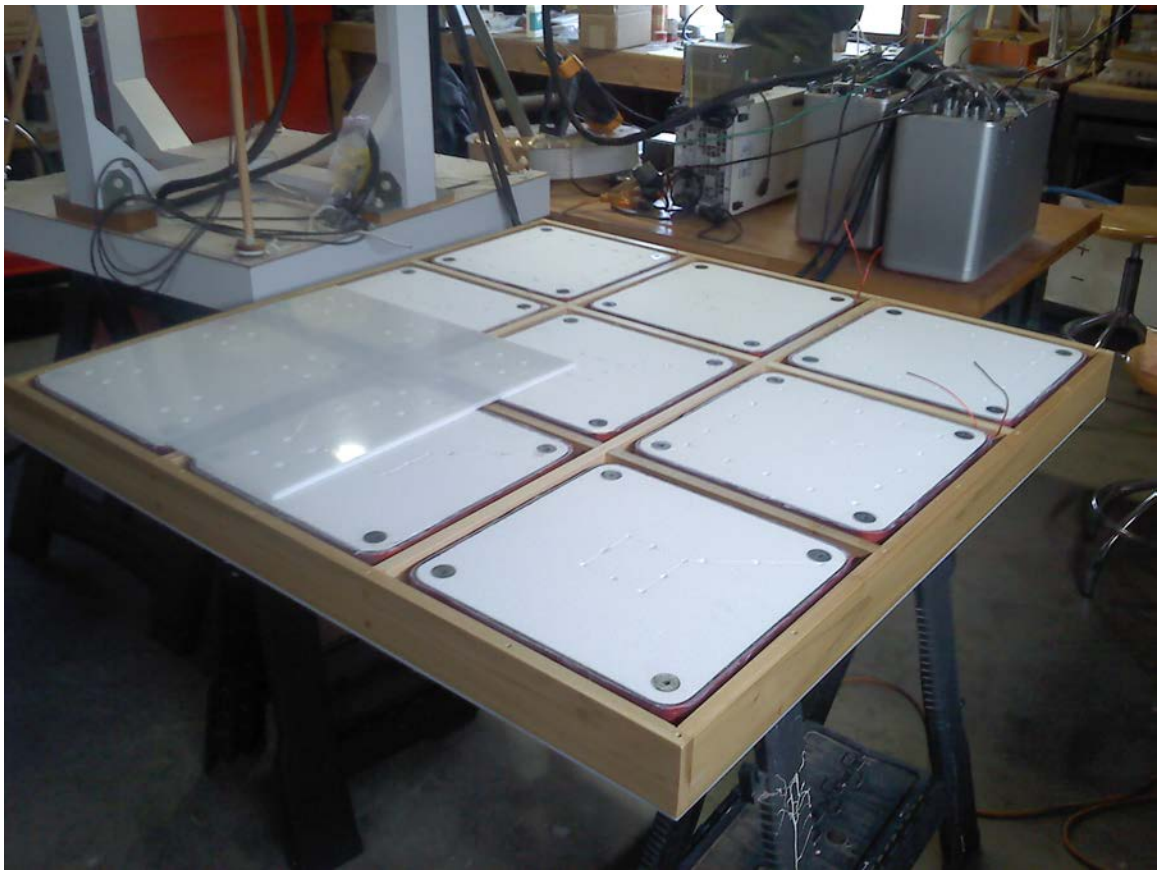

Figure 4.1: Pedemis Tx array. Tx loops are the same size and template as the TEMTADS coils. 35cm loop size with 40cm between centers. See Sec. 4.1.a for more information about the Pedemis transmitter array.

Figure 4.2: Pedemis Rx array on top of the Tx array. Rx receiver coils are the same size and template as the MPV2 coils. Receiver coils have an 8cm loop size with 20cm between centers. See Sec. 4.1.b for more information about the Pedemis receiver array.

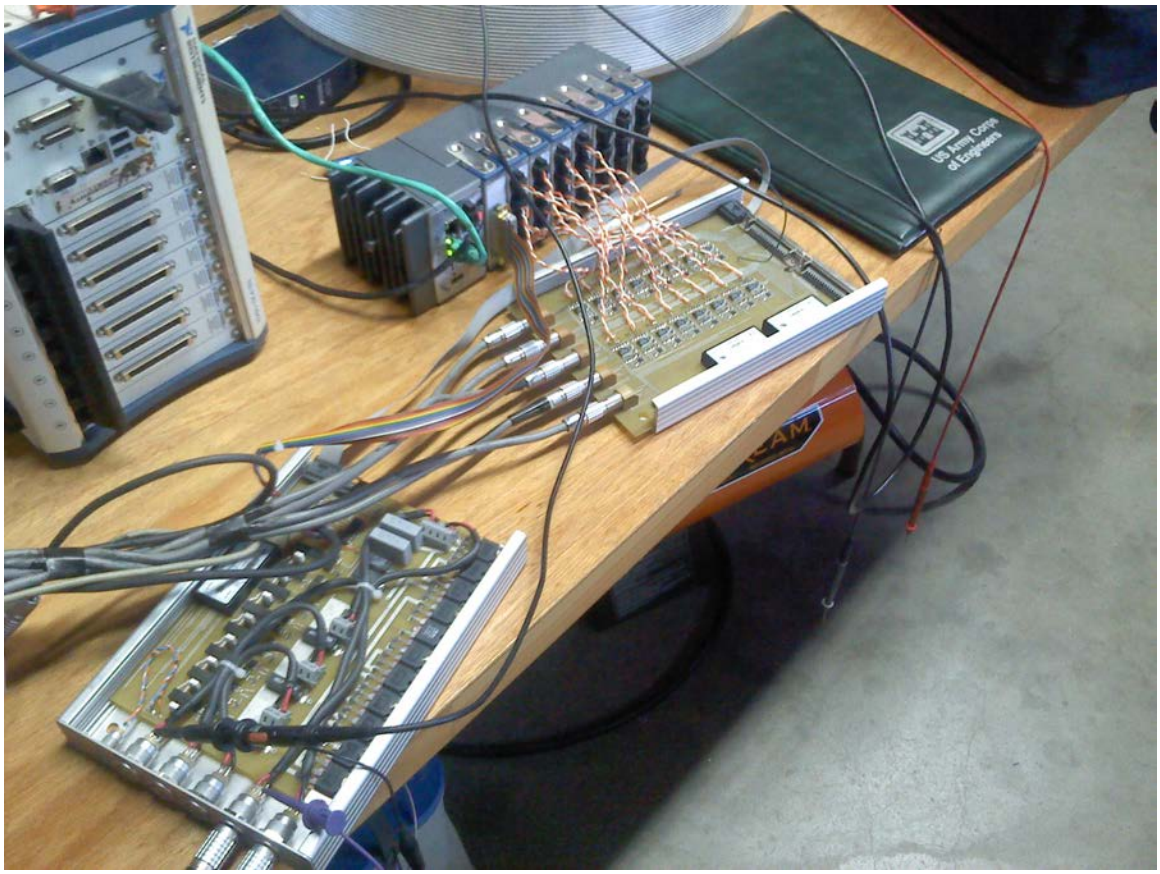

Figure 4.3: Pedemis control electronics. A National Instruments cRIO system with DAQ modules and a digital IO module control Pedemis's transmitters and receivers. See Sec. 4.1.c for more on the electronic control system of Pedemis. The cRIO is programmed in LabVIEW (see Sec. 5.1 for more on Pedemis control software). Also shown are the old transmitter control board (lower left) and the old filter board (in front of cRIO).

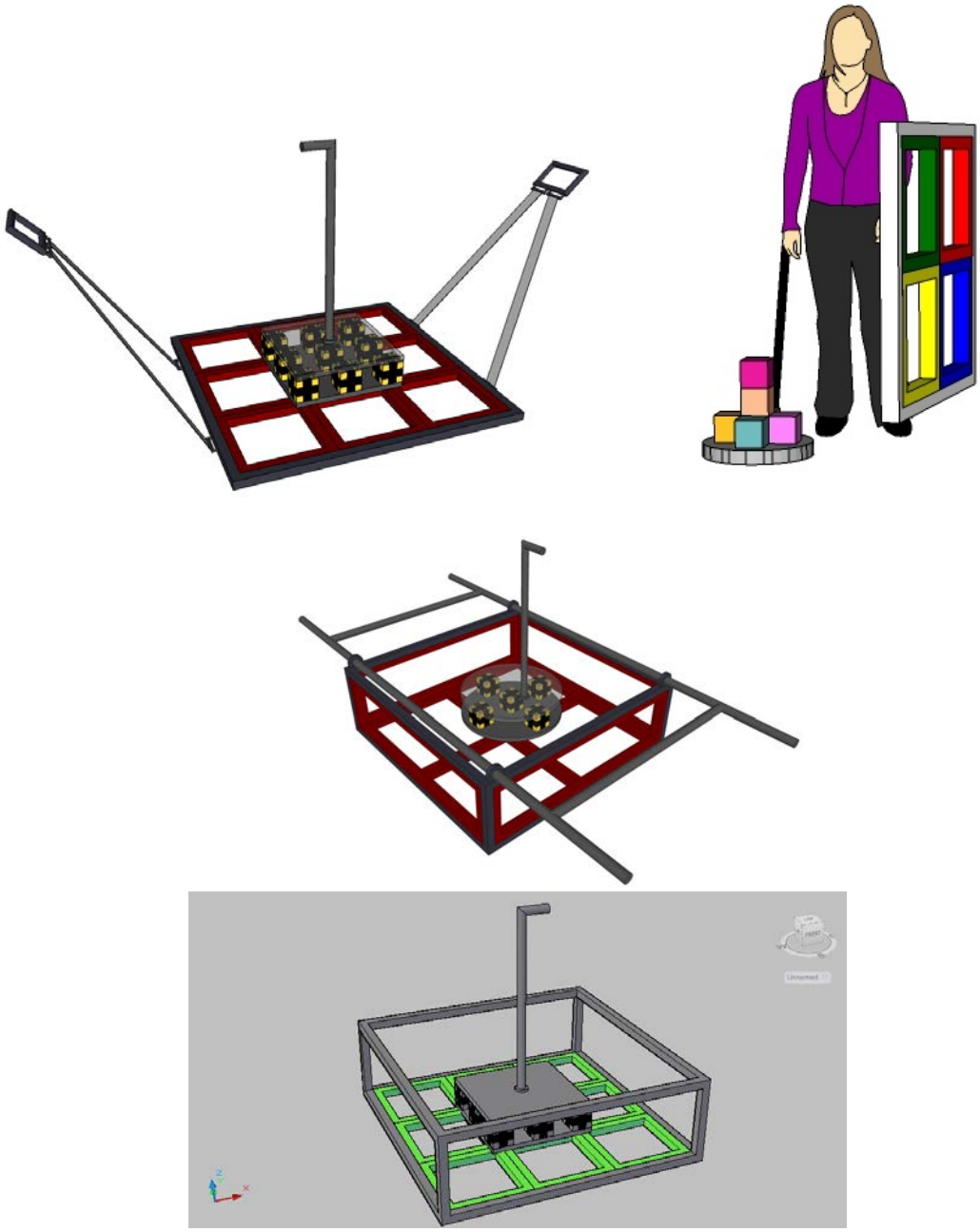

Figure 4.4: Possible designs of Tx and Rx arrays considered during the design phase of Pedemis before arriving at the design in Fig. 2.1.

We simulated various designs for the Pedemis transmitters to help us decide which Tx configuration would best achieve the design goals in Sec. 4.1. Figures 4.5–4.7 present the results of three simulations illustrating the trade offs associated with different numbers of coils with different sizes in different configurations. All three figures show the inverted total ONVMS (see Sec. 4.6) from a 60mm mortar at 40cm depth to center simulated with the MAS (method of auxiliary sources) algorithm. The straight line shows the result without noise added to the secondary field, while the line with circles shows the inverted result with some noise added to the synthetic data.

Figure 4.5 shows that for a 2x2 Tx array, while the algorithm was able to invert for the T-ONVMS, the results degraded quickly for the amount of noise added with the result that the T-ONVMS with noise is significantly different than the T-ONVMS without noise even at early time where the secondary field is the strongest. This is due to the target being illuminated by only 4 look angles with this 4 Tx configuration. The amount of information at the receivers about the target is less than with a configuration that has more transmitters. For anomalies with multiple targets present, fewer transmitters also results in a lessened capability to discriminate between the various targets due to a lack of information.

On the other hand, as can be seen in Fig. 4.6, when there are more Tx with some Tx in a vertical orientation, the inverted T-ONVMS for noisy synthetic data follows the noise free T-ONVMS to a much later time due to the many more look angles and increased information in the data. The four added vertical coils do help some in interrogating the anomaly, but also unfortunately add considerable weight to the assembly via their metal weight and necessary supporting structure.

In between these two extremes is the 3x3 array with results shown in Fig. 4.7. This configuration results in only minimally worse T-ONVMS for the noisy case than the case with the four vertical coils. The takeaway here is that while the four vertical coils can add information for the inversion algorithms, the added information is not significant, but the increase from a 2x2 to a 3x3 Tx array does add resolution and data diversity to the secondary field recorded by the receivers.

Given these considerations and the practical constraints imposed by Tx circuitry, weight, and complexity, we decided on a 3x3 Tx array with 35cm transmitters (same Tx design as TEMTADS) spaced 5 cm apart resulting in an overall Tx assembly of 1.2m on a side weighing about 35 pounds. This compromise yields high quality data with several looks at the anomaly sufficient to distinguish multiple targets in highly cluttered environments.

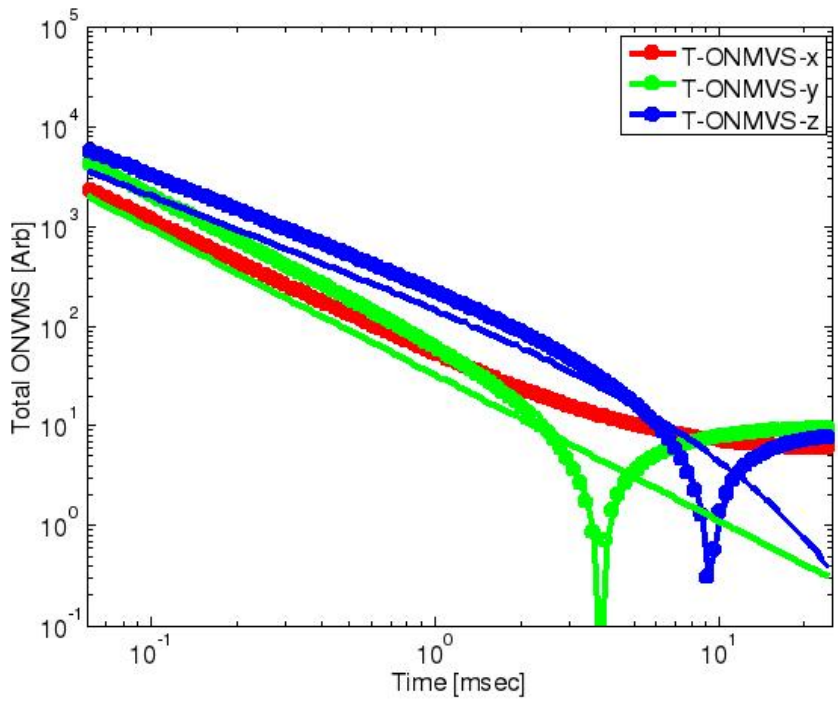

Figure 4.5: Simulated 2x2 Tx array results. Tx loop size was 45cm on a side. The lines without circles show the result without noise added, while the lines with circles shows the inverted result with some noise added to the synthetic data.

4.1.b Pedemis Rx Array

From a data analysis standpoint, more data from more receivers in an EMI system will lead to a more robust result. However, given practical considerations of size, weight, and cabling, only a finite number of receivers can be implemented. Experience with the MPV and MPV2 [1, 34] made it clear that vector receiver cubes which measure all three components on the secondary magnetic field from the target produced superior data than single axis receivers. As a result, one early decision was to use these 8cm receiver cubes in Pedemis (see Fig. 4.8). These cubes are made from 8cm balsa wood blanks routed to accept small diameter copper wire especially wound to produce the same receiver moment in all three dimensions. For more information on the design of these Rx cubes, see the MPV-II documentation.

The question of how many Rx cubes to implement on Pedemis involves many considerations including weight, complexity, number of DAQ modules in the NI cRIO, cabling issues, protocol (see Sec. 4.5), operator fatigue, etc. Each receiver

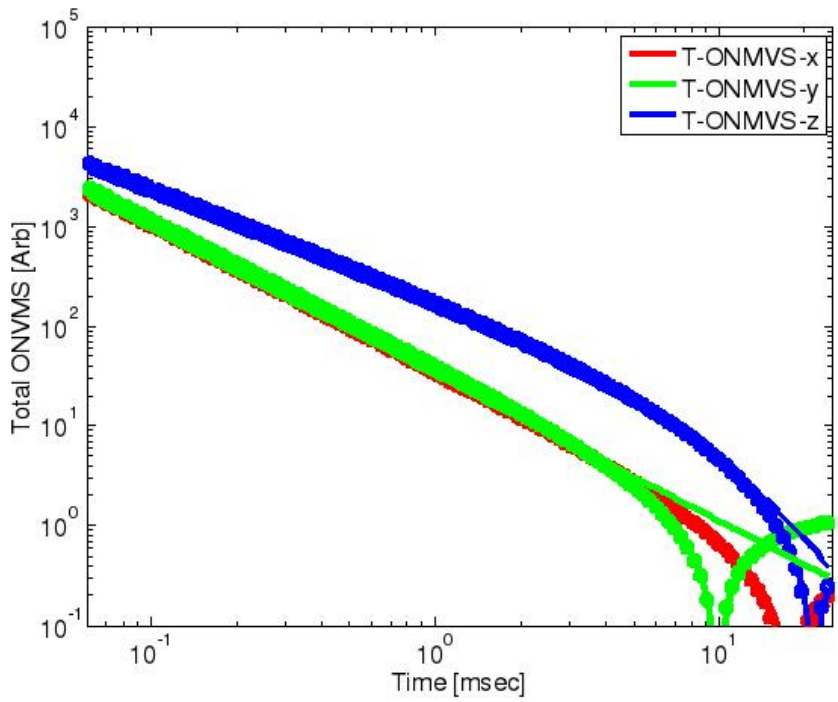

Figure 4.6: Simulated 3x3 + 4vertical Tx array results. Horizontal Tx loop size was 30cm on a side. Vertical Tx loop size was 30cm tall 90cm long. The lines without circles show the result without noise added, while the lines with circles shows the inverted result with some noise added to the synthetic data.

cube requires an additional preamplifier board near the cube itself to minimize stray EM noise from the surroundings. Additionally, 9 separate wires and 3 DAQ channels are required to accommodate each cube. Originally, we considered a 6x6 stationary Rx array for Pedemis, but abandoned that due to practical considerations. Perhaps if a multiplexed Rx array were to be designed, then this number of Rx channels ($3 \times 36 = 108$) could be accommodated. Aside from these practical matters, we wanted the Rx array to be physically decoupled from the Tx array, so this fixed design was not implemented.

The 6x6 array of 20cm spaced secondary field samples was still desirable, however, so a compromise 3x3 array moved into the 4 corners on top of the Pedemis Tx array was suggested. The 20cm sampling size in our analysis is sufficient to discriminate between objects in close proximity without being redundant for most anomalies seen to date. Though the 3x3 array would require moving the Rx array 4 times for the most detailed data shot, the advantages of dense, high quality data while preserving a manageable cabling and DAQ module load outweighed

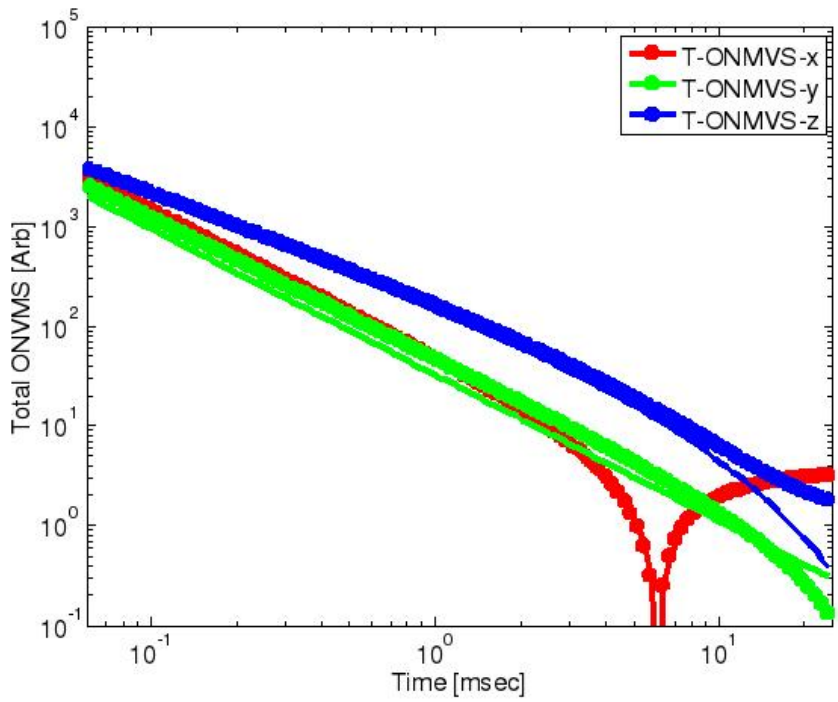

Figure 4.7: Simulated 3x3 Tx array results. Tx loop size was 30cm on a side. The lines without circles show the result without noise added, while the lines with circles shows the inverted result with some noise added to the synthetic data.

the increase in complexity of the data acquisition protocol. This compromise also conveniently allowed the Rx array to be decoupled from the Tx array while keeping the weight to about 10 pounds. See Sec. 4.5 for more information on Pedemis deployment protocols. The position of the Rx array is calculated via measurements of the primary field during the "on" time of the Pedemis transmitters. For more on this positioning method, see Sec. 4.3.

4.1.c Pedemis Control Electronics

Pedemis uses the NI cRIO for controlling the Tx and Rx arrays and associated circuitry. This represents a step forward from prior portable EMI systems like the MPV-II in terms of weight, power usage, and decreased complexity. The weight of the cRIO chassis and modules is around 8 pounds compared to over 20 for the full PXI chassis and related electronics. Instead of 3 lithium ion batteries and 3 hour swap intervals, we expect to use only 2 of these batteries with a 5-6 hour swap interval. Also, the cRIO chassis, with its integrated modules, is simpler and more robust than the prior full PXI chassis, but the cRIO is still a fully functioning

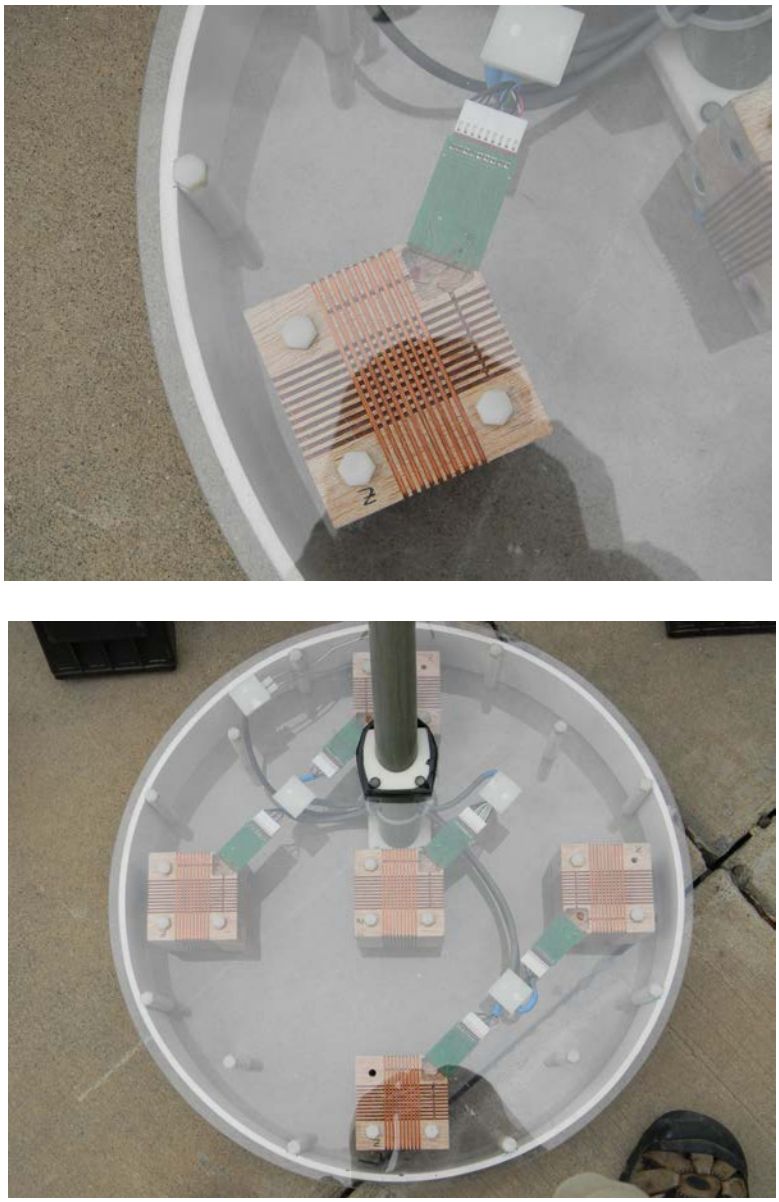

Figure 4.8: Receiver cubes from the MPV-II instrument also used in the new Pedemis. Cubes are made from 8cm balsa wood blanks routed to accept small diameter copper wire.

field ready computing platform. There are 4 main components to the cRIO control system shown in Fig. 4.9 and Fig. 4.3:

1. CRIO-9022, Real-Time PowerPC Embedded Controller for CompactRIO, 533 MHz, 2 GB storage, 256 MB DRAM
2. cRIO-9116, 8-slot Virtex-5 LX 85 Reconfigurable Chassis for CompactRIO
3. NI 9222, 4-Ch, 10 V, 16-Bit, 500 kS/s, Simultaneous AI C Series Module for

CompactDAQ and CompactRIO (Pedemis needs 7 of these: 27 Rx channels and 1 Tx current channel)

4. NI 9401 8-Channel, 100 ns, TTL Digital Input/Output Module

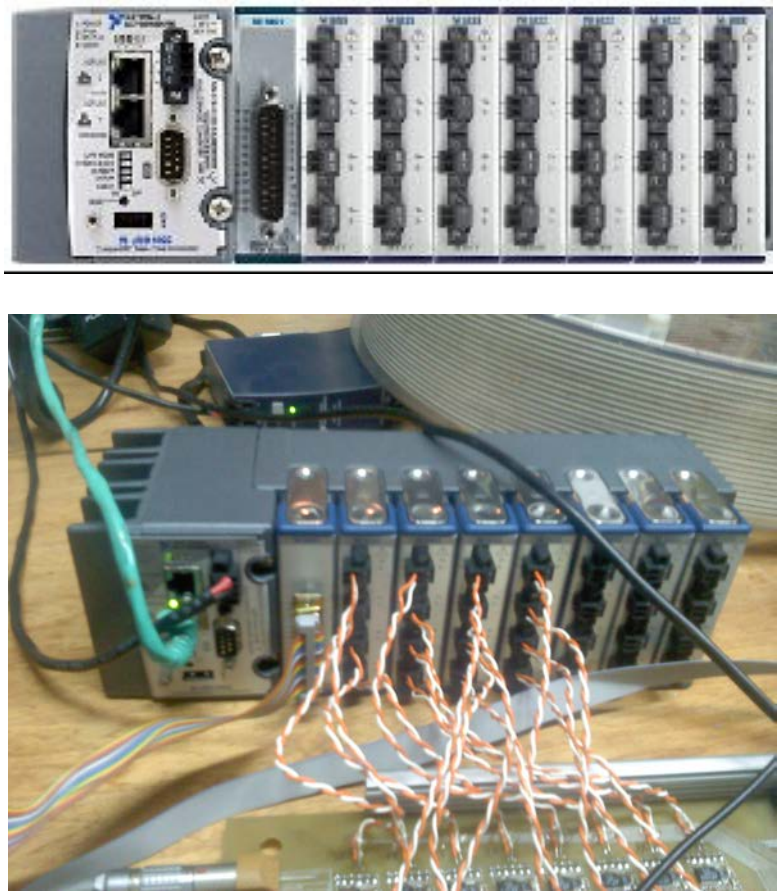

Figure 4.9: Pedemis control electronics. Upper figure is as designed at NI.com. Lower figure is as configured for the initial data reported in Sec. 5.2. The NI-9401 is in the leftmost slot while the 7 NI-9222's are in the remaining 7 slots of the 8 slot chassis.

The only current disadvantage to using the NI-cRIO platform is that G&G's EM3D control software written in Visual Basic and C# would not run on the cRIO, thus necessitating programming Pedemis control software in LabVIEW from scratch. We have made progress in programming this software, and this is discussed in more detail in Sec. 5.1.

4.2 Completed Pedemis Instrument

A photograph of the completed Pedemis sensor is shown in Fig. 4.10(a) showing the independent transmitter (Tx) and receiver (Rx) arrays. The coplanar 3×3

array of square coil transmitters is visible through the plastic cover, producing a total sensor size of about 121.5 cm $\times$ 121.5 cm. The square Rx array, with a side of about 56 cm, is shown in the top-left position with a vertical non-metallic handle meant to facilitate maneuverability. The sensor is here shown in a laboratory setting, mounted on sawhorses with a UXO underneath. In the field, poles are attached to the the front and back carrying straps for carrying by two operators during dynamic data collection as shown in Fig. 4.10(b). For static data collection Pedemis is laid on the ground and not carried (see Fig. 4.10(c)). The Tx and Rx arrays are schematically represented in Fig. 4.11, with the receivers also arranged in a 3×3 configuration with 20 cm center-to-center spacing. Each receiver is a triaxial receiver similar to those on the MPV2 [1]. The default dataset is therefore composed of 9 transmitters $\times$ 9 receivers $\times$ 3 components, or 243 time signatures recording the secondary magnetic field between 100 μs and 25 ms.

Pedemis uses the National Instrument cDAQ and a small mini-pc for controlling the Tx and Rx arrays and associated circuitry. This represents a step forward from prior portable EMI systems like the MPV-II in terms of weight, power usage, and decreased complexity. The weight of the cDAQ chassis and modules is around 8 pounds compared to over 20 pounds for the full PXI chassis and related electronics. Instead of 3 lithium ion batteries and 3 hour swap intervals, we use only 2 of these batteries with a 5-6 hour swap interval. Also, the cDAQ chassis, with its integrated modules, is simpler and more robust than the prior full PXI chassis. The combined weight of the transmitter and receiver arrays is about 38 pounds (not including cabling or gurney poles) whereas the overall weight of the controlling electronics plus batteries is approximately 20 pounds.

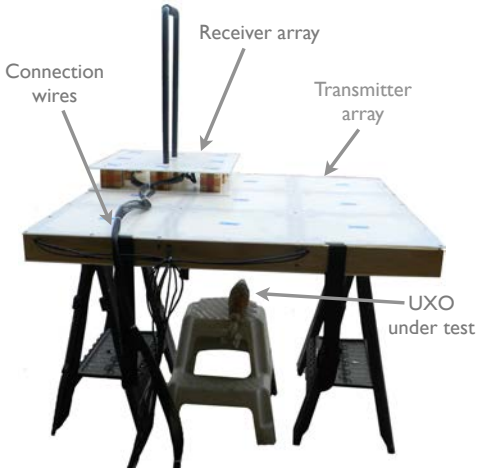

(a) Photograph of the sensor and a UXO under test in a laboratory setting.

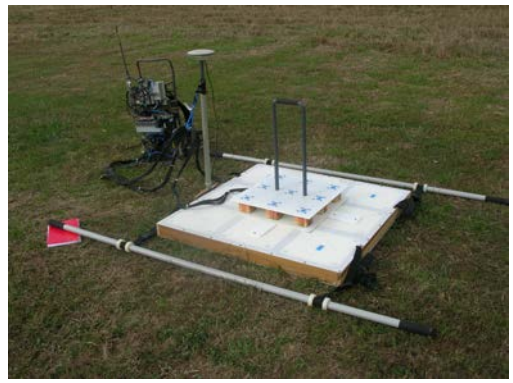

(b) Sensor in operation at APG on the ground for cued interrogation.

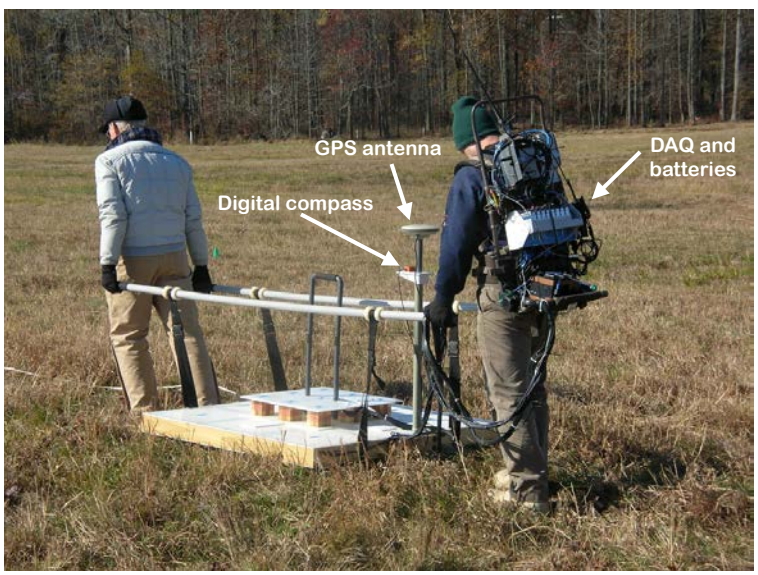

(c) Sensor in operation at APG carried by two operators in the open field.

Figure 4.10: The Pedemis sensor in both laboratory and field settings. Total weight of the Tx and Rx arrays is 38 pounds, while the total weight for the backpack is 20 pounds.

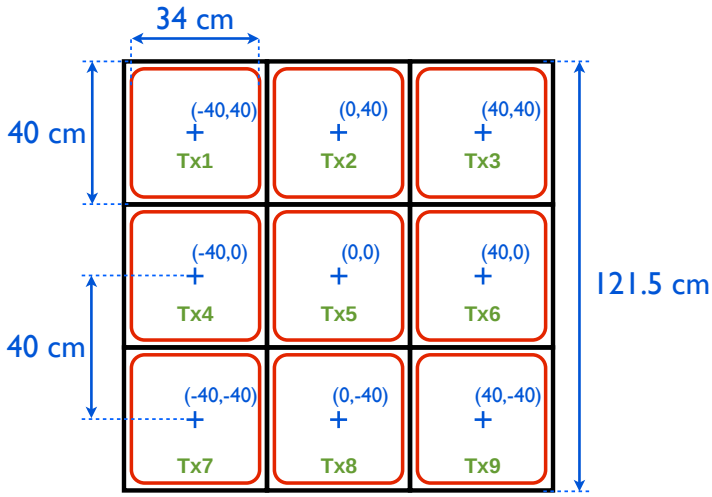

(a) Transmitter array.

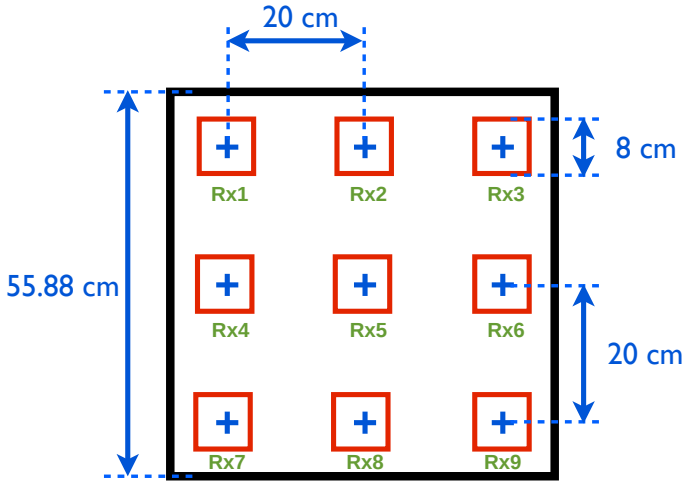

(b) Receiver array.

Figure 4.11: Schematic representation of the Pedemis sensor.

4.3 Pedemis Rx Positioning

We have developed two approaches to calculate the position of the Rx array with respect to the Tx array. The first approach involves a brute force technique of minimizing the error function between the received primary field at the receivers and a dipole source. This method is described below in Sec. 4.3.a.

The second method is faster but more restrictive in that it presently only works for cases in which the Rx coils are parallel or perpendicular to the Tx coils, i.e. no angular mismatch can occur. This method is fast, and we believe could be extended to accommodate arbitrary Euler angles between the Tx and Rx coil planes. This method is described in Sec. 4.3.b.

4.3.a General Rx Array Positioning

The Rx array on Pedemis is not held in a fixed geometry relative to the Tx array except as noted in Sec. 4.5 for cued interrogation mode #1 (CIM1). As a result, the position of the Rx array must be retrieved in order for data shots taken at different Rx array positions to be be meaningful. This position of the Rx array is found on Pedemis by a beacon positioning approach, an approach first conceived in our MR-1537 GEM-3$\mathscr{D}^+$project and continued in MR-1443 MPV and MR-201005 MPV2.

The beacon positioning concept relies on the capability of the receivers to measure the strength of the primary field when each transmitter is being energized. After these data from the "on" time of the transmitter are recorded, the receivers then collect EMI data from the "off" time of the transmitters. Given these "on" time data, the geometry of the transmitters, and a record of the current in the energized transmitter, it is possible to calculate where the Rx array is in 3D space to under 1cm accuracy when the Rx array is within 2 meters of the Tx array.

We modeled the Pedemis beacon positioning system in order to predict how accurate we could expect the calculated position to be. Figure 4.12 shows an example of the Rx array above a model of the Tx array with the closest receiver at least 10cm away from the Tx coils. Using our simulation as a sanity check, if we use all four expected Rx array locations (as in cued interrogation mode #2 (CIM2), see Sec. 4.5), there is essentially only numerical error on the order of machine precision for the inverted position of the Rx array (see Fig. 4.13).

After these types of sanity checks, we also wanted to make sure targets under the Tx array would not distort the primary field sufficiently to degrade the "on"

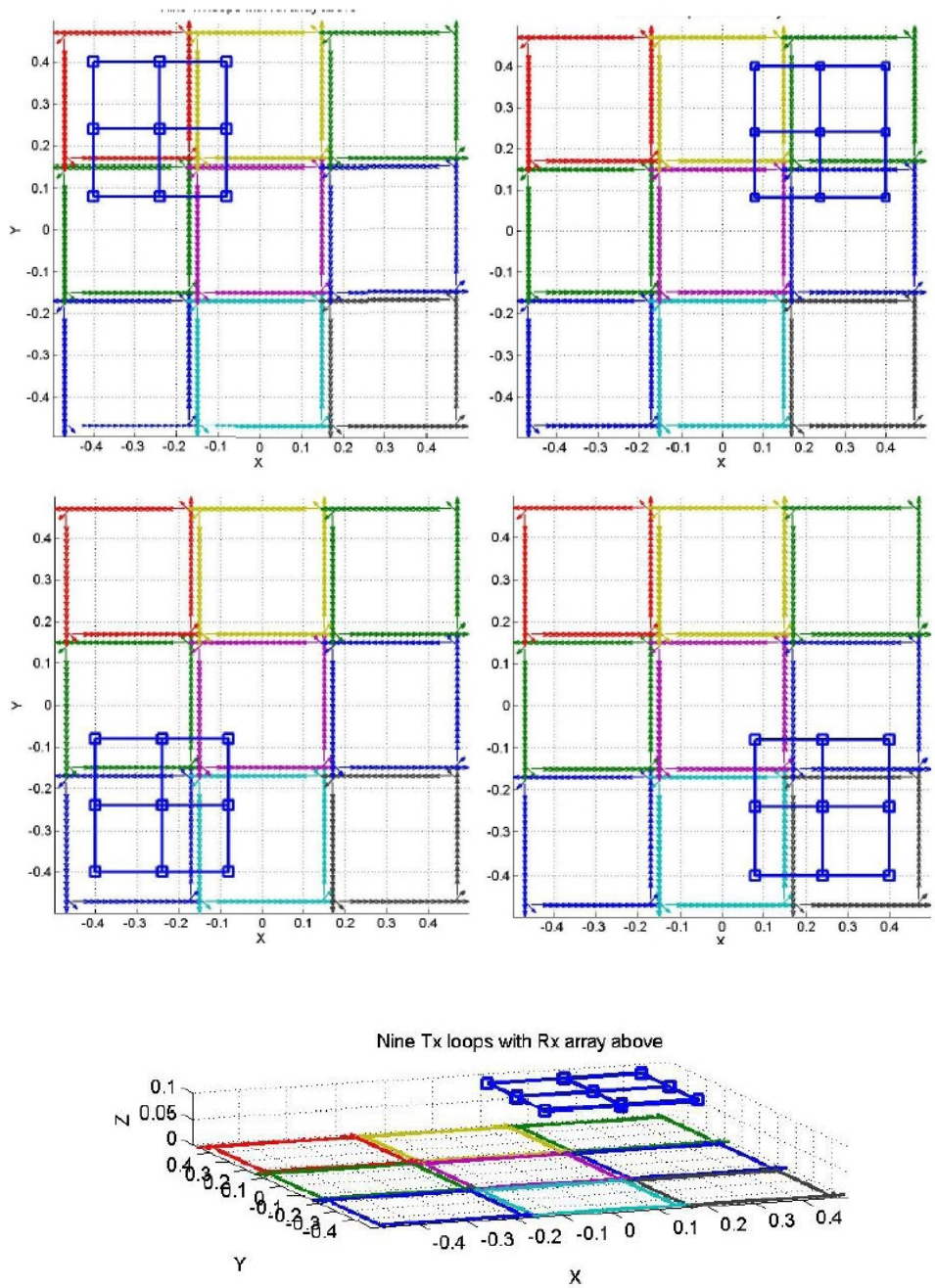

Figure 4.12: Pedemis beacon example with Rx array above the Tx array.

time measurements and produce a false position. To this end, we added a simulated 10cm sphere only 10cm below the center of the Tx array to see what effect it would have on the primary field and thereby the inverted Rx array position. Figure 4.14 shows the log10 positional error in the inverted Rx array location when the Rx array is 10cm above the Tx array and the sphere is present. Even though the

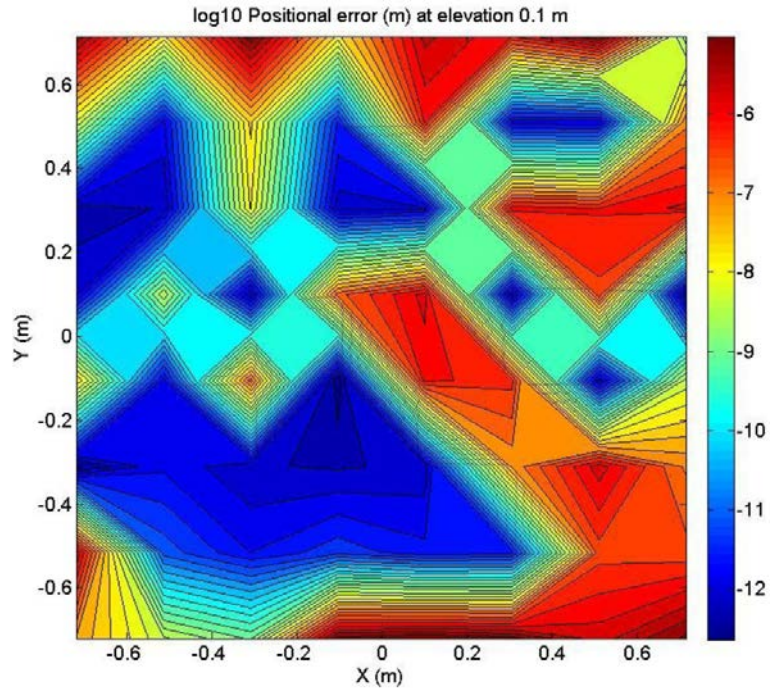

Figure 4.13: Pedemis beacon example error. For this synthetic case, the error is essentially only numerical error on the order of machine precision for the inverted position of the Rx array.

presence of the sphere caused up to 1.5% perturbation of the primary field for some Tx/Rx combinations, the overall position of the Rx array was accurate to within less than 1mm.

We applied the algorithms developed during the simulation phase to the initial data collected in November 2011 in Grand Junction, CO (see Sec. 5.2). For the data shot #3 in Sec. 5.2, the MPV2 sensor head was left in one location (at the bottom right corner of the Tx array) while all nine transmitters fired in turn (see Fig. 5.3). For this case, with the Rx array directly over the (undamped) transmitters, the error in the inverted Rx array position was 2-3mm, which is on the order of our physical measurement expected error.

Our final test corresponding to data shot #4 in Sec. 5.2 tested whether the position of the Rx array could be inverted for even when the Rx array was positioned outside the Tx array (see Fig. 4.15). Figure 4.16 shows the inverted position of the Rx array using our algorithms. In this case as well, the inverted position was withing half a centimeter which is within the manual positioning and measurement error.

These results are encouraging in that they suggest that the beacon positioning system and algorithms can invert for the position of the Rx array when the Rx

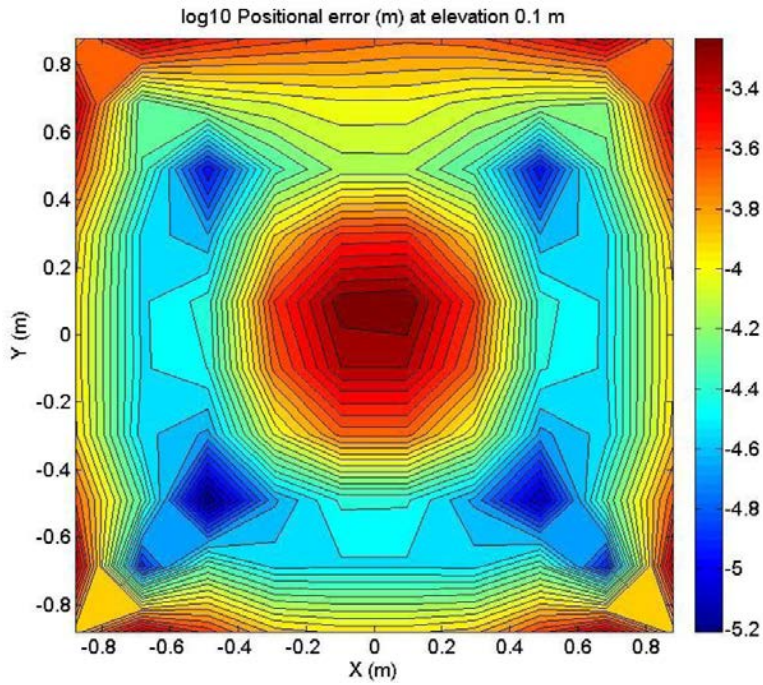

Figure 4.14: Pedemis beacon target induced error from a sphere placed under the Tx array.

array is within a meter of the Tx array. The accuracy appears to be within 1cm and in most cases on the order of a few millimeters.

More details on the exact algorithms developed for Pedemis positioning are found in Sec. 5.4.d and references therein.

4.3.b Positioning Based on Mutual Inductance

The receiver assembly of Pedemis can be fixed to the transmitters or detached from them for enhanced flexibility and convenience. The latter mode requires a positioning system that finds the location of the receivers with respect to the transmitters at any time without hampering portability or requiring communication with outside agents (which may be precluded by field conditions). The current system described above in Sec. 4.3.a examines the primary field during the transmitters' on-time phase and optimizes to find the location at which it is most likely to obtain the combination of measured values. We have also developed an algorithm that computes mutual inductances analytically and exploits their geometric information to predict location. The method does full justice to Faraday's Law from the start and incorporates the fine structure of both transmitters and receivers; it is exact and involves only elementary functions, making it unnecessary to set up and

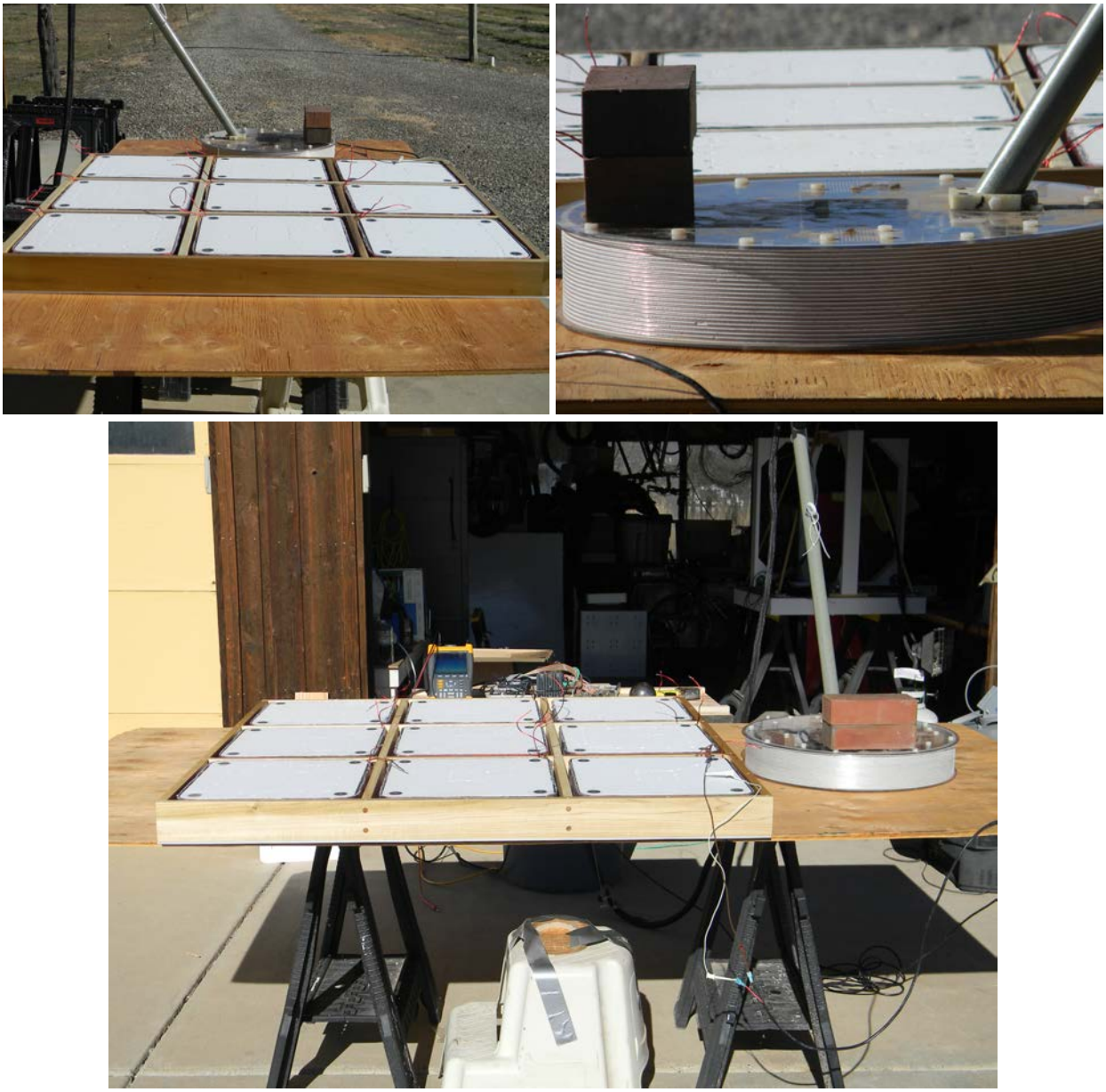

Figure 4.15: Pedemis Beacon Inversion #1 for the case of the MPV2 at the lower right hand corner of the Tx array. No target was present and the inverted position was within 0.5cm of the measured position.

monitor approximations and guaranteeing robustness and stability everywhere; it uses a fraction of the memory and is orders-of-magnitude faster than methods based on numerical quadrature. We have tested the algorithm on Pedemis and have obtained encouraging results which we summarize in this section.

4.3.b.(1) Introduction and Background The main feature of Pedemis is that the receivers can be detached from the transmitters in order to allow flexible data acquisition modes and deployment options. Figure 2.1 shows two possible configurations. To be useful, the system must know the location of the receiver assembly accurately, which information is required at the discrimination stage. Moreover, it would be desirable that the positioning system be as self-contained and portable as possible and perform its duty in close to real time. Previous experience with other sensors [39–42] has shown that it is possible to use the primary field of the sensor for this purpose: during the "on-time" of its duty cycle, the transmitters produce strong fields, and their relative strengths can be fed into an optimization procedure to to find the location at which it is most likely to obtain a given measured combination.

According to Faraday's law [43], the quantity measured by an EMI receiver is the electromotive force given by the negative time derivative of the flux through its area:

$$\mathscr{E} = -\frac{d\Phi}{dt} = -\frac{d}{dt}\int \mathbf{B}\cdot\hat{\mathbf{n}}\,da. \tag{4.3.1}$$

To get reasonable estimates of location it is necessary to characterize the dimensions and geometry of the sensor with as much realism as possible, for several reasons: 1) The transmitters and receivers are very close to each other in most cases, and in the near field the effects of finite size are noticeable. 2) The measured signal depends on the time derivative of the current (see Eq. (4.3.3)); this quantity must be found numerically and its computation amplifies the measurement noise. 3) The currents vary significantly from transmitter to transmitter.

The surface integration in Eq. (4.3.1) can be treated with varying levels of detail. "Volume integration" considers the signal to be the sum of the fluxes through all the turns of the wire; this is the most realistic approximation to Eq. (4.3.1). One can also perform "Area integration," in which the signal is taken to be the flux through just one turn (taken to be the middle coil) multiplied by the number of turns. In each of the preceding cases the integrals are evaluated using Gauss-Legendre quadrature [44]. Finally, in the "Point receiver" limit one can assume the measured signal to be the field at the center of the cube, multiplied by the area of a coil and the number of turns.

As Figures 4.17 and 4.18 show, the differences between the three limits are noticeable in ordinary configurations, and can be quite large. On the other hand, the time that each of these approximations takes to run increases with increasing

realism: the integrals in the figures were computed using a 9×9 Gauss-Legendre grid, and thus the area integration requires almost two orders of magnitude more operations than the point limit; for the volume integration it is necessary to perform the surface integration tenfold. This is independent of the number of turns in the transmitter array; if the transmitter is treated to full accuracy, the number of required operations increases by another factor of 30. To that add the fact that there are 9 transmitters and 9 receivers, and that to find the location of the receiver assembly we have to evaluate this forward model repeatedly as part of an optimization. It is clear that we must take a different approach if we are to obtain the results in real time. The method we have developed is the topic of the following section.

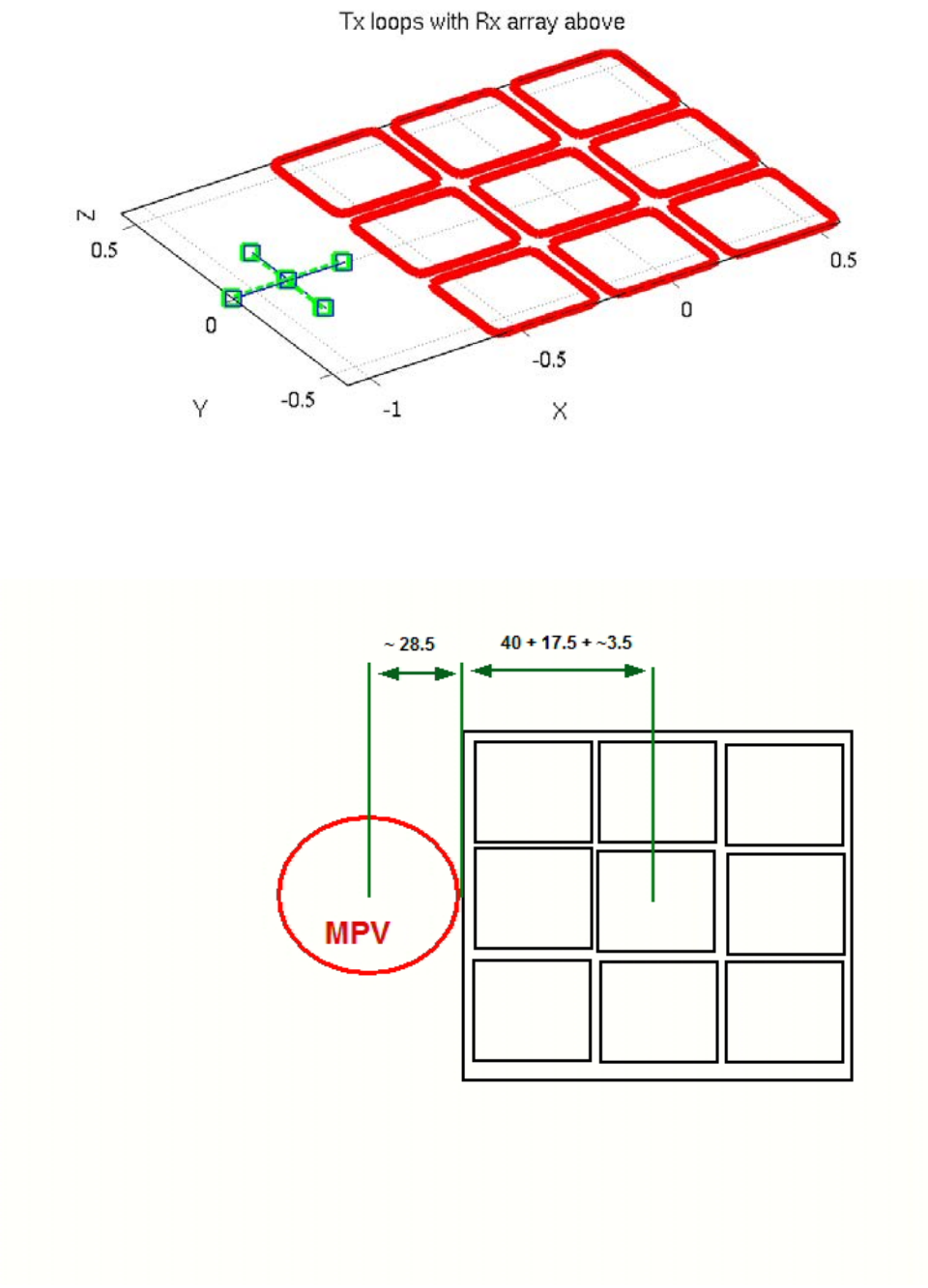

Figure 4.16: Pedemis Beacon Inversion #2 for the case of the MPV2 outside and to the left of the Tx array. No target was present and the inverted position was within 0.5cm of the measured position.

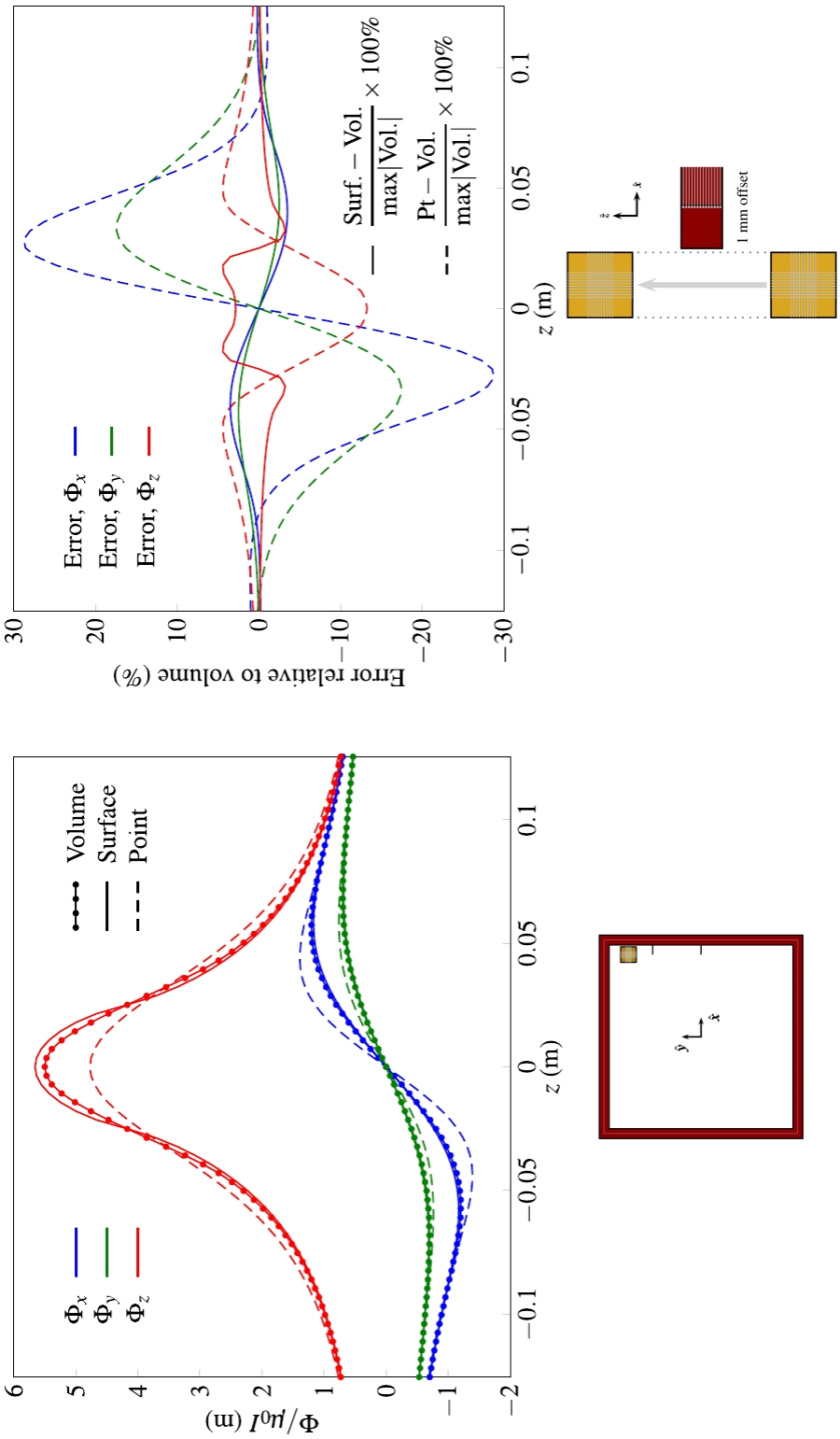

Figure 4.17: The difference between the point, area, and volume approaches to the surface integration in Faraday's law are noticeable. Shown are the measured fluxes in the x-, y-, and z-directions when a Pedemis receiver cube is moved on a vertical trajectory offset 1-mm from one of the transmitters (the actual transmitters are smaller). The area integration is superior to the point limit.

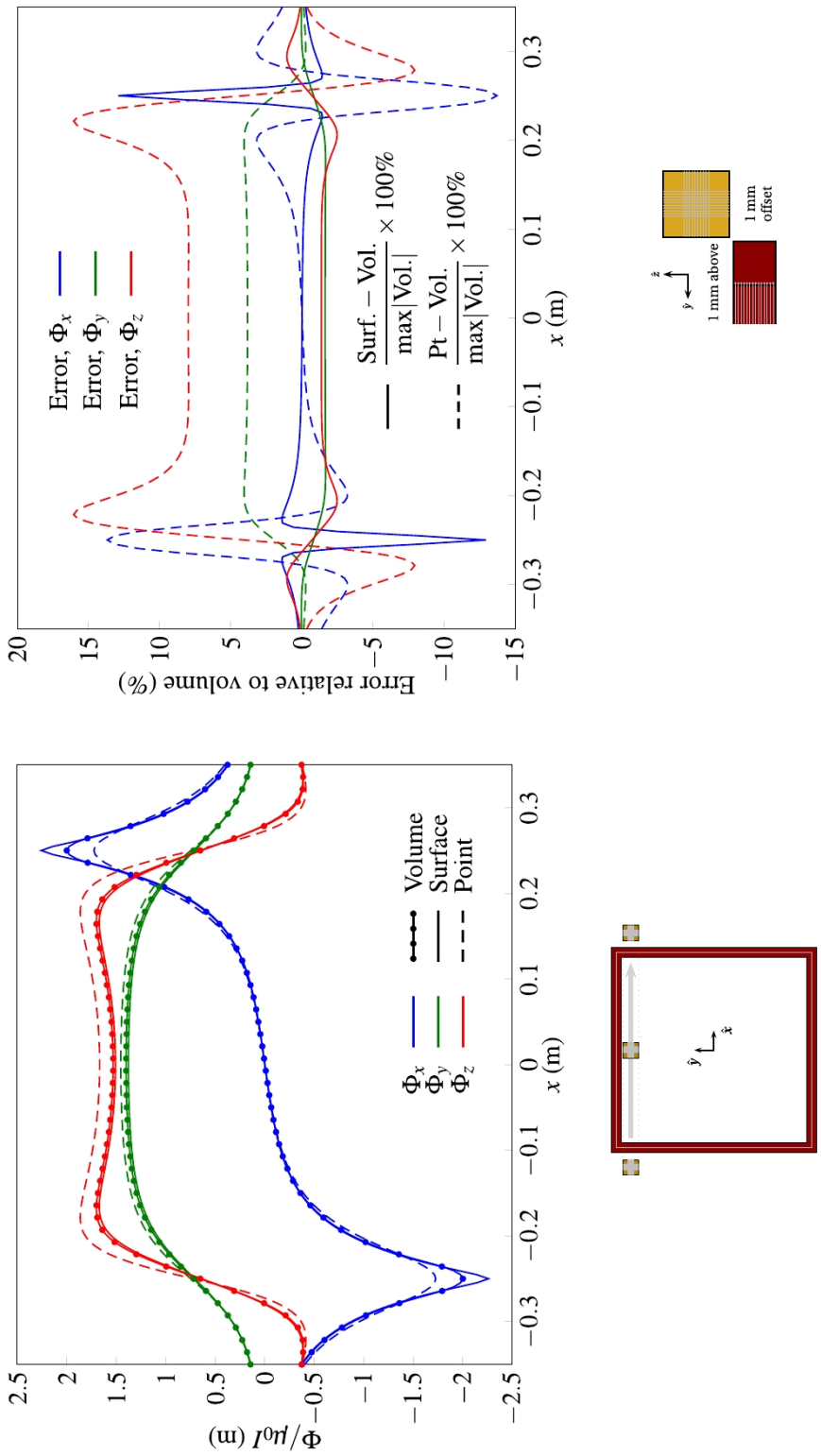

Figure 4.18: Similar to Figure 4.17, but now on a horizontal trajectory just above the transmitter assembly. Right above the transmitter coils the differences are noticeable, even when the area integration is performed. The method of Section 4.3.b.(2) performs the integration implicitly to full accuracy.

4.3.b.(2) Positioning via mutual inductance We can gain a significant improvement in speed from the realization that the mutual inductance of two coils (1 and 2) [45], defined by the Neumann formula

$$M_{12} = \frac{\Phi_1}{i_2} = \frac{\mu_0}{4\pi} \oint\oint \frac{d\mathbf{l}_1 \cdot d\mathbf{l}_2}{|\mathbf{r}_1 - \mathbf{r}_2|} = \frac{\Phi_2}{i_1} = M_{21}, \tag{4.3.2}$$

contains all the relevant geometric information. Equation Eq. (4.3.1) then becomes

$$\mathscr{E} = -M\frac{di}{dt}. \tag{4.3.3}$$

Moreover, there is a closed expression for the mutual inductance of two parallel straight filaments [46–48] that is particularly suited for fast implementation as a forward model:

$$\begin{aligned} M = \frac{\mu_0}{4\pi}\Bigg[& \alpha \operatorname{argsinh}\frac{\alpha}{d} - \beta \operatorname{argsinh}\frac{\beta}{d} - \gamma \operatorname{argsinh}\frac{\gamma}{d} + \delta \operatorname{argsinh}\frac{\delta}{d} \\ & - \sqrt{\alpha^2+d^2} + \sqrt{\beta^2+d^2} + \sqrt{\gamma^2+d^2} - \sqrt{\delta^2+d^2}\Bigg], \end{aligned} \tag{4.3.4}$$

where the geometric parameters are defined as shown in Fig. 4.19. Equation 4.3.4

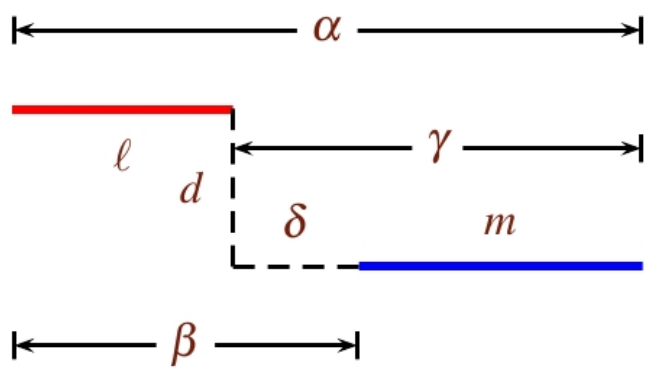

Figure 4.19: Geometry for (4.3.4).

contains only elementary functions, which are readily available and whose computation has been standardized and optimized for speed and accuracy. The integration is done implicitly at full accuracy, making it unnecessary to keep track of the number of integration points. Moreover, much time is saved because the procedure is exempted from carrying out unnecessary calculations: the volume integration requires that we compute the field at hundreds of points, and in most

of them only one of the three components is needed, which means that two thirds of the computations are wasted when the normal algorithm is employed. Finally, there is no risk of obtaining divergent values because the relative height d is always guaranteed to be nonzero. (When the receivers are placed flat on the transmitters, the center-to-center difference in altitude is 8.99 cm, due mainly to the plastic lids that both transmitters and receivers have and whose widths are respectively $3/16in.$ and $1/4in.$.) Do note, however, that the procedure assumes that the transmitters and receivers have parallel axes; that is its main limitation.

Equation Eq. (4.3.4) can be extended to squares, and in turn to Pedemis's arrays of stacks of transmitter and receiver coils. The parameters α, β, γ, δ, and d change with every point as the receivers are moved around when taking measurements, and it is necessary to perform some bookkeeping. Table 4.20 shows how the complete inductance is to be calculated for a given relative location.

The whole operation can be implemented in Matlab without using loops and runs some 500 times faster than the conventional integration. This suggests that it is possible to incorporate the inductance-based positioning algorithm into the following protocol:

1. Use the code in the single-coil area-integration limit (it does not compute the point-receiver limit) to optimize with several different starting points.
2. Use the best result of (1) to start the optimizer with the full detailed structure. It can be run just once.
3. If rotations are required, one can feed the best result of (1) or (2) into a forward model that includes them.

It is thus possible to incorporate the 30 turns in each transmitter, the 10 turns in each receiver, and the fact that there are 9 of each, and still get real-time receiver positioning. The next section will show the performance of the procedure on a set of measurements carried out with Pedemis at an actual UXO site.

4.3.b.(3) Mutual Induction Based Positioning Results Personnel from the Cold Regions Research and Engineering Laboratory and G&G Sciences took data at the Aberdeen Proving Ground in Maryland between 5 and 16 November 2012. The measurements, reported and described in more detail elsewhere in these proceedings [38], comprised among others a set of static measurements over 257 cells—five shots per measurement for a total of 1285 data shots. Several cells were selected for deeper interrogation, and a few dynamic measurements were carried out. Data were also taken in an indirect-fire and mogul areas (see Sec. 5.4.e).

The static measurements were taken at five different receiver locations: Position 1 is at the center of the transmitter grid and Positions 2 through 5 correspond to the receiver assembly's being placed at each of the four quadrants (and are numbered in the same order) so that their outer edges are aligned; the centers of the assemblies are thus separated by 32 cm in each direction, for a total separation of $32\sqrt{2}$ cm. Positions 2 and 4 are shown on Figure 4.21. The locations were fixed in that fashion in order to streamline the data-taking process enough to finish all the needed measurements on time. The positioning algorithm, then, was not a critical part of the data-taking, but was still necessary to provide analysts with the necessary background file to subtract for target discrimination.

After reading the on-time data we select the time gate. Recall that to comply with Faraday's Law Eq. (4.3.1) we must multiply by the time derivatives of the currents, which change from transmitter to transmitter. The receivers saturate when the magnetic flux goes beyond a certain value (about 8 mV), and faint signals have low signal-to-noise ratio. It is desirable to find a gate that has as many signals as possible that strike the right balance in magnitude. The next step is to differentiate the currents: we use cubic splines to find piecewise polynomials that interpolate them and differentiate the polynomials. The gate-selection and current-differentiation processes have been fully automated.

Figures 4.22 to 4.26 show a sequence of five measurements (Nos. 00236 through 002450) made on 7 November at the APG blind grid. The plots show the currents and on-time primary fields for all transmitters and receivers, the spline-computed derivatives, and the data picked up by the receivers at the chosen gate. The solid lines in the flux plots are the measured values, while the markers are the flux predictions for the receiver location. The measured values that do not have markers associated with them correspond to saturated receivers or measurements with small SNR that were not used in the calculations. The predictions of the positioning scheme agree quite well with the actual measurements, in this set of five and in all the other static cases.

4.3.b.(4) Conclusion In this section we have presented a procedure that could help provide real-time positioning for the Pedemis system as it strives to detect, identify, discriminate, and classify UXO in real time in difficult terrain. The positioning system samples the on-time primary field of the transmitter array and uses optimization to find the location that best describes the combination of secondary-flux time decays measured component-to-component by the receiver array. The

positioning protocol complies fully with Faraday's law, takes into account the coil fine structure of both assemblies, needs no adjustable parameters and thus does not require any monitoring, and contains only well-known elementary functions, which guarantees its high accuracy, quick execution time, and solid reliability.

The procedure is not the last word, however, because it has a major limitation: it requires the transmitters and receivers to have parallel axes. In limited tests we have found that our routine yields reasonable location estimates when the receiver assembly is tilted, though these are not as accurate as would be desirable. In any event, there is a solution for skew filaments [49, 50] that could be used as a basis for a completely general locator. Its implementation is not trivial, though, and the bookkeeping is more complicated than for the cases we have treated in this section.

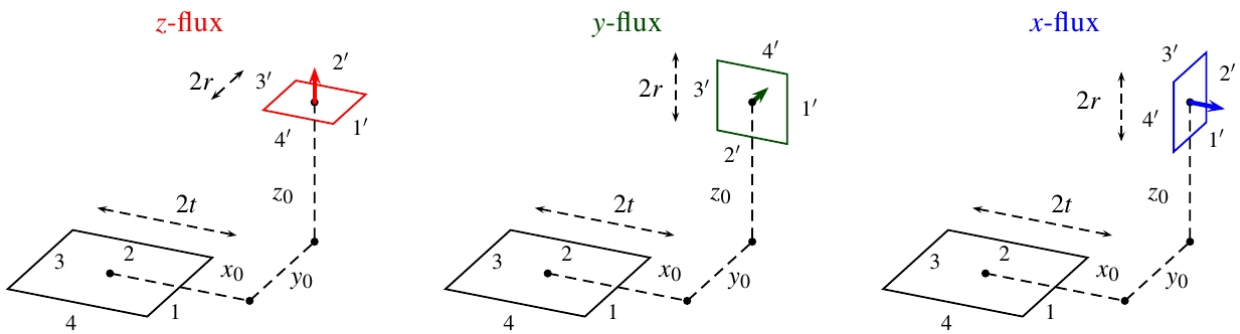

Flux	Pair	α	β	γ	δ	d^2
z	$11'$	y_0+r+t	y_0+r-t	y_0-r+t	y_0-r-t	$(x_0+r-t)^2+z_0^2$
	$13'$	y_0+r+t	y_0+r-t	y_0-r+t	y_0-r-t	$(x_0-r-t)^2+z_0^2$
	$33'$	y_0+r+t	y_0+r-t	y_0-r+t	y_0-r-t	$(x_0-r+t)^2+z_0^2$
	$31'$	y_0+r+t	y_0+r-t	y_0-r+t	y_0-r-t	$(x_0+r+t)^2+z_0^2$
	$22'$	x_0+r+t	x_0+r-t	x_0-r+t	x_0-r-t	$(y_0+r-t)^2+z_0^2$
	$24'$	x_0+r+t	x_0+r-t	x_0-r+t	x_0-r-t	$(y_0-r-t)^2+z_0^2$
	$44'$	x_0+r+t	x_0+r-t	x_0-r+t	x_0-r-t	$(y_0-r+t)^2+z_0^2$
	$42'$	x_0+r+t	x_0+r-t	x_0-r+t	x_0-r-t	$(y_0+r+t)^2+z_0^2$
		$M_z = M_{11'} - M_{13'} + M_{33'} - M_{31'} + M_{22'} - M_{24'} + M_{44'} - M_{42'}$				
y	$22'$	x_0+r+t	x_0+r-t	x_0-r+t	x_0-r-t	$(y_0-t)^2+(z_0-r)^2$
	$24'$	x_0+r+t	x_0+r-t	x_0-r+t	x_0-r-t	$(y_0+t)^2+(z_0-r)^2$
	$44'$	x_0+r+t	x_0+r-t	x_0-r+t	x_0-r-t	$(y_0+t)^2+(z_0+r)^2$
	$42'$	x_0+r+t	x_0+r-t	x_0-r+t	x_0-r-t	$(y_0-t)^2+(z_0+r)^2$
		$M_y = M_{22'} - M_{24'} + M_{44'} - M_{42'}$				
x	$11'$	y_0+r+t	y_0+r-t	y_0-r+t	y_0-r-t	$(x_0-t)^2+(z_0-r)^2$
	$13'$	y_0+r+t	y_0+r-t	y_0-r+t	y_0-r-t	$(x_0+t)^2+(z_0-r)^2$
	$33'$	y_0+r+t	y_0+r-t	y_0-r+t	y_0-r-t	$(x_0+t)^2+(z_0+r)^2$
	$31'$	y_0+r+t	y_0+r-t	y_0-r+t	y_0-r-t	$(x_0-t)^2+(z_0+r)^2$
		$M_x = M_{11'} - M_{13'} + M_{33'} - M_{31'}$				

Figure 4.20: Pairs of filaments that have to be summed as part of the mutual-inductance positioning algorithm. The parameters α, β, γ, δ, and d change with every point as the receivers are moved around when taking measurements.

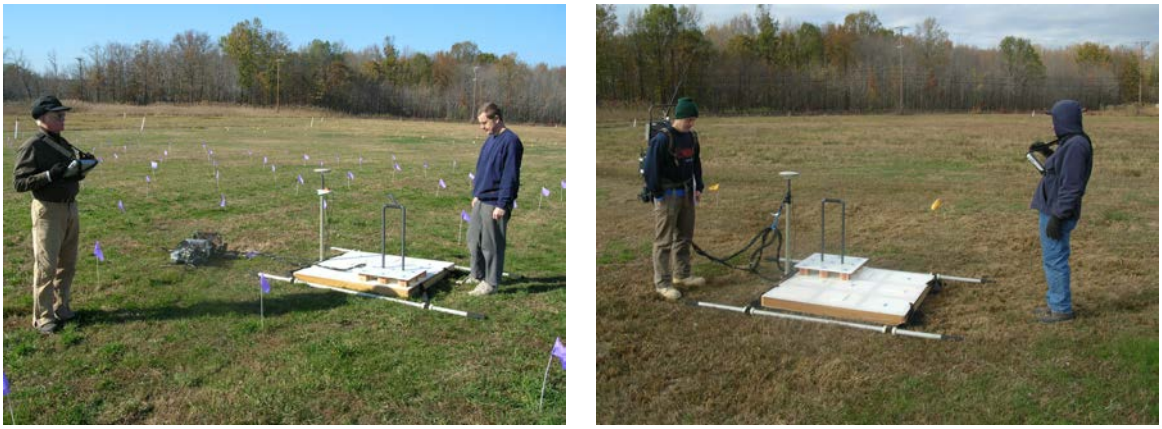

Figure 4.21: Data collection with Pedemis at the Aberdeen Proving Ground. Shown are two instances of static measurements taken at Position 2 (left) and Position 4 (right).

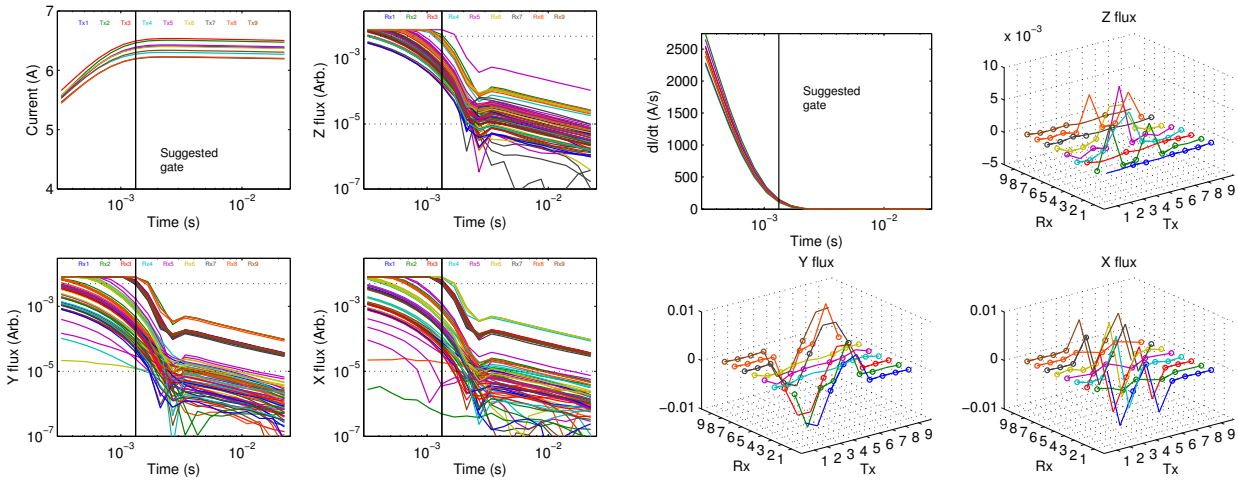

Figure 4.22: APG static measurement #00236: The program suggests Gate #7 (1324 µs) and predicts the Rx to be at Position 1.

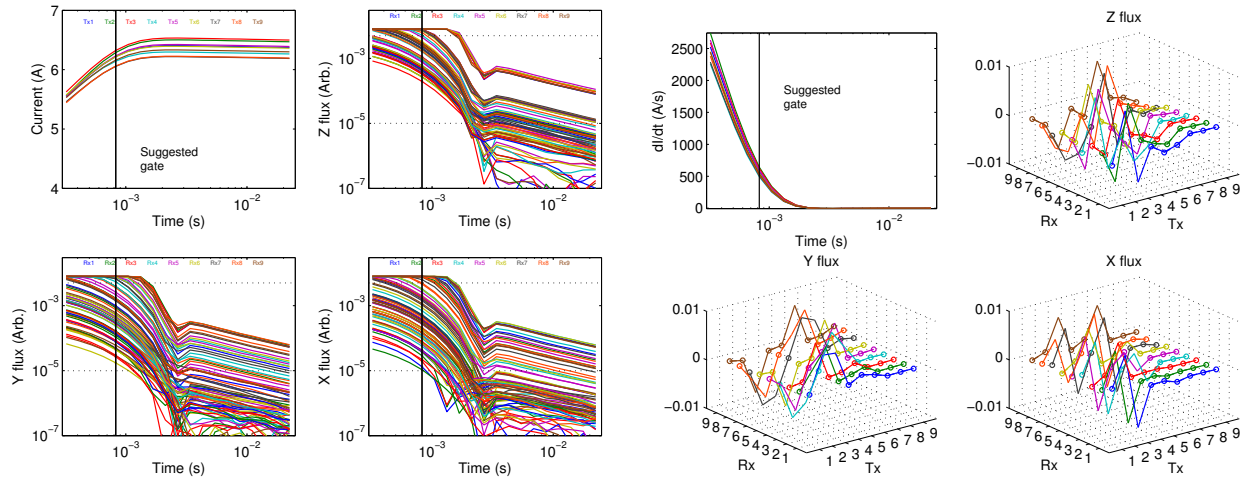

Figure 4.23: APG static measurement #00237: The program suggests Gate #5 (826 µs) and predicts the Rx to be at Position 2.

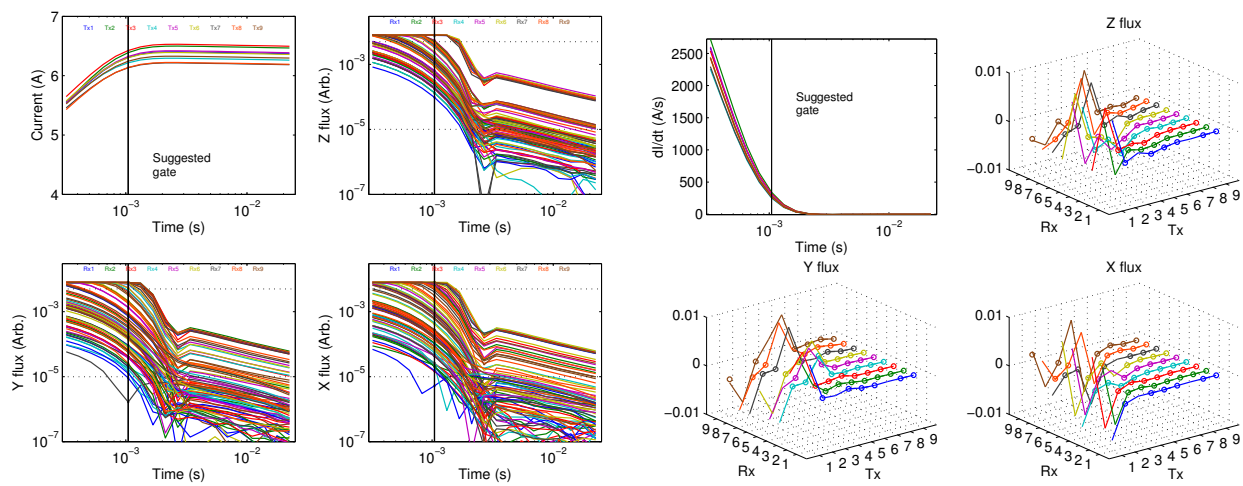

Figure 4.24: APG static measurement #00238: The program suggests Gate #6 (1046 µs) and predicts the Rx to be at Position 3.

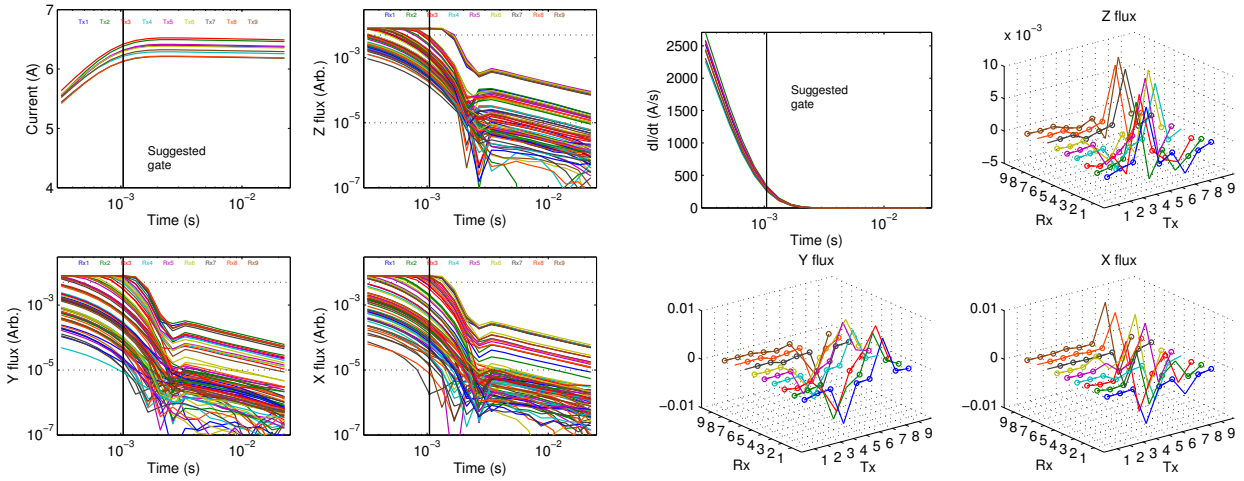

Figure 4.25: APG static measurement #00239: The program suggests Gate #6 (1046 µs) and predicts the Rx to be at Position 4.

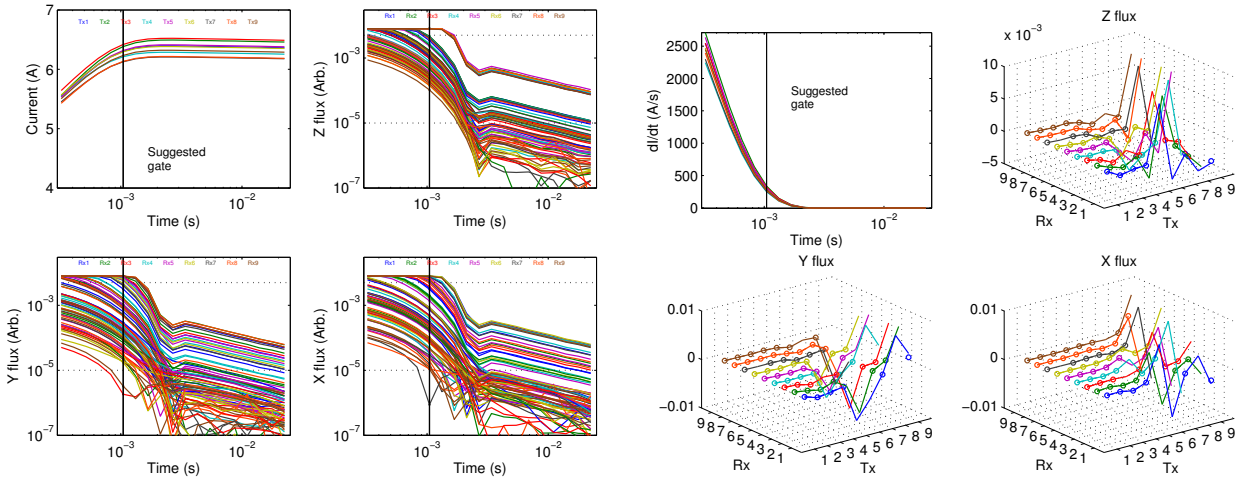

Figure 4.26: APG static measurement #00240: The program suggests Gate #6 (1046 µs) and predicts the Rx to be at Position 5.

4.4 Background Subtraction

All EMI instruments generally have to account for background noise when acquiring data or the results may be poor or corrupted. With all prior EMI instruments, the transmitter(s) and receiver(s) have been in a fixed geometry with respect to each other, so acquiring a background shot was a relatively simple matter of finding a quiet location and acquiring a data shot. Because the Tx and Rx arrays on Pedemis are not in a fixed geometry, the "background" is not as simple to acquire and remove from the data. Background due to instrument noise is one type of background that we would definitely like to remove from Pedemis data. But if the Rx array is at all moved off from a prior location, the instrument noise will change dramatically mainly because the Tx coils are so close to the receivers. These Tx could can act like targets themselves, but their influence in the EMI data is considered instrument noise and is undesirable.

We installed guides on the top of the Tx array to limit the Rx array to standard locations for most of the data acquisition of Pedemis (see Fig. 4.27). These guides

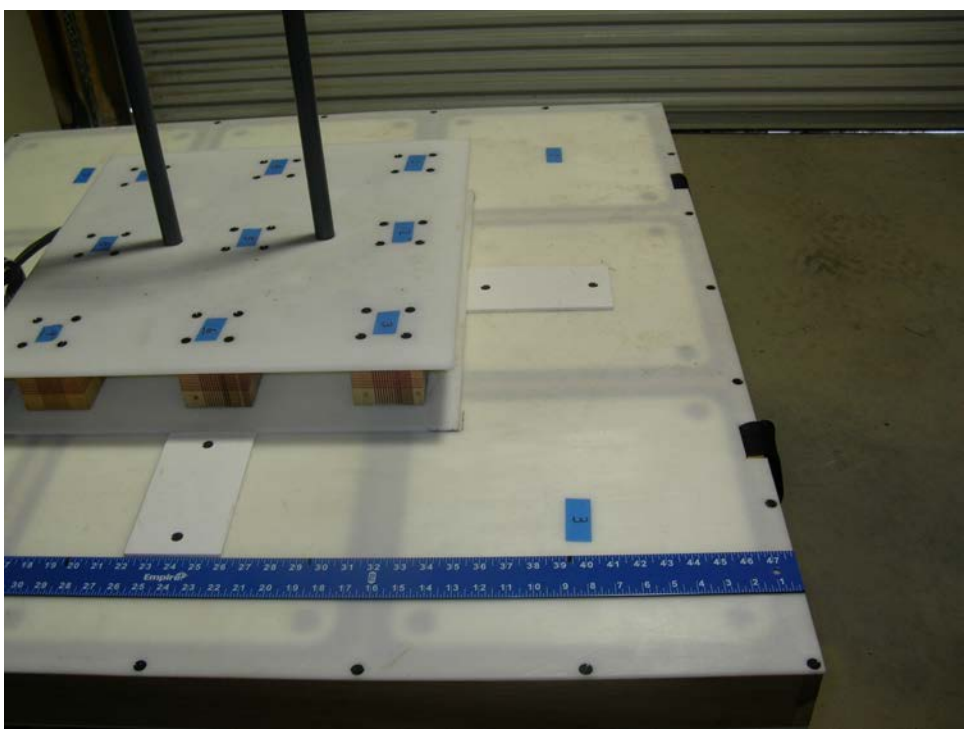

Figure 4.27: Pedemis guides for the Rx array on top of the Tx array. This helped reduce Rx location errors and thereby helped reduce background noise.

helped reduce Rx location errors and thereby helped reduce background noise.

For the general case of an arbitrary Rx array location, our plan to remove this

noise could center on simply taking thousands of measurements and interpolating between them in the 6-space consisting of Pedemis's 3D location in space and its current 3 Euler angles. Not only is that laborious, but trying to get that many measurements, including in the 2 meters outside the Tx array could take years even on an automated platform like the ERDC test stand.

Instead, we plan to reproduce the response (AKA instrument noise or instrument background) from the Tx coils using an equivalent source approach similar to the NSMS method. These equivalent sources are found from a much smaller set of normal background measurements at known locations. Once this set of sources is known, the time domain response from the coils (as represented by the sources) can be quickly calculated anywhere in space. The location of the Rx array are known from the Pedemis beacon type positioning as described in Sec. 4.3. Any future background type measurements in the air were added to the training routine for the equivalent sources and their accuracy was improved. This instrument background subtraction routine were built into Pedemis so that any data collected by Pedemis had this instrument noise removed before recording the data. Note that this solution for this instrument noise does not address the issue of geological noise in the EMI due to the soil. Note that this part of the project was not completed due to time and budget constraints. For the data acquired at APG, this background removal method was not needed except in a few test cases in the mogul area (see Fig. 5.34).

4.5 Pedemis Operation Protocol

There are several data collection protocols for using Pedemis depending on whether Pedemis was used for detection and cued interrogation, and what the data quality is over each target. If Pedemis is to be used for the detection segment of the survey, then Pedemis is put into detection mode (see below for mode descriptions) until an anomaly is detected. Once detected, Pedemis is the placed over the anomaly, and data is acquired in cued interrogation mode #1. After this data is collected, a determination is made whether Pedemis should either 1) enter interrogation mode #2 (for widespread multiple targets) or #3 (for deep targets) or data collection over this anomaly should conclude.

Pedemis has the following data collection protocols:

- **Detection Mode –** Data is acquired at 3 samples per second as Pedemis is transported over the ground. A plot of the z-component of the magnetic field is displayed in real time on the controlling device to facilitate anomaly detection. The Rx array is centered on the Tx array and fixed in position.

- **Cued Interrogation Mode #1 (CIM1) –** This mode directly follows a detection. Pedemis is set down centered over the anomaly with the Rx array still fixed in position. A static data shot using all nine Tx coils and all 9 receivers in this configuration is then taken. This data shot takes around 30 seconds. Depending on the results of this data, users follow one of the following three courses of action:

  1. *Enter Cued Interrogation Mode #2*
  2. *Enter Cued Interrogation Mode #3*
  3. *Resume Detection Mode*

- **Cued Interrogation Mode #2 (CIM2, for multiple and/or widespread targets) –** Based on the data from cued interrogation mode #1 using the JD method, a determination is made (at first by expert users, later by computer algorithm) whether there are multiple and/or widespread targets in the field of view of Pedemis. If this is the case, then this interrogation mode is used. In this mode, the Rx array is positioned first in the center, then near each of the four corners of the Tx array in sequence (see the sketch in Fig. 4.28 and Fig. 4.29) for four 30 second data shots. Total time for this interrogation is

about 2 minutes. This mode provides an equivalent 6x6 array of vector magnetic field values from 9 independent transmitters over a 1.2m square area. These four positions avoid the Tx coils as much as possible (3.5cm smallest lateral separation) while yielding a uniform 6x6 composite data shot.

- **Cued Interrogation Mode #3 (CIM3, for deep targets) –** This cued interrogation mode is used if deep targets seem to be present, but the data is not of sufficient SNR to make a reliable classification of the target. For this mode, the Rx array is left in the center of the Tx array (as in detection and cued #1 modes), but a longer data shot is acquired in order to integrate more samples and thus increase SNR for deep targets. This data shot may take up to 5 minutes to complete depending on the desired SNR.

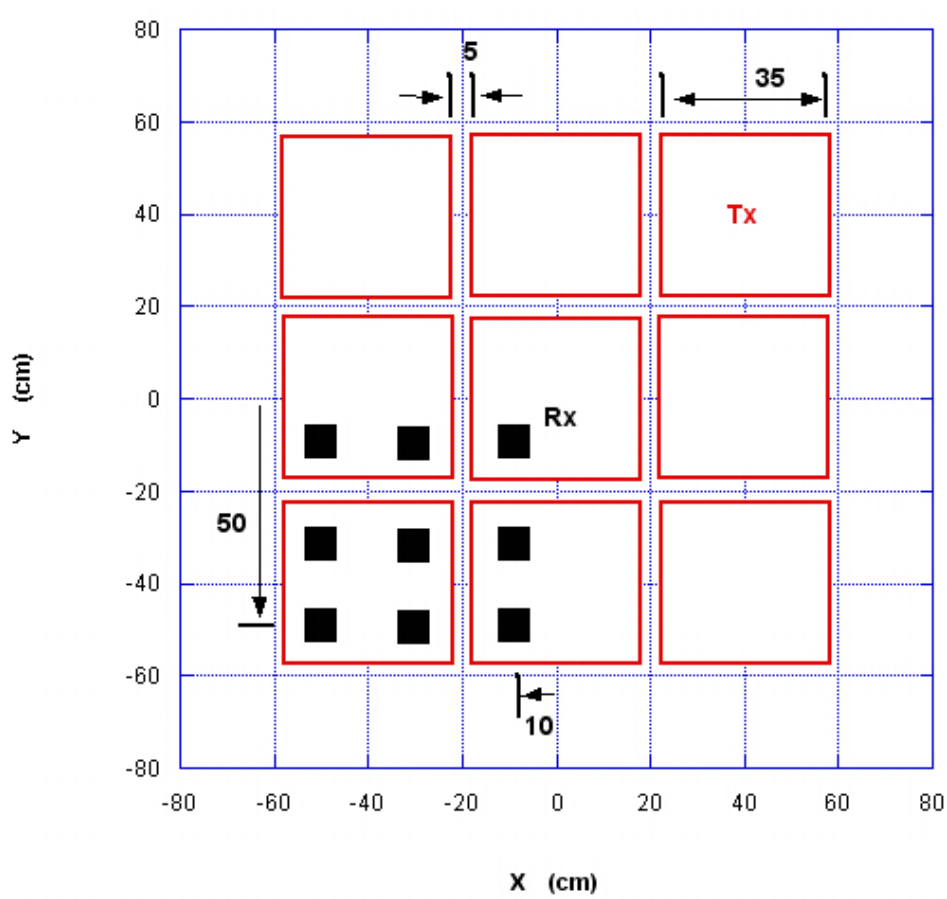

Figure 4.28: Pedemis DAQ Position #1 sketch. 35cm transmitters with 5cm spacing. The 50cm Rx array is shown in the lower left quadrant (AKA position "#1" of 4). These four positions avoid the Tx coils as much as possible while yielding a uniform 6x6 composite data shot.

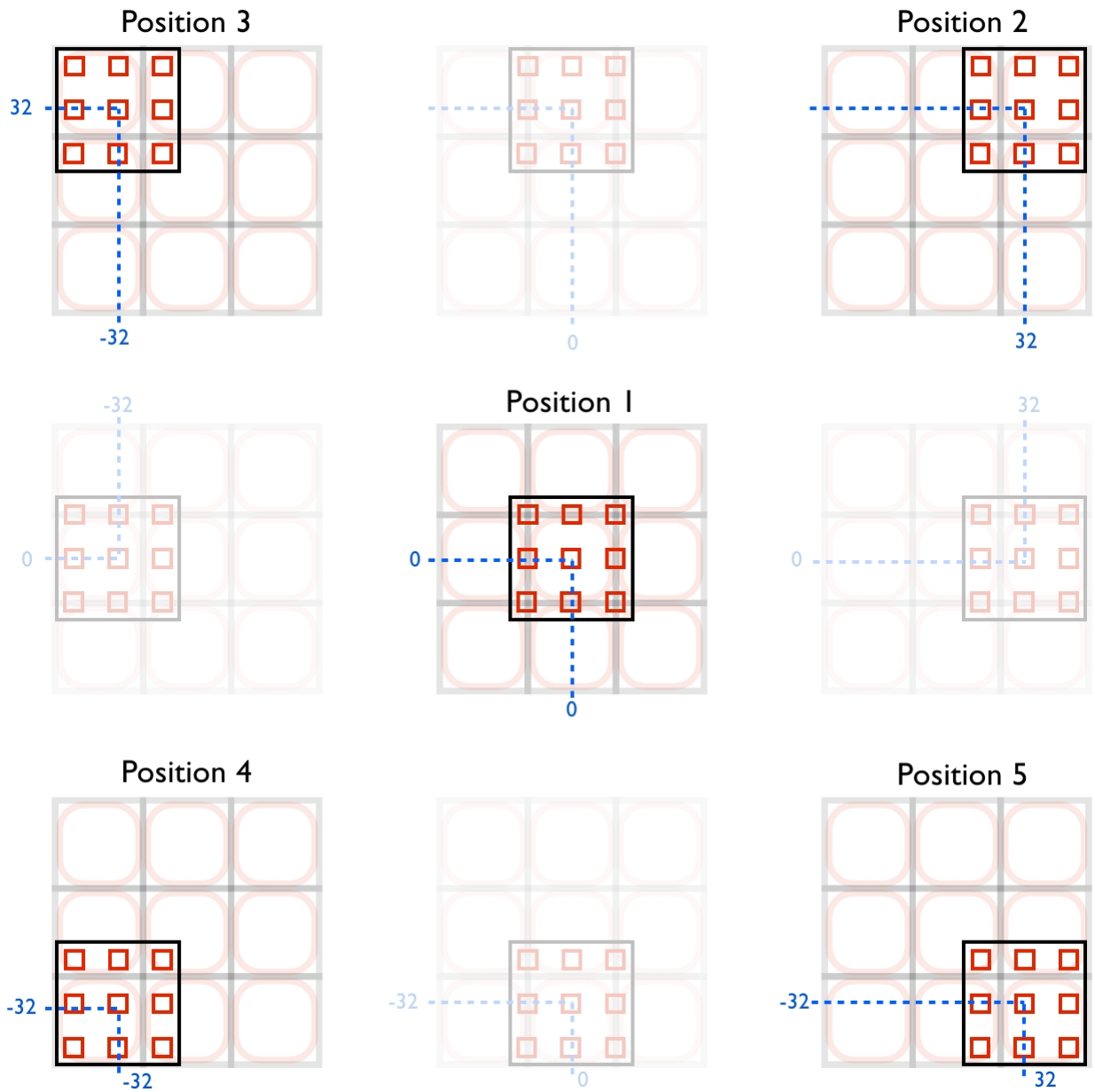

Figure 4.29: Pedemis DAQ Positions.

During MR-1712, the determination of which data protocol to follow is made by expert users, however we hope to be able to systematize the decision process into computer algorithms in future Pedemis work.

Our standard interrogation protocol during either static or dynamic mode [51] starts by positioning the Rx array in the middle of the Tx array and detecting signals based on an amplitude threshold with only the central transmitter firing. The sensor uses a square wavefront composed of four quarter cycles: 'on pos-

itive', 'off', 'on negative', and 'off', as shown in Figure 4.30. After each 'on' quarter cycles, data are collected during the corresponding 'off' quarter cycles, and are negative of each other due to the inverted excitations. During the data collection window, however, ubiquitous 60 Hz interference signals $s_{60}(t)$ are also measured and need to be canceled, suggesting the use of a total data collection time of 33.33 ms as in Figure 4.30(a), or its multiples such as 100 ms in Figure 4.30(b) which has been historically chosen. During both 'on' time intervals, a primary field is applied and induces eddy currents in the targets. During both 'off' time intervals, the eddy currents produce the secondary magnetic field which is therefore collected for 100 ms/4=25 ms.

The cued interrogation protocol is then set as follows:

(1) Cued interrogation mode 1: again only the central transmitter (Tx 5) is active with the Rx array centered. The secondary magnetic field is collected for 360 cycles of 100 ms each. A JD plot is available after this data is collected to aid the expert operator in their decision to either:

1. resume dynamic interrogation
2. enter Cued interrogation mode 2, or
3. enter Cued interrogation mode 3

(2) Cued interrogation mode 2: if a weak signal is detected in (1), a broader deep interrogation ensues with Tx 2, 4, 6, and 8 active for the same central Rx array position, again using 360 repeats for each Tx resulting in 36 s $\times$ 4 = 144 s. This data is combined with mode 1 data if available.

(3) Cued interrogation mode 3: if detection is clear in (1), data are collected with all transmitters sequentially active, at each of five Rx array positions: centered as shown in Fig. 4.32, aligned top-right, top-left, bottom-left, and bottom-right with the edge of the Tx array. A total of 30 repeats are used for each Tx and each location of the Rx array, resulting in an acquisition time of 3.0 s $\times$ 9 $\times$ 5=135 s.

The actual operator time spent is therefore 36 s in detection (1), then either 144 s in interrogation (2) or 135 s in interrogation (3). A flowchart of the data acquisition process is shown in Fig. 4.31. In addition, several corresponding data shots are collected in the absence of targets in order to provide the reference background data necessary for the subtraction of repeatable noise sources. Including time to

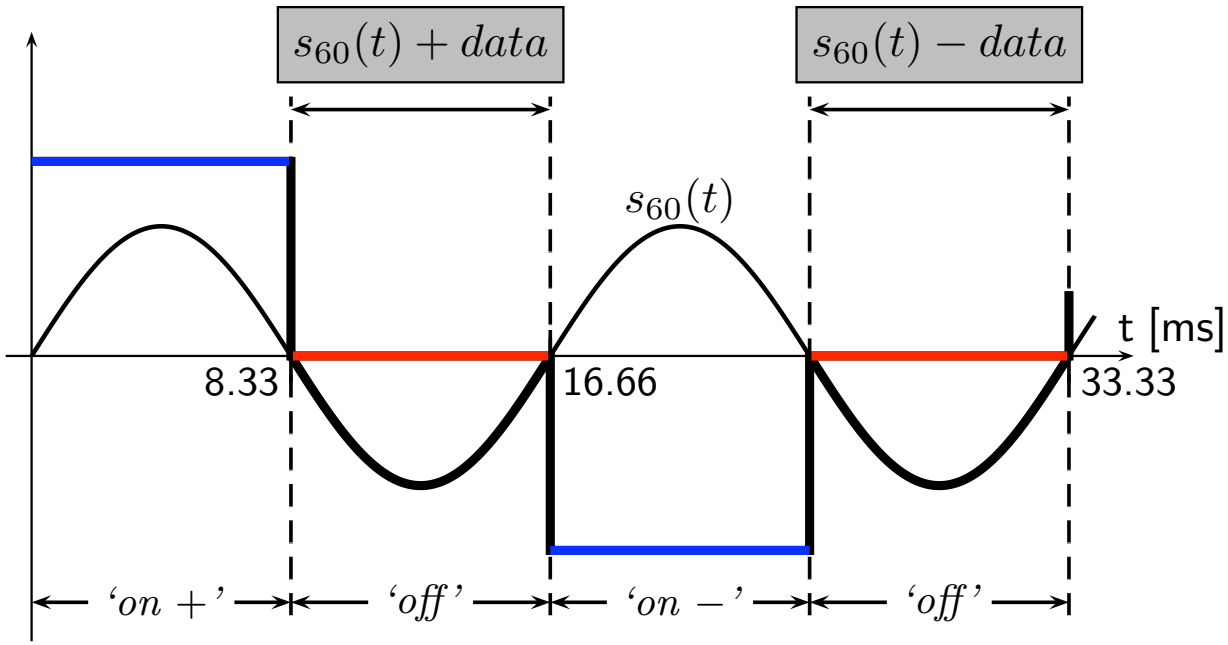

(a) Data collection window of 33.33 ms.

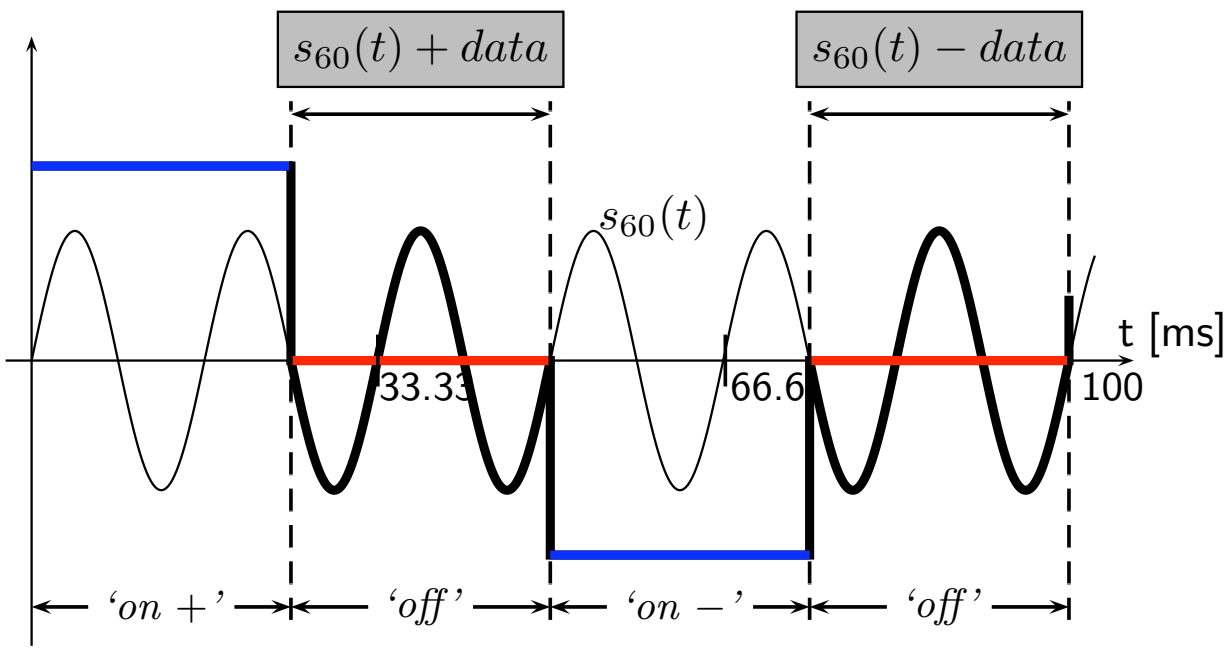

(b) Data collection window of 100 ms.

Figure 4.30: Rectangular wavefront of the Pedemis sensor in order to reject 60 Hz harmonics. The primary field is applied during the 'on' quarter cycles and the data are collected during the 'off' quarter cycles. Along with the data, 60 Hz interference signals – denoted by $s_{60}(t)$ – are also measured and can be canceled by subtracting the two data collection windows. The cancellation is perfect if the data collection window spans multiples of 33.33 ms as in (a), for example 100 ms as in (b). The cancellation remains effective for harmonics of 60 Hz.

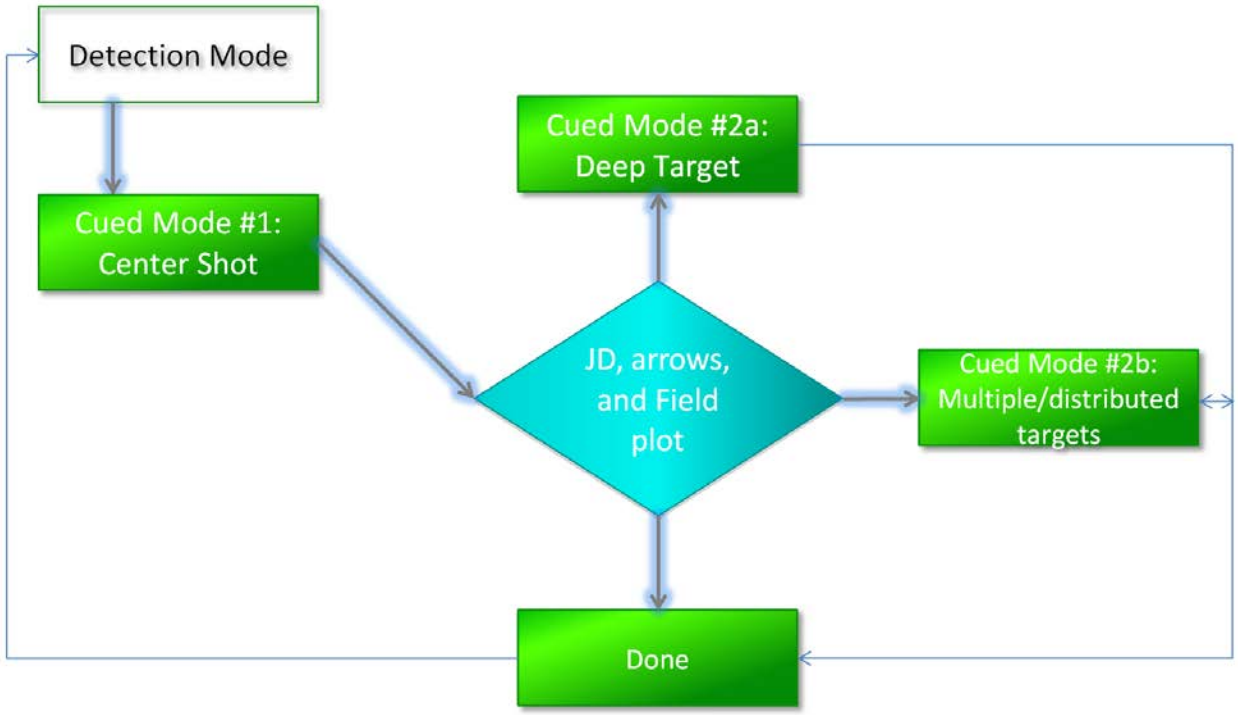

Figure 4.31: Data acquisition flowchart for Pedemis operation.

move the sensor and related hardware, we have averaged about 20 targets per hour during our survey at APG (see Sec. 5.4).

4.6 ONVMS Applied to Pedemis

In order to take into account the data quality and diversity that Pedemis provides, we adapted the advanced EMI model, called the Ortho-Normalized Volume Magnetic Source technique (ONVMS), to be used with the Pedemis data. The ONVMS approach is a further extension of the Normalized Surface Magnetic Source (NSMS) model, based upon the assumption that the secondary magnetic field of a buried object, interrogated by a sensor, can be replaced with a superposition of fields originating from a set of sources (usually magnetic dipoles) distributed over a volume. Since all physical radiating sources are located inside the scatterers - rather than in the soil or air - the spatial distribution of these fictitious dipoles indicates the locations and orientations of any targets present inside the computational volume. The great advantage of the ONVMS technique over other models is that it takes into account mutual couplings between different sections of different targets,

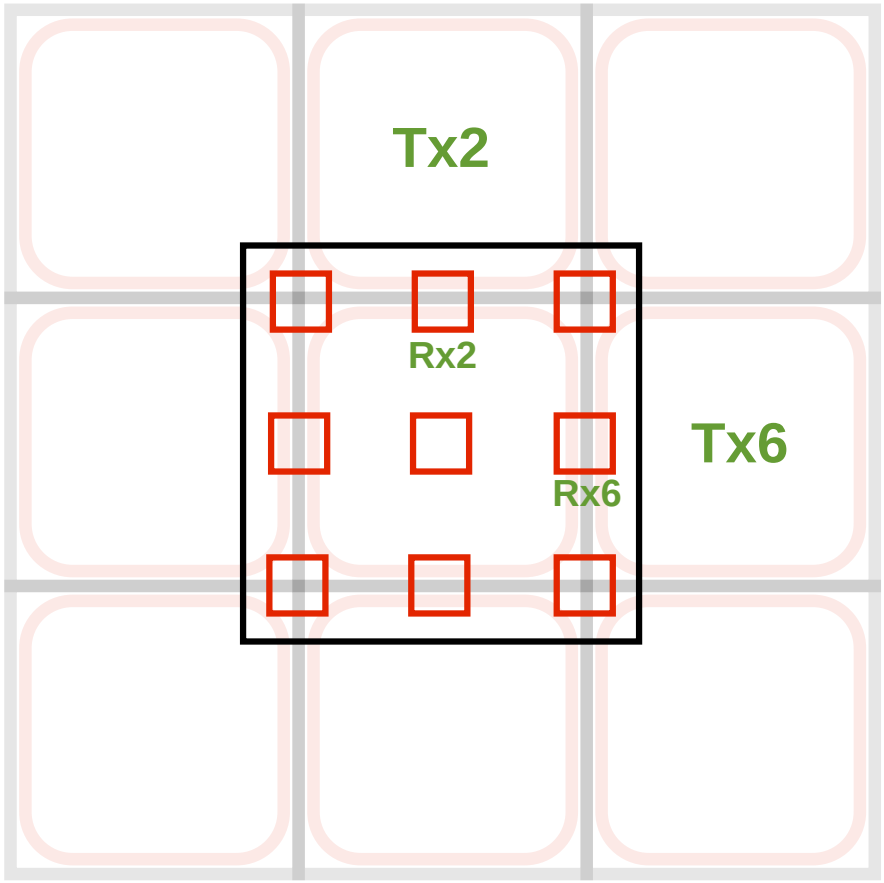

Figure 4.32: Detection configuration: the Rx array is located at the center of the Tx array and the sensor is essentially used to detect signals based on an amplitude threshold. In a cued interrogation mode, the Tx array is centered over the potential target and signals are collected at various Rx array positions.

while simultaneously avoiding the appearance of singular matrices in multi-target situations. It is, thus, gracefully indifferent to the number of targets: once the amplitudes and the locations of the corresponding dipoles are determined, one need only look at their clustering patterns, compute the time-dependent total polarizability tensor for each group, and subsequently diagonalize each such tensor using the joint diagonalization procedure [3]. The resulting diagonal elements have been found to be intrinsic to the objects they represent, and can be used, on their own or combined with other quantities, in discrimination analysis. Recent ESTCP live-site discrimination studies have clearly indicated the superior discrimination performance of the ONVMS method in combination with the statistical processing approaches described [5, 6, 52]. In this section, we demonstrate first time the applicability of the OVNMS method to the Pedemis data.

4.6.a Pedemis and ONVMS Modeling

The Pedemis transmitters are modeled as infinitely thin rectangular wires. The primary magnetic field produced at any observation point $\mathbf{r}$ by the T-th loop is determined simply from the Biot-Savart law,

$$\mathbf{B}_T(\mathbf{r}) = \frac{\mu_0}{4\pi}\sum_{i=1}^{N_{Tx}} \frac{I_T[\Delta\ell_{T,i}\times\mathbf{R}_{T,i}]}{R_{T,i}^3},\ T = 1,2,...,9, \tag{4.6.1}$$

where, $\mathbf{R}_{T,i} = |\mathbf{r}-\mathbf{r}\prime_{T,i}|$, $\mathbf{r}\prime_{T,i}$is the location of the i-th current element, and $\Delta\ell_{j,i}$ is the tangential length vector for the i-th subsection of the loop. In what follows, and unless we note otherwise, we divide each transmitter coil into $N_{Tx} = 40$ subsections whenever we calculate the primary magnetic field using Eq. (4.6.1).

The Pedemis receiver array consists of 3x3 array of cubic sensors, with 20-cm neighbor-to-neighbor separation (see Figs. 4.10 and 4.11). Each sensor measures, along three orthogonal directions, the induced voltages that, by Faraday's law, correspond to the negative of the time derivative of the secondary magnetic field flux through the area spanned by the corresponding coils. The induced voltage in the R-th sensor along the α-th direction, where $R = 1,2,\ldots,9$ and $\alpha = z,y,x$, is computed using:

$$V_R^\alpha = -\int_{S_R^\alpha} \frac{\partial\mathbf{B}}{\partial t}\cdot d\mathbf{s}_R^\alpha = \sum_{i=1}^{N_{Rx}} \frac{\partial\mathbf{B}_i(\mathbf{r}_{i,R}^\alpha - \mathbf{r}_o)}{\partial t}\cdot\hat{\mathbf{n}}_\alpha \Delta s_{i,R}^\alpha, \tag{4.6.2}$$

where s_R^α is the area of the relevant coil (all of which are 8 cm × 8 cm squares) and $\hat{\mathbf{n}}_\alpha$ is the unit vector perpendicular to it, $\Delta s_{i,R}^\alpha$ and $\mathbf{r}_{i,R}^\alpha$ are, respectively, the

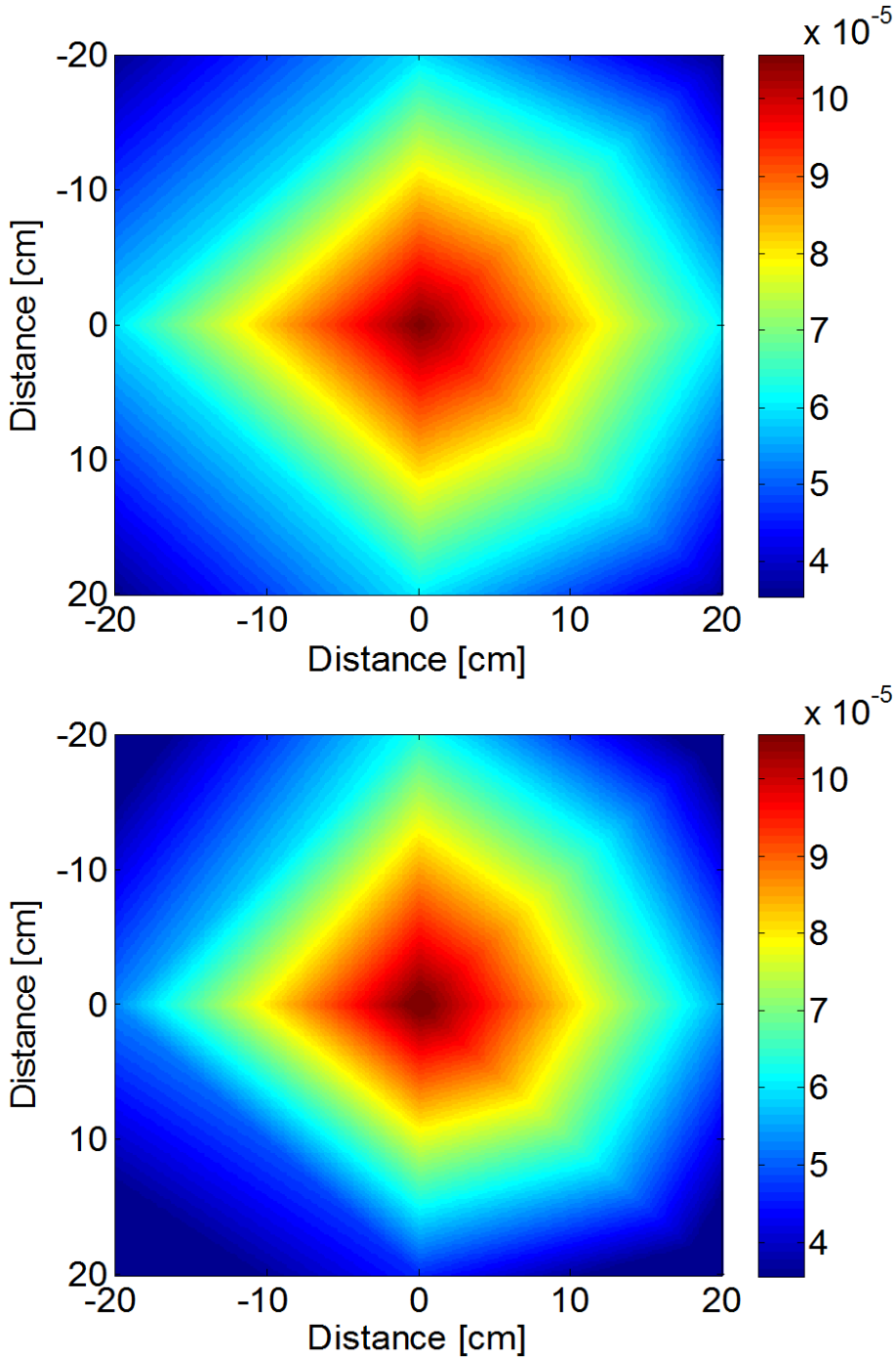

Figure 4.33: ONVMS-modeled (upper) and measured (lower) PEDEMIS data for a four inch diameter sphere at the 10th time channel. First row for Hy and second row for Hx magnetic fields. The sphere is placed at a depth of 36 cm to the PEDEMIS Tx array.

i-th sub-area and vector location point on s_R^α, $\mathbf{B}_i(\mathbf{r}_{i,R}^\alpha) = \mu_o \mathbf{H}_i(\mathbf{r}_{i,R}^\alpha)$ is the magnetic induction (proportional to the magnetic field $\mathbf{H}_i(\mathbf{r}_{i,R}^\alpha)$) produced at $\mathbf{r}_{i,R}^\alpha$ by a source placed at $\mathbf{r}_o$. We always divide s_R^α into $N_{Rx} = 4$ sub-areas.

4.6.b ONVMS Modeling Results

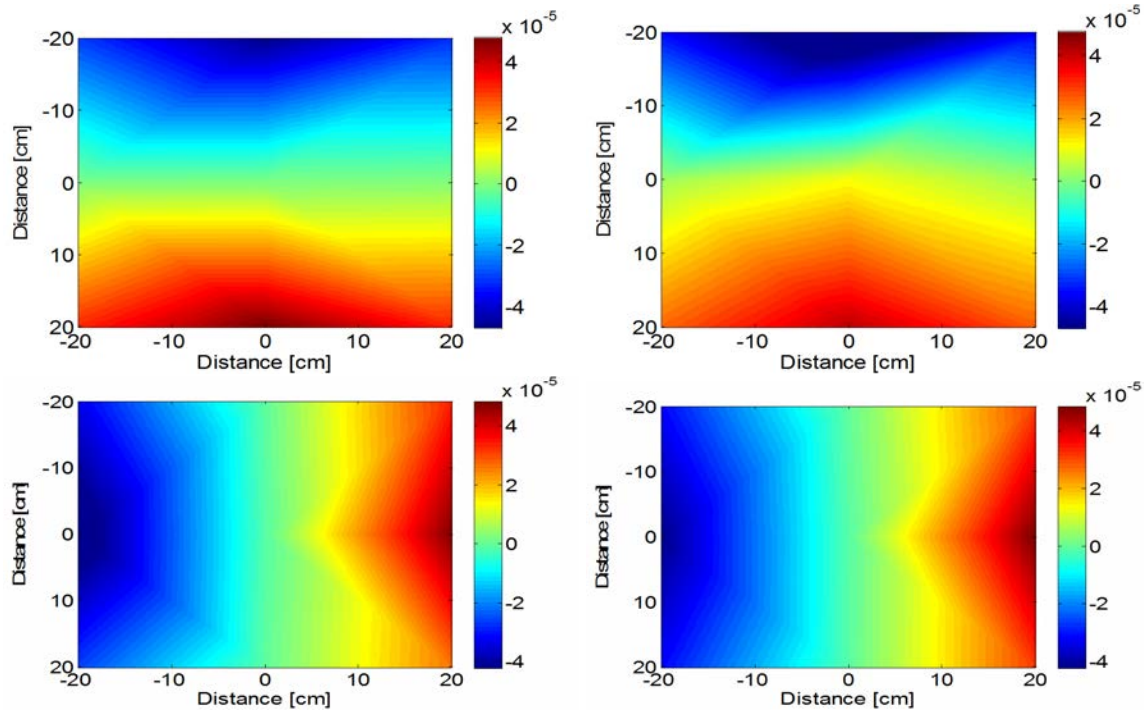

Figure 4.34: ONVMS-modeled (left) and measured (right) PEDEMIS data for a four inch diameter sphere at the 10th time channel. First row for Hy and second row for Hx magnetic fields. The sphere is placed at a depth of 36 cm to the PEDEMIS Tx array.

To validate the Pedemis versions of our advanced EMI codes we conducted comparisons between actual and measured data for a permeable 4-inch-diameter sphere. The sphere was placed 36 cm bellow the Pedemis Tx array. The measured and predicted magnetic fields for Tx# 5 (center) at all receivers, placed at the Pedemis center, are depicted in Figs. 4.33 and 4.34. The response of the sphere is approximated with a single ONVMS source, whose location is determined using the Differential Evolution (DE) algorithm. The inverted depth (35 cm) and lateral offsets match the actual location of the target very well. The model is seen to predict target EMI responses very accurately.

5 Results and Discussion

Pedemis was completely fabricated by the end of August, 2012. Here we present some further information on Pedemis, the data acquired with Pedemis, and some technical issues encoutnered and solved in the course of the project.

5.1 Pedemis DAQ Control Software

Pedemis can be controlled by two different programs: LabVIEW and EM3D from G&G Scineces, Inc. LabVIEW was chosen first as the controlling software because initially the NI cRIO was the electronics platform (see Appendix A.1). While we were able to acquire data in November, 2011 using the LabVIEW program interface, when we switched to a cDAQ platform, we were then able to use the more mature EM3D program to control the electronics on Pedemis. We used EM3D at APG to control Pedemis.

Our goal with the Pedemis control software in written in LabVIEW is to program such a robust, powerful, simple, yet flexible and intuitive interface based on the web browser concept of tabs for different functionality. For example, one tab or window of the browser would be dedicated to configuring data acquisition parameters for Pedemis. This tab would be available, but rarely used in the field. Another tab would display information regarding the current or next anomaly and would have a simple button for data collection, a comment box, and a field plot for checking proper operation of the receivers. Yet another tab could be for a more in depth analysis of the current data using techniques such as JD or a Gauss Newton multiple dipole search [2]. Any nearby web enabled device should be able to connect to and control Pedemis, from a smart phone to an iPad, to a laptop computer.

The cRIO-9022 controller communicates with the cRIO-9116 FPGA chassis both controlling it and receiving data from the modules. This RT controller will also host this webserver described above. Most of the calculations and higher level operations are controlled on the RT controller while the FPGA mainly specializes in collecting the data itself. Figure 5.1 shows part of the Virtual Instrument (VI) which runs on the RT controller.

The NI-9222 modules collect data from 4 channels at 500KS/s which is sufficient for the time bands we are interested in with Pedemis (100μs to 25ms). Seven of these modules are needed due to the 27 receiver channels from the nine triaxial receiver cubes, and another channel monitors the transmitter current. The

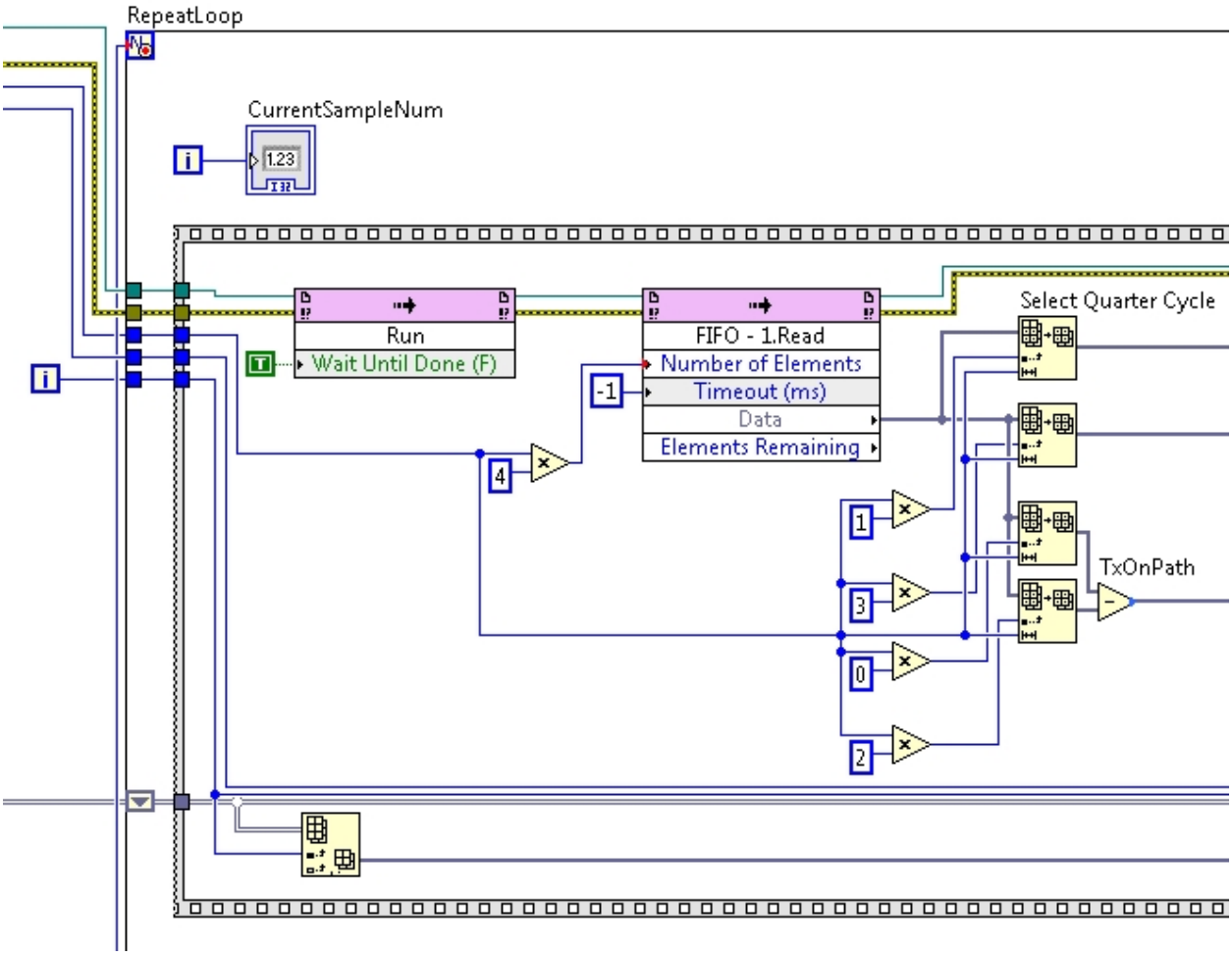

Figure 5.1: Partial view of Pedemis RT control software. This VI manages file I/O, runs the webserver, performs the averaging and data analysis, and controls most all functions except actual data collection itself which is handled on the cRIO-9116 FPGA chassis.

core function of the VI that runs on the cRIO-9116 FPGA chassis can be seen in Fig. 5.2.

Both the RT VI in Fig. 5.1 and the FPGA VI in Fig. 5.2 have what's referred to as a "front panel" that displays the information associated with each VI. The prototype front panel for the data collection reported in Sec. 5.2 performed with only minimum functionality, but was sufficient for acquiring data from Pedemis's 9 transmitters. This interface was continually improved throughout this project and will be throughout any follow-on work.

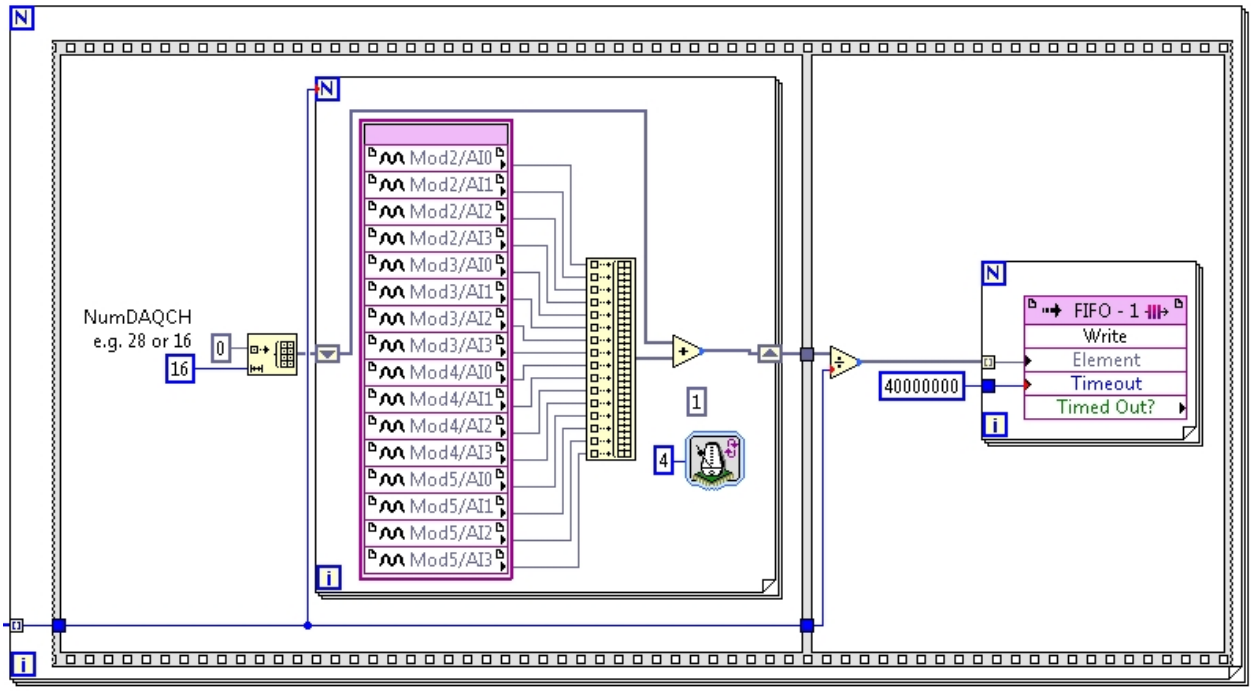

Figure 5.2: Pedemis FPGA control software. This VI

5.2 Initial Data, November 2011

We were able to collect initial proof of concept data outside of G&G Sciences office in Grand Junction, CO in November, 2011. Pedemis was not fully fabricated, and the main difference between the hardware used to collect these data and the finished instrument are as follows:

1. **Tx array –** The individual Tx coils were fabricated for this initial data, but the associated cabling had not been. As a result, we had to manually hook up each transmitter during data collection. As another result, because these coils were open circuit (if not the one being energized), they tended to have a longer than usual secondary z-component response for the receivers. Thus, the z-component of the received field is noisier than the x or y components in this initial data.

2. **Rx array –** The Rx array was fabricated, but the cabling to hook it up to the cRIO DAQ was not complete. Instead, we used the 5 receiver cubes and associated cabling of the MPV2 for this initial data. The MPV2 Rx cubes are the same design as the Pedemis cubes, so these preliminary results should be very similar to the production data once Pedemis is fully fabricated.

3. **Transmitter Control Board –** The transmitter control board was redesigned for Pedemis. For these initial data shots, we used the MPV2 transmitter control board.

4. **Analog Anti-aliasing Filters –** Likewise with the anti-aliasing filter boards, since these were redesigned for Pedemis, we used the MPV2 board.

We did use the cRIO based system with the LabVIEW VIs described in Sec. 5.1 to control the boards and sample the output of the Rx channels after the filter board (see Fig. 5.1). The core functionality of these VIs were improved during the remainder of the project, but the core control logic is complete.

Figure 5.3 show the data acquisition setup and process at Grand Junction, CO in November, 2011. Data was collected (a "shot") at 5 MPV2 positions over the

Figure 5.3: Initial data setup in Grand Junction CO in November, 2011. The MPV2 receivers were used as the Pedemis Rx cabling was incomplete.

Tx array with all 9 transmitters firing in turn. In terms of orientation, the MPV2

handle is pointing in the negative y direction. Four total data shots were collected:

1. A background shot
2. A shot over a 4 inch steel sphere. The sphere was located at depth 26 cm (to nearest point on sphere) under the corners of the four upper left transmitters.
3. Positioning test shot with no target. For this shot, the MPV2 sensor head was left in one location (at the bottom right corner of the Tx array) while all nine transmitters fired in turn. This was to test the positioning algorithms in Sec. 4.3 with no target present.
4. Positioning test shot with no target. This time, the MPV2 sensor head was outside the Tx array to the left.

The initial data was analyzed for satisfactory SNR and reasonableness in our lab. Figure 5.4 shows the raw data from the 5 MPV2 receivers situated in the top left corner of the Tx array and the center transmitter firing. As expected, the z-components of the received magnetic field are more noisy than the x or y components due to the open terminals at the remaining transmitter terminals. Note that we integrated and averaged one hundred 10Hz measurements for these data. Using our Gauss-Newton dipole inversion routine [2], we get the polarizabilities shown in Fig. 5.5 using only the x and y components of the received magnetic field.

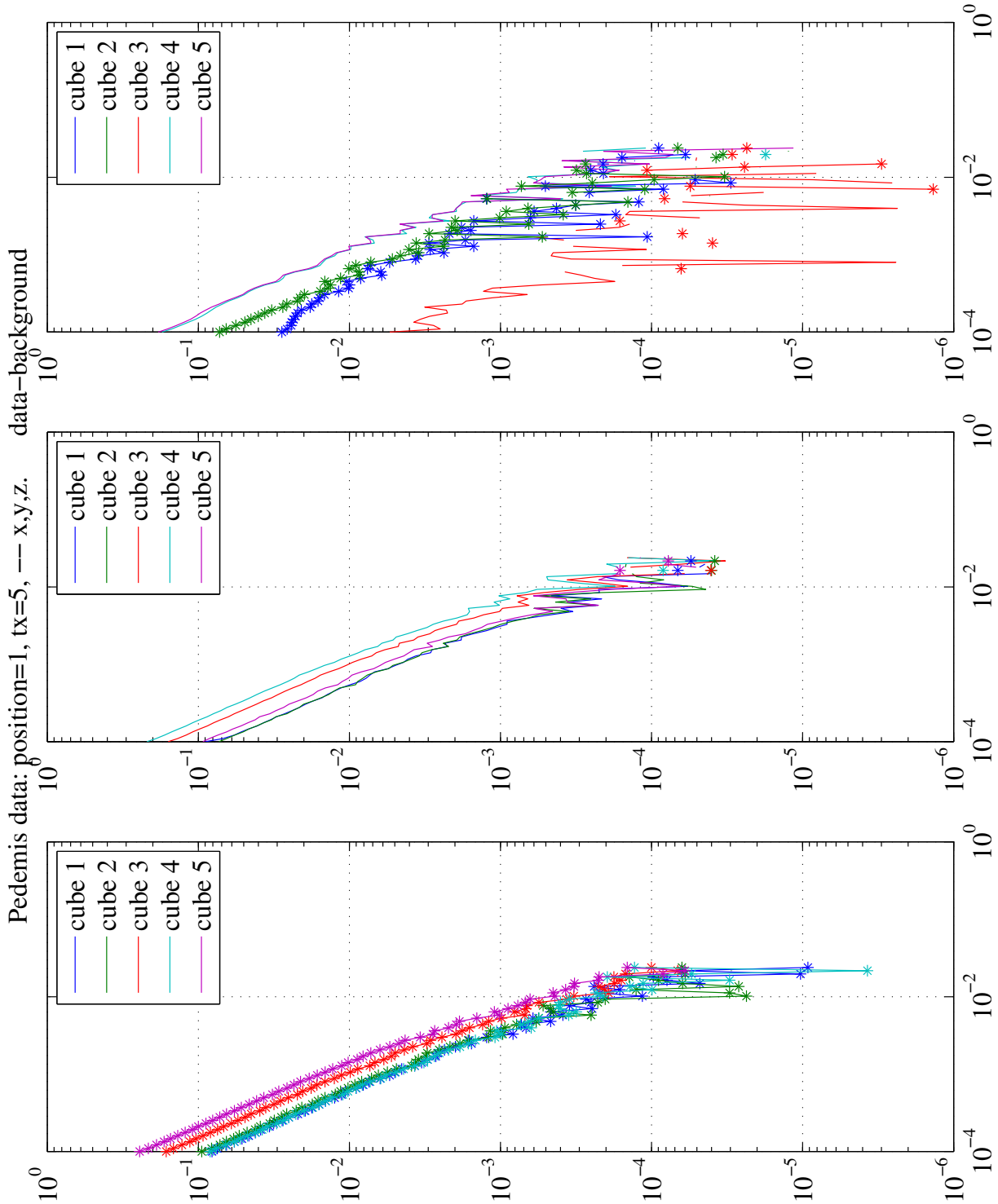

Figure 5.4: Example data from Pedemis. Raw data from the 5 MPV2 receivers situated in the top left corner of the Tx array and the center transmitter firing. The lower subfigure shows the x-component, the center subfigure shows the y-component, and the upper subfigure shows the z-component.

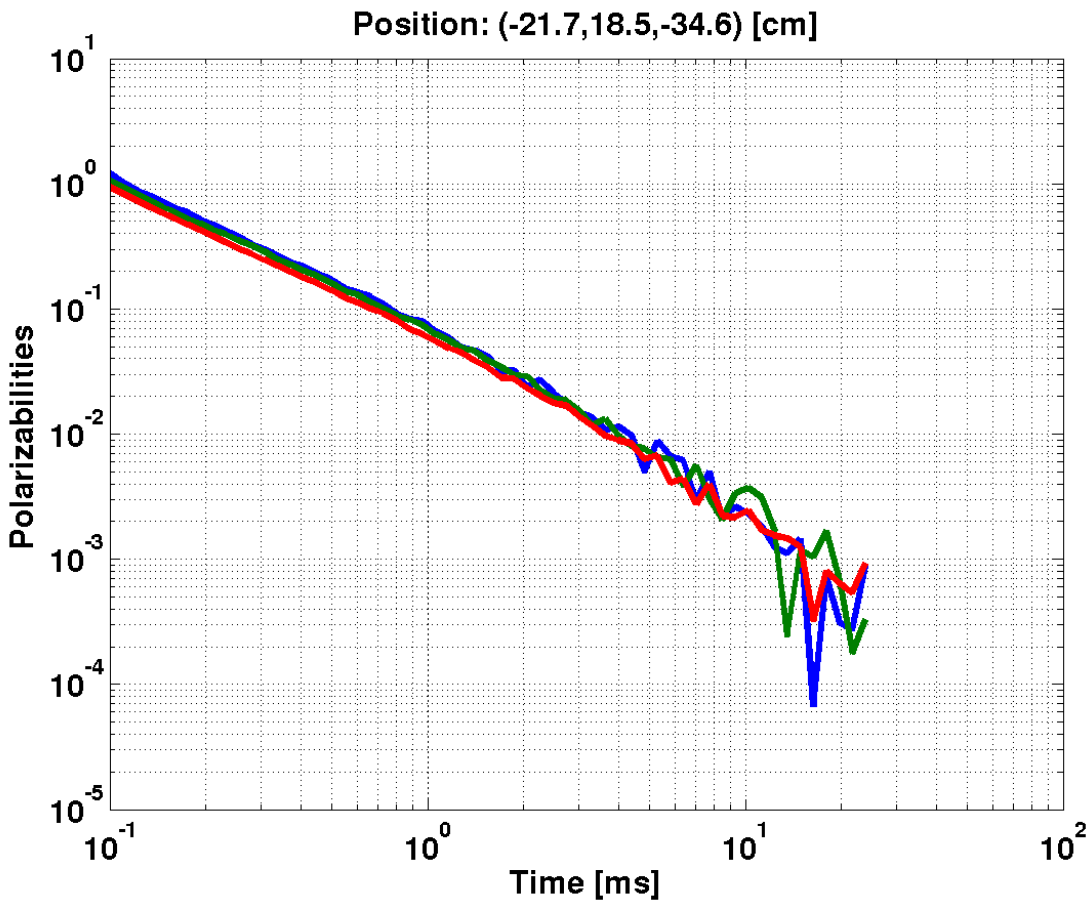

Figure 5.5: Polarizabilities from data in Fig. 5.4. These were calculated using only the x and y components of the received magnetic field due to the z-component being noisy (see discussion above).

5.3 Hardware Challenges

As Pedemis neared completion and deployment in the Fall of 2012, we did some further testing in August, 2012 before deployment to APG. At times, the data acquisition went smoothly and the results looked good, for example in the case depicted in Figs. 5.6–5.8.

Figure 5.6: Pedemis acquiring data over 81mm mortar.

However, we soon noticed that there were times when the ontime data especially did not look so good as shown in Fig. 5.9. We traced this back to a DC to DC converter that was not producing as clean a current as we had hoped (see Fig. 5.10). Once we removed the converter, the currents were predictable and repeatable like in Fig. 5.11 and the ontime data was corrected.

Another challenge we faced was the presence of unwanted residuals in the background of the instrument as shown in Fig. 5.12. The residuals turned out to be a combinations of wire splice connectors (such as those used in automobiles) and wires being very near the top of the Tx array. After removing the splice connectors, the residuals were small and predictable enough for initial deployment, then we could safely ignore them via the usual process of background subtraction for the standard positions of Fig. 4.29.

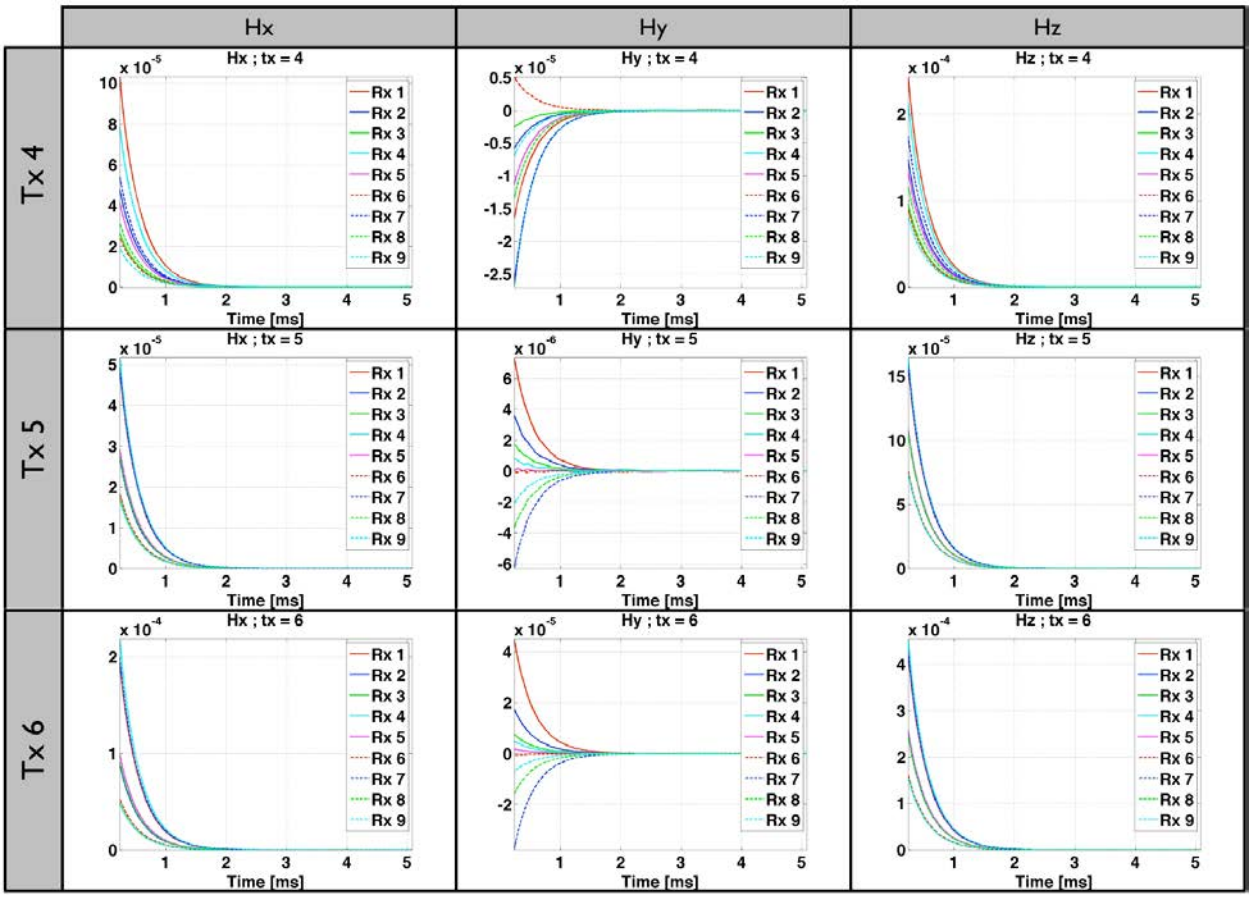

Figure 5.7: Example of "on" time data from August 14th in Grand Junction, CO. These data are clean in this case and are used in positioning the Rx array relative to the Tx array.

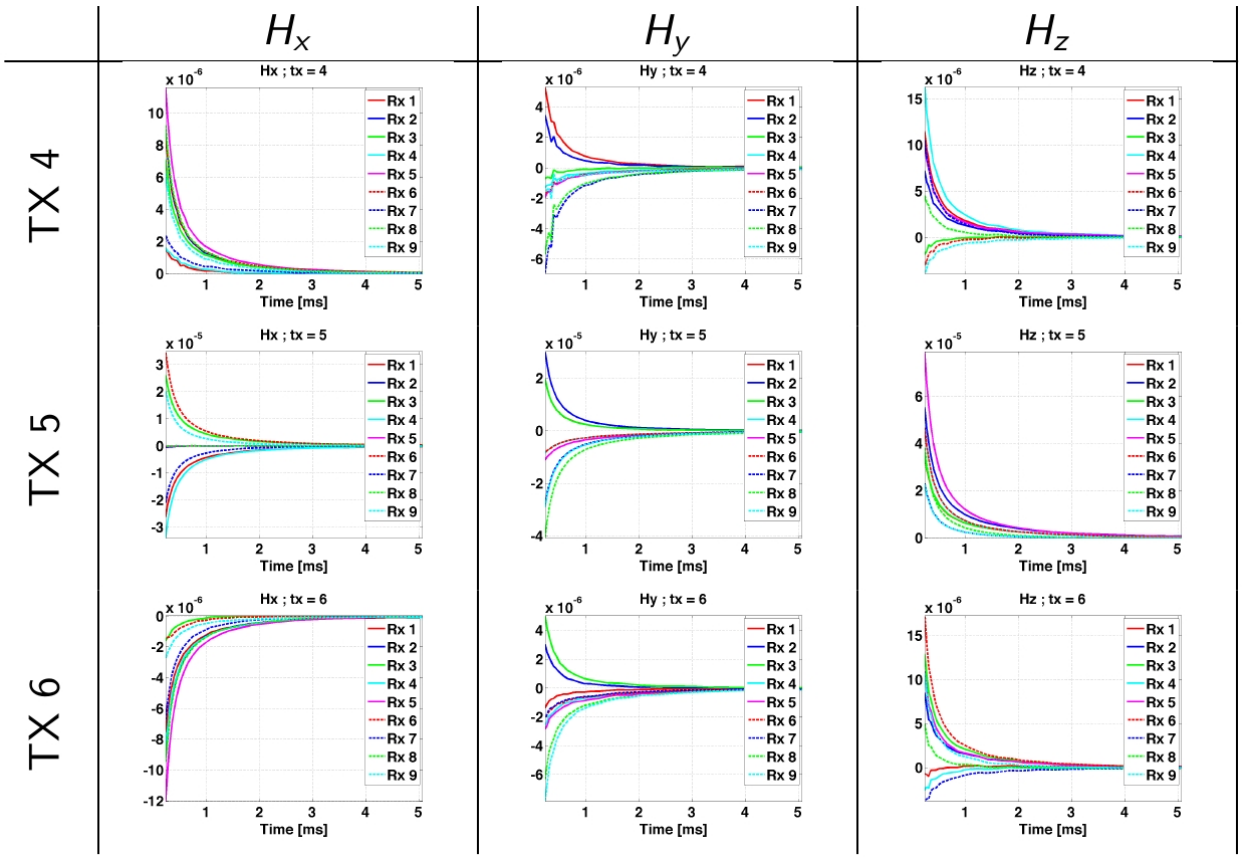

Figure 5.8: Example of "off" time data from August 14th in Grand Junction, CO. These data are used to invert for the target: in this case the 81mm mortar depicted in Fig. 5.6.

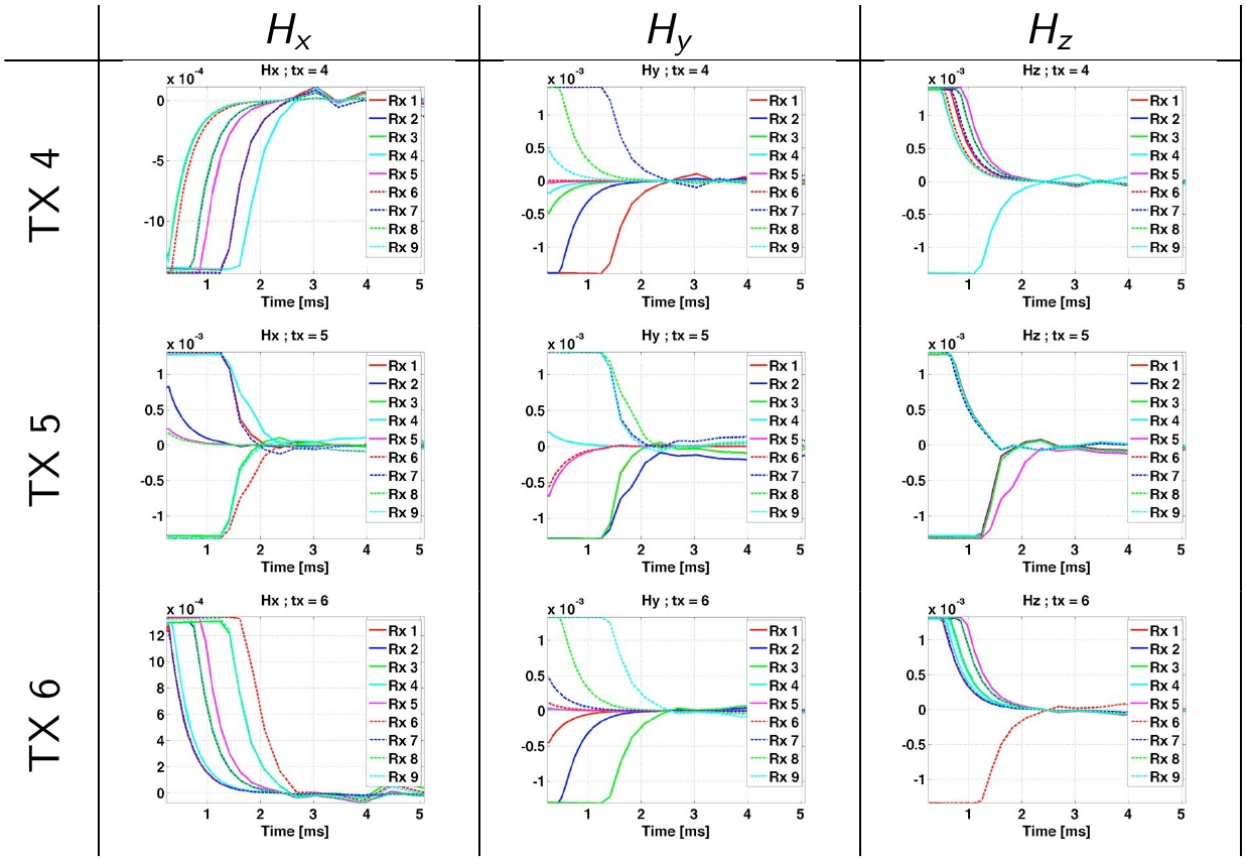

Figure 5.9: Example of “on” time bad data also over a 81mm mortar.

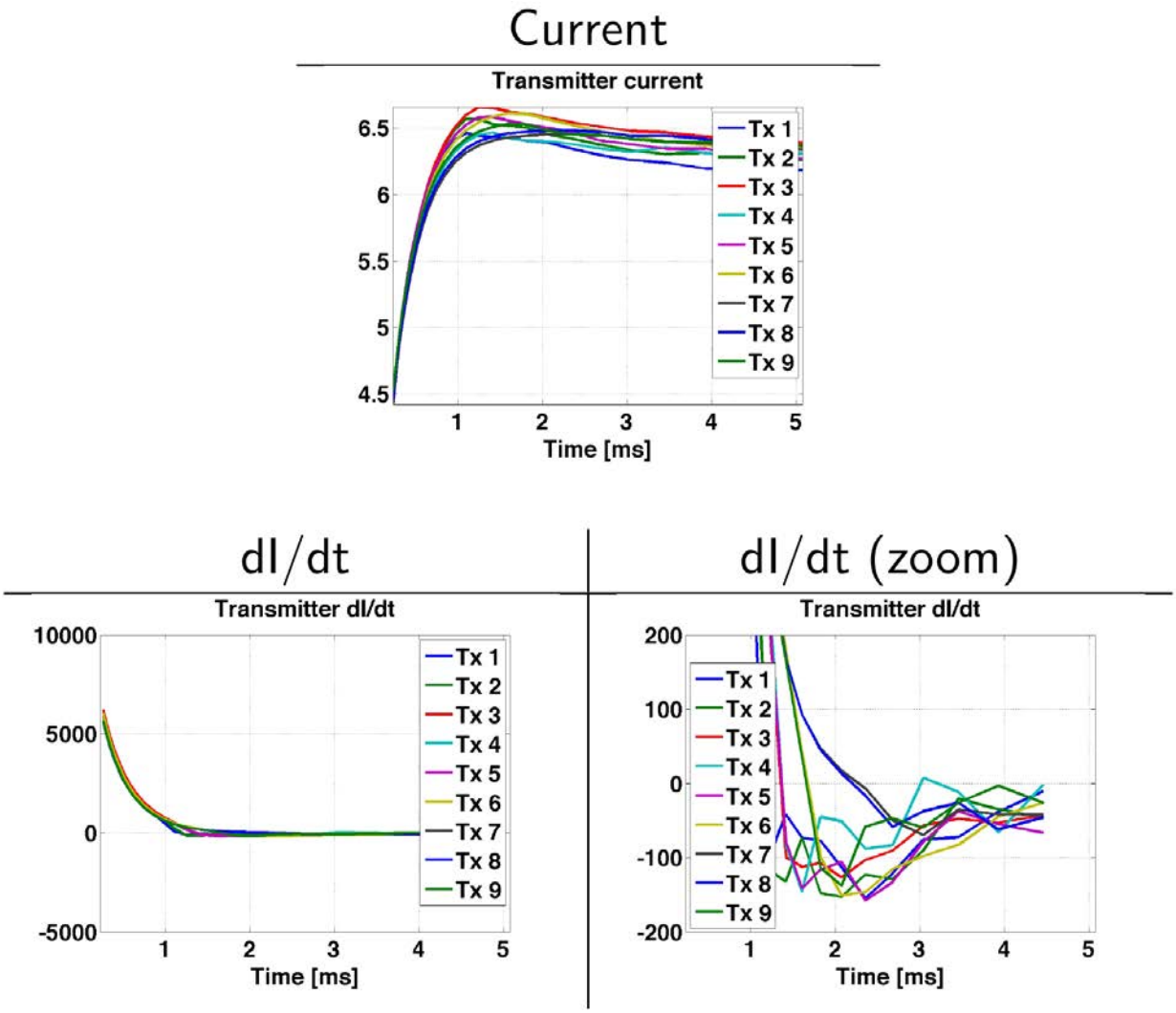

Figure 5.10: Example of unstable Tx currents caused by a DC to DC converter meant to normalize all the currents to the same value.

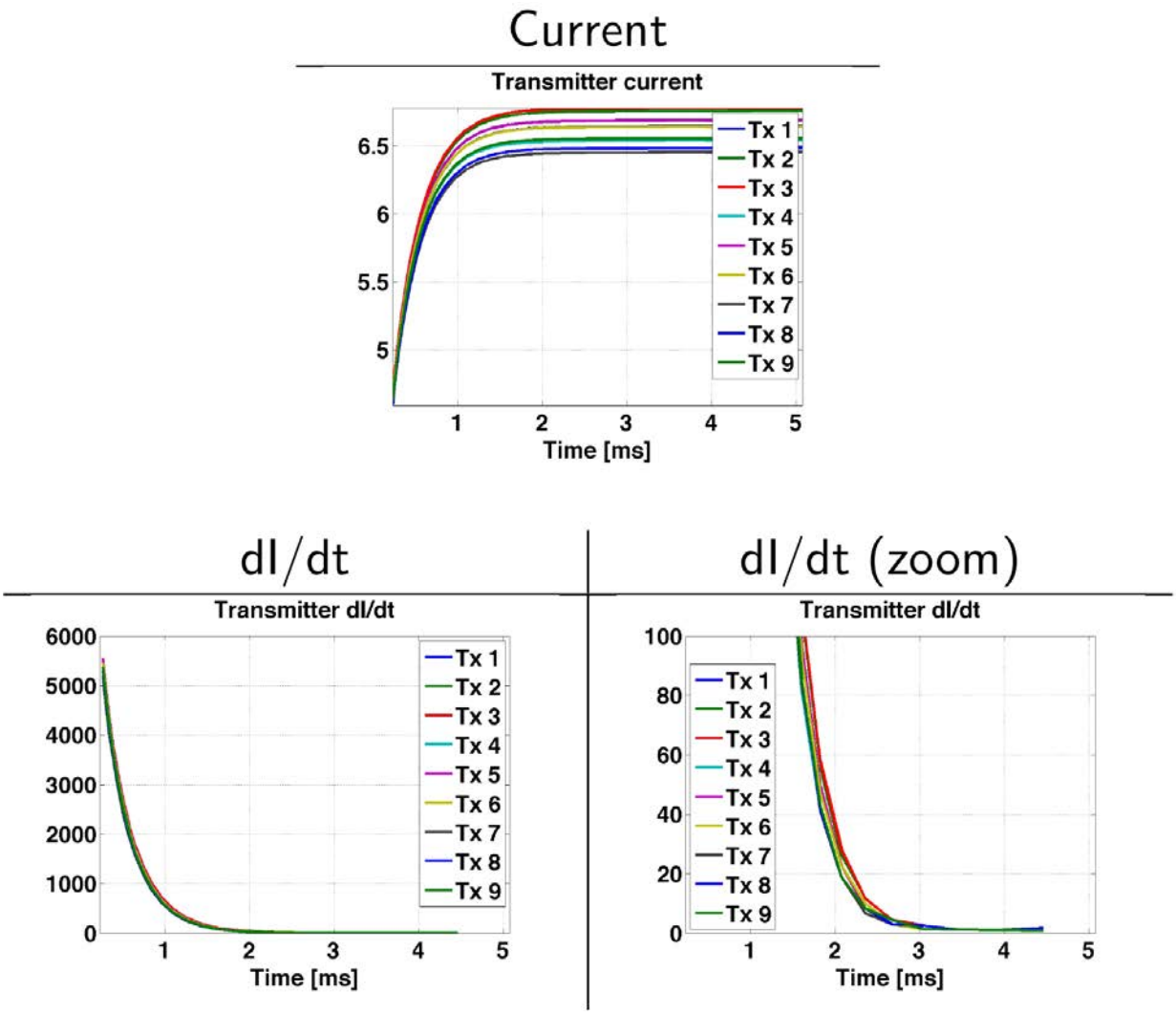

Figure 5.11: Example of stable Tx currents after the DC to DC converter was removed.

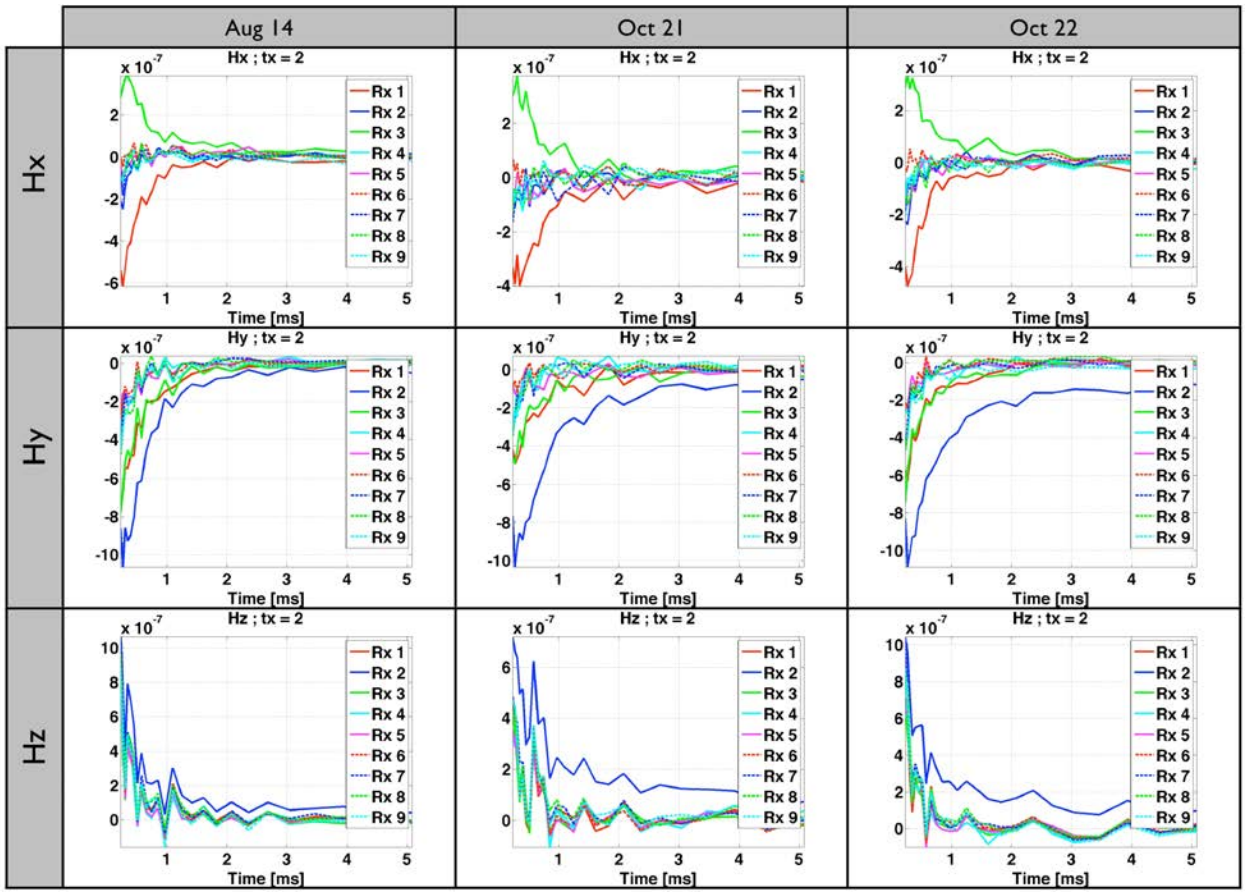

Figure 5.12: Example of unwanted background residuals in Pedemis data.

5.4 APG Deployment

The Pedemis sensor was newly assembled and shipped to APG for its first test site validation, i.e. on actual buried targets as opposed to laboratory testing. The objective of this demonstration is to validate the technology through a blind test at one of the Standardized UXO Test Sites. We have previously done a shake-down demonstration of the technology at G&G Sciences laboratory site (see Sec. 5.2) but a blind test is a better measure measure of system performance.

Figure 5.13: Pedemis at the mogul area at APG.

5.4.a Data Protocol and Acquisition at APG

Here we add some specifics on the data acquisition protocols outlined in Sec. 4.5.

Dynamic data acquisition mode was used in our partial survey of the indirect fire and mogul areas. We stacked 3 10Hz samples then updated the control soft-

ware in real time with the $\hat{z}$ field plots from the nine Pedemis receivers. For this mode, we set up 0.5meter wide lanes in a roughly 40x70 ft quadrilateral (see Fig. 5.33). Two people would carry Pedemis down each lane with one of the operators also looking at a display running Windows Remote Desktop on the mini-PC on Pedemis (see Fig. 4.10). That operator would be looking mostly at the $\hat{z}$ field plots from the nine receivers to make a determination of whether to stop and interrogate a target or not. Once a determination was made to stop, the operator would center Pedemis over the anomaly using a real time arrow system (see Fig. 5.14), and also then choose to get a JD plot (such as in Fig. 5.15) to further determine whether to perform a full interrogation.

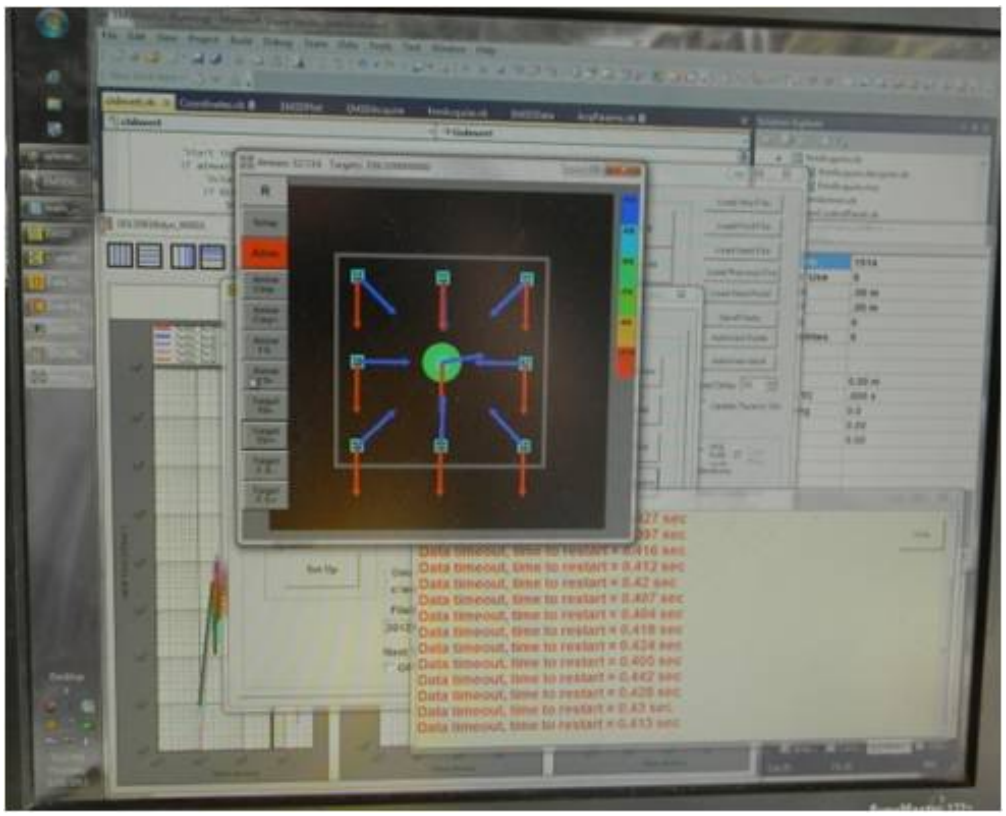

Figure 5.14: Real-time arrow display from EM3D used to center Pedemis over an anomaly during dynamic data acquisition.

Cued interrogation mode #1 (CIM1) followed dynamic mode in the case of further investigation and was also used for all the locations in the calibration and blind grids. CIM1 acquired 360 stacked responses at 10Hz which took 36 seconds total. The Rx array is left in the center of the Tx array at position #1. There were a few cases in the IDF and mogul areas where the signal in dynamic mode was so strong that we skipped CIM1 (see Fig. 5.33). However, we usually performed

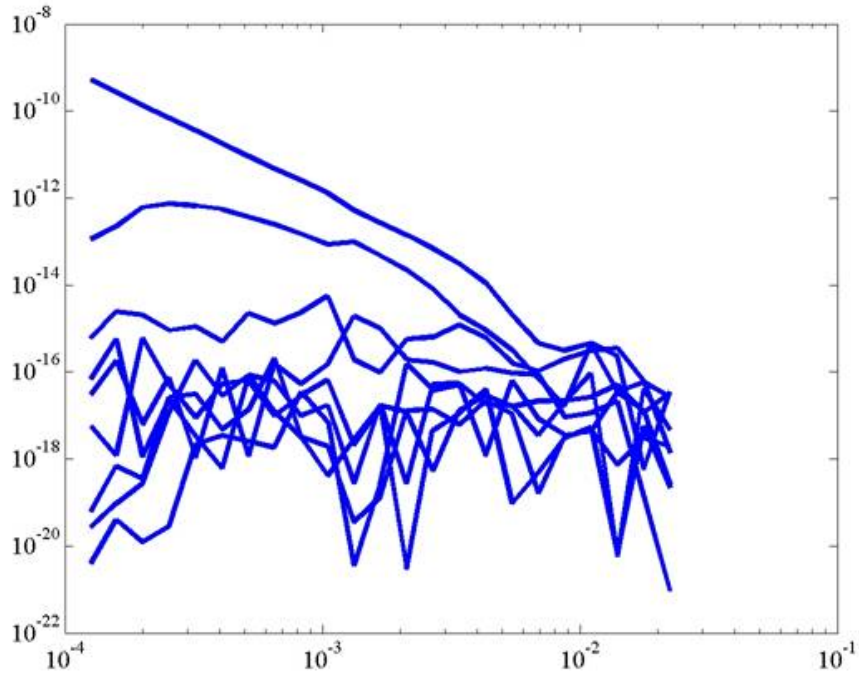

Figure 5.15: JD of Pedemis dynamic data from the indirect fire area at APG.

CIM1 because for the diagnostic value and because we could easily combine the data from CIM1 and CIM2 into a 5-transmitter data set during post processing.

For deep targets, we left the Rx array in position #1, and acquired data for 36 seconds while each of transmitters 2, 4, 6, and 8 were active. This CIM2 data sequence took 144 seconds without any action by the operators to move the Rx array. The purpose of this mode was to interrogate deep targets from a few angles while maximizing data stacking time, thus maximizing SNR. An example of us acquiring data in CIM2 is shown in Fig. 5.16.

CIM3 followed CIM1 if the data were sufficiently strong to not need the longer integration time of CIM2. This mode was useful for getting a better interrogation from shallow targets or multiple targets because of the multiple receiver positions. In this mode, all 9 transmitters would fire in sequence for 3 seconds each while the receiver array was moved through positions 1 to 5. Thus this mode required 5 position changes in between data acquisition and took $9 \times 5 \times 3 = 135$ seconds. Pedemis is shown in CIM3, position 1 in Fig. 5.17 and in position 4 in Fig. 5.18. Due to the shorter stacking time, the SNR of CIM3 is about 12dB lower than the SNR for CIM1 and CIM2.

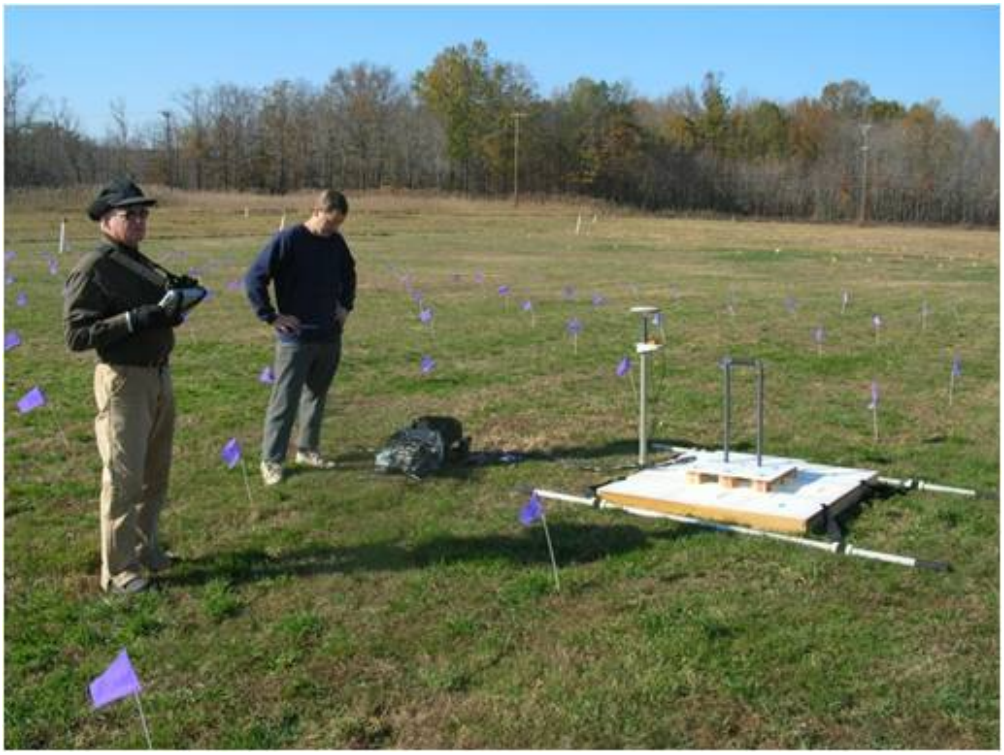

Figure 5.16: CIM2 (deep interrogation mode) data acquisition on the blind grid at APG.

Figure 5.17: Pedemis in CIM3, position 1 for 27 seconds. APG mogul area.

Figure 5.18: Pedemis in CIM3, position 4 for 27 seconds. APG calibration area.

5.4.b APG Background and Site Description

On the advice of SERDP/ESTCP, the site chosen for this test was the UXO Technology Standardized Test Site at Aberdeen Proving Ground. It is located within a secured range area of the Aberdeen Proving Ground. The Aberdeen Area of APG is located approximately 30 miles northeast of Baltimore at the northern end of the Chesapeake Bay. The Standardized Test Site itself encompasses 17 acres of upland and lowland flats, woods and wetlands. It contains calibration lanes with known targets at known locations as well as unknown targets over the blind grid (indicated locations), mogul areas, open fields, and wooded terrain.

More information on the site, its characteristics and the process of its development can be found at http://aec.army.mil/usaec/technology/uxo01c01.html.

5.4.b.(1) Site Selection This is our first field demonstration of Pedemis. The demonstration was conducted on the Standardized UXO Test Site at APG. Use of this site allowed us to receive validation results from near-real-world conditions without incurring the logistics and intrusive investigation expenses that would be required for a demonstration at a live site.

5.4.b.(2) Site History The Standardized UXO Technology Demonstration Site is adjacent to the Trench Warfare facility at the Aberdeen Proving Ground. The specific area was used for a variety of ordnance tests over the years. Initial magnetometer and EMI surveys conducted by the MTADS team performed after a "mag and flag" survey of the same area identified over a thousand remaining anomalies. These data were used for a final clean up of the site prior to the emplacement of the original test items. Prior to the two subsequent reconfiguration events, unexplained anomalies identified by demonstrators using the site were also investigated and removed.

5.4.b.(3) Site Topography and Geology According to the soils survey conducted for the entire area of APG in 1998, the test site consists primarily of Elkton Series type soil[53]. The Elkton Series consist of very deep, slowly permeable, poorly drained soils. These soils formed in silty aeolian sediments and the underlying loamy alluvial and marine sediments. They are on upland and lowland flats and in depressions of the Mid-Atlantic Coastal Plain. Slopes range from 0 to 2 percent.

Overall, the demonstration site is relatively flat and level. There are some low-lying areas in the northwest portion of the site that tend to have standing water during the wet periods of the year. The current sensor system is not sufficiently weatherproofed to operate through standing water. However, during the most recent reconfiguration, the areas most prone to being underwater were excluded from the survey scenarios.

5.4.b.(4) Munitions Contamination Pedemis was deployed in man-portable mode in the calibration and blind test grids. The demonstration then proceeded to parts of the indirect fire and parts of the mogul area (see Table 1). Figure 5.19 is a map of the Standardized UXO Technology Demonstration Site at APG. The Calibration and Blind Grids are shown along with the various Open Field Areas.

Table 1: Layout descriptions at APG as of August 2012.

Test Area	Description
Calibration Lane (0.30 acres)	The calibration portion of the test site consists of at least nineteen (19) lanes. This area contains 14 standard munitions items buried in six positions, with representation of clutter, at various angles and depths to allow demonstrators to calibrate their equipment. A wire hoop gives a standard signature to compare to the signature the detection instrument is receiving. If an installation has site-specific munitions that are not part of the Standardized Target, extra calibration lanes can be added.
Blind Test Grid 0.50 acres	The APG Blind Test Grid (BTG) consists of 400 grid cells. The center of each blind grid cell contains either munitions, clutter, or nothing
Open Field 10.00 acres	The Open Field area provides the demonstrator with a variety of realistic scenarios essential for evaluating sensor system performance. The scenarios and challenges found on this Open Field area consist of a gravel road, wet areas, dips, ruts and trees. Vegetation height varies from 15 to 25 centimeters. Other challenges that may be found on an open field site include electrical lines, swales, stone pads/roads, and metallic fencing that test the capabilities of the platform systems or hand held detectors. Recently the Open Field area was reconfigured to emulate typical impact area conditions. The Open Field area is now divided into four subareas (legacy, direct fire, indirect fire and challenge): Open field (legacy) – The legacy subarea contains the same wide variety of randomly-placed munitions that were present in the open field prior to the January 2008 general reconfiguration of the site. Open field (direct fire) – The direct fire subarea contains only three munition types that could be typically found at an impact area of a direct fire weapons range. Munitions and clutter are placed in a pattern typical for these munitions. Open field (indirect fire) – The indirect fire subarea contains only three munition types that could be typically found at an impact area of an indirect fire weapons range. Munitions and clutter are placed in a pattern typical for these munitions. Open field (challenge) – The challenge subarea is easily reconfigurable used to meet the specific needs and requirements of the demonstrator or the program sponsor. Any results from this area will not be reported in the standardized scoring record.
Scenario 1. Moguls 1.30 acres	Mogul Area – The Mogul Area consists of two areas (the rectangular or driving portion of the course and the triangular section with more difficult, non-drivable terrain). The rectangular section includes six (6) test lanes, which incorporate a slope challenge, 0.61m and 0.91m moguls, 0.61m and 0.91m slanted moguls, and vibration lanes. This section of the course is designed for testing vendors' vehicles' abilities to traverse adverse terrain (vehicle must minimize damage to terrain) and to check accuracy of sensor equipment when subjected to vibration and offset angles created by rough terrain. The triangular section incorporates more intense moguls and terrain, which can be traversed only by foot using hand held or pushed sensor devices. A series of craters (as deep as 0.91m) and mounds (as high as 0.91m) encompasses this section. As rainwater fills the craters, the water serves as another challenge to the demonstrators.
Scenario 2. Wooded Area 1.34 acres	Wooded Area (for APG only) – This area consists of cleared woods (tree removal with only stumps remaining), partially cleared woods (including all underbrush and fallen trees), and virgin woods (i.e., woods in natural state with all trees, underbrush, and fallen trees left in place).

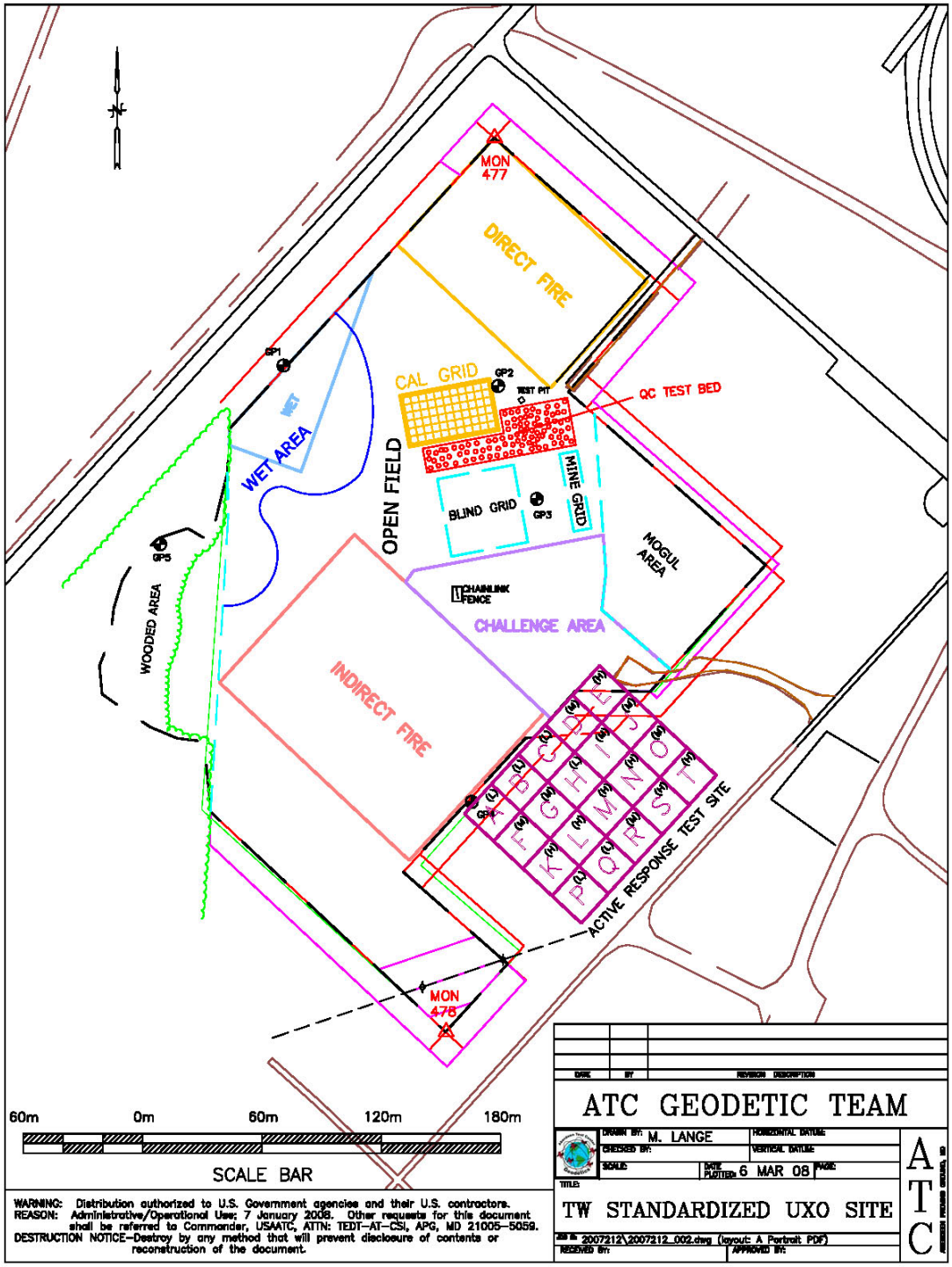

Figure 5.19: Map of the reconfigured (January, 2008) APG Standardized UXO Test Site.

5.4.c APG Objectives

The overarching goal of this test is to validate the Pedemis technology for UXO characterization at sites where topography and vegetation may or may not preclude deployment of wheel-based advanced geophysical platforms. UXO characterization technologies can be affected by variations in site terrain, geology, vegetative cover and weather conditions encountered. It is the objective of our tests to validate the Pedemis technology at a site where each of these factors may play a role; and where the characteristics of the site and the subsurface target configurations are carefully cataloged. This permitted meaningful scoring and comparison of results as well as documentation of realistic costs. The site chosen that fits this description is the Standardized UXO Technology Demonstration Site at Aberdeen Proving Ground (APG).

This Standardized UXO Technology Demonstration Sites Program is a multi-agency program spearheaded by the U.S. Army Environmental Command (USAEC). The U.S. Army Aberdeen Test Center (ATC) and the U.S. Army Corps of Engineers Engineer Research and Development Center (ERDC) provide programmatic support. The program is being funded and supported by the Environmental Security Technology Certification Program (ESTCP), the Strategic Environmental Research and Development Program (SERDP), and the Army Environmental Quality Technology (EQT) program.

The specific characteristics of interest at the APG Standardized Test Site include well characterized targets and settings within calibration lanes; blind grids of targets in which locations are indicated but buried objects are unknown (cued-interrogation); mogul areas with mobility and topography challenges; and open field areas in which unknown targets are at unknown locations, within a considerable variety of representative settings and scenarios. We attempted to demonstrate the Pedemis technology by surveying the test site as if it were a true live site remediation project. Complete characterization of the UXO contamination was demonstrated by collecting the data required to detect potential targets and to classify these targets as part of a single survey.

Effective data collection was assisted by real-time quality control tools, such as signal monitoring, the Joint Diagonalization (JD) method[3], and data quality feedback (see Sec. 5.4.a). Data was processed to supply a prioritized list of targets to excavate. The dig list was based on the inversion of Pedemis data and classification of the recovered parameters, exploiting our recently developed

methods. These include prominently parameterization via the Normalized Surface Magnetic Source (NSMS) model [7–15]; the Orthonormalized Volume Magnetic Source Method (ONVMS) [5, 6, 54]; Joint Diagonalization (JD) of unprocessed survey data, requiring no search or inversion computations, but helping to indicate the number and nature of unseen targets; and clustering algorithms that have proven quite successful at exploiting the NSMS and other parameterizations[55].

Two levels of positioning are required for the modes of operation envisioned herein:

- Geolocationing, RTK GPS system with error less than 10cm for use while covering ground during surveying for anomaly detection (see Fig. 4.10); and
- Precise local positioning of the Rx array relative to the Tx array, with accuracy 1-2cm. This comes into play during detailed in-depth or cued interrogation, especially if the Rx array is detached and arbitrarily moved outside set guides, once an anomaly is detected and judged worthy of in-depth investigation for discrimination processing. We used a "beacon" type local positioning to determine the location of the Rx array relative to the Tx array (see Sec. 4.3).

Orientation of the Tx array relative to the RTK GPS unit is accomplished via a digital compass, an MTI30 Attitude and Heading Reference System from XSENS.

For this test at APG, navigation in the calibration lanes and in the blind grid is not an issue as anomaly locations are marked. Within the mogul and indirect fire zones we laid out survey lines via cords/ropes, at intervals of 0.5 meters between lines. Precise local position, i.e. of the Rx array relative to the Tx array, was accomplished by the beacon system described in Sec. 4.3.

The performance objectives for this test are summarized in Table 2. Success depends on the intrinsic quality of the Pedemis technology, on the quality of the survey protocol and implementation, and on the data analysis that ensues. Measured performance is a combination of these factors and accounts for the proposed one-pass survey protocol, which consists of covering the site in detection mode and interrupting momentarily the detection with a local cued interrogation survey (advanced characterization of an anomaly) whenever a detection threshold is exceeded. The main objective is to characterize the detection and characterization capability of Pedemis as a function of the targets depth and size. Aggravating factors include presence of secondary targets and magnetic soil.

Table 2: Planned schedule of activities for the APG Pedemis test, Summer-Fall 2012

Performance Objective	**Metric**	**Data Required**	**Success Criteria**
Quantitative Performance Objectives			
Detection of all munitions of interest	Probability of detection (Pd) of seeded items at different depths	– Detection map – List of potential targets – Rate of detection of seeded munitions	Pd >0.95 for all munitions in top 0.30 m and for medium and large munitions in top 1 m
Minimize UXO discrimination false alarm rate (DFAR)	Percent anomaly sources identified as UXO that were not	– Prioritized dig list with probabilities – Scoring report from APG	Reduction of false alarms by >75%while maintaining a Pd in cued interrogation of >0.98
Location accuracy	Average error and standard deviation in northing and easting for seed items	– Location of seed items surveyed to accuracy of 5 cm – Estimated location from analysis of data	ΔN and ΔE <7.5 cm σN and σE <7.5 cm
Production rate/coverage	– Number of targets interrogated each day	– Log of field work	– 75 to 100 targets or 0.5 acres per day
Analysis Time	– Average time required for inversion and classification	– Log of analysis work	– Analyst time <2 minutes – Inversion time <15 minutes
Correct Instrument Operation	Data repeatability and verification	Data acquired over same targets at the beginning of each operating day	Data must be repeatable within %1
Survey coverage	Area covered in dynamic mode survey	RTK-GPS location record and compass data	>99.5% coverage (defined as area within 15cm of 50cm Rx array)
Qualitative Performance Objectives			
Ease of use in field procedures and in data analysis		– Feedback from field personnel on usability of technology and time required – Feedback from data analysts on usability of data and time required	

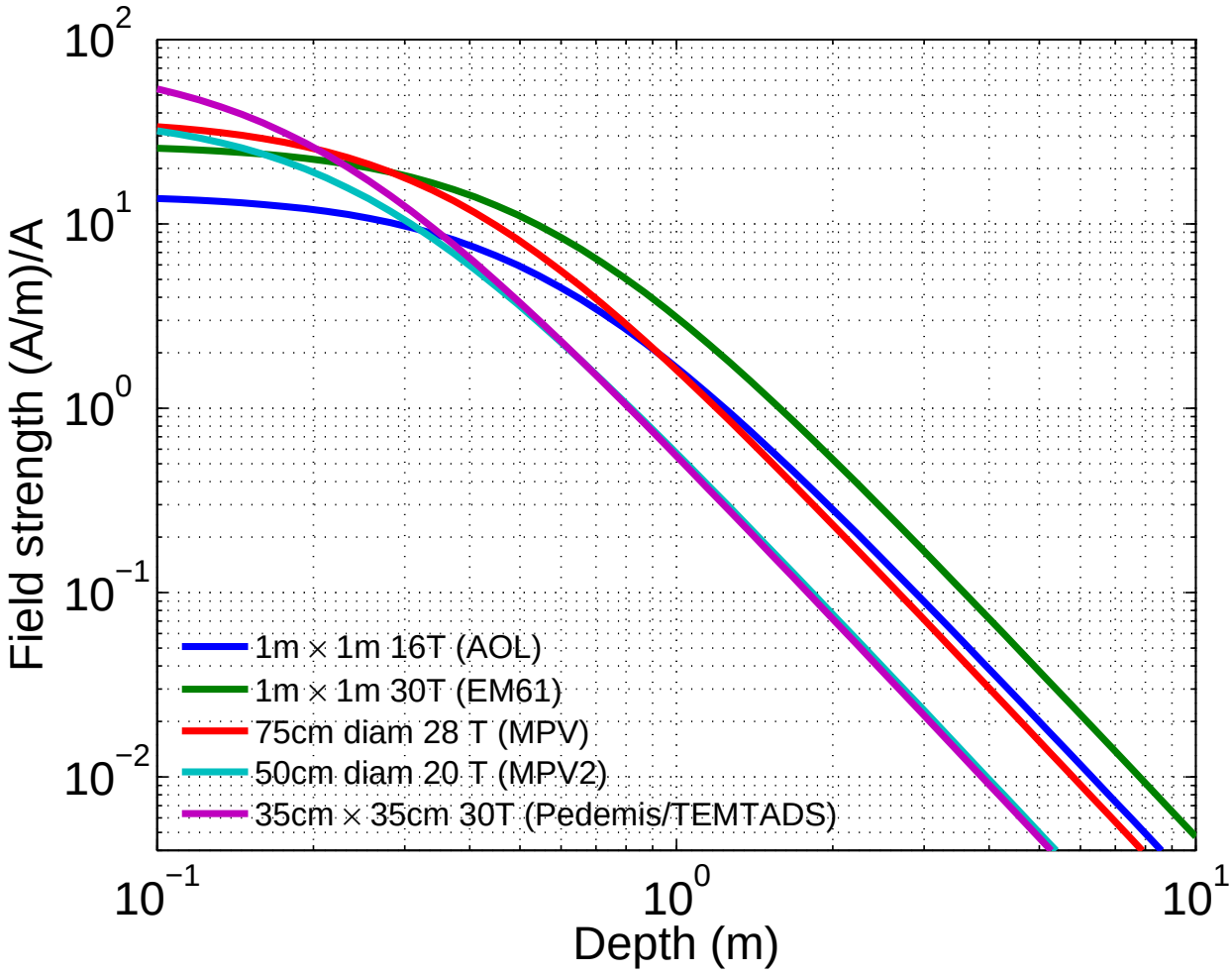

Figure 5.20: The vertical field strength of 6 different systems studied, measured as a function of depth beneath the center of the loops.

5.4.c.(1) Objective: Detection of all munitions of interest This is the primary objective of this demonstration. All shallow potential targets should be detected and recognized as such. Even though Pedemis is a man-portable EMI sensor, our modeling during the initial stages of this project and the MR1443 (MPV) project suggested that even though the transmitters of Pedemis are smaller than MetalMapper, for example, the primary field at depths of interest is not significantly different (see Fig. 5.20). In fact, the transmitters of Pedemis are the same size as the transmitters of TEMTADS, a system that has demonstrated good depth perception in field trials. We expect Pedemis to have the similar detection performance as these other handheld and wheel based systems.

5.4.c.(2) Objective: Reduction of False Alarms This is the other primary measure of the effectiveness of this technology. By collecting high-quality, precisely-located data, we expect to be able to discriminate munitions from scrap and frag with high efficiency.

5.4.c.(3) Objective: Location Accuracy An important measure of how efficiently any required remediation will proceed is the accuracy of predicted location of the targets marked to be dug. Large location errors lead to confusion among the UXO techs assigned to the remediation costing time and often leading to removal of a small, shallow object when a larger, deeper object was the intended target.

5.4.c.(4) Objective: Production Rate Even if the performance of the technology on the two metrics above is satisfactory, there is an economic metric to consider. There is a known cost of remediating a suspected munitions item. If the cost to interrogate a target is greater than this cost, the technology will be useful only at sites with special conditions or target values. Note, however, that in its ultimate implementation this technology will result in detection and classification on a single survey. The limiting factor of

- The number of targets interrogated per day or
- The acreage surveyed per day

is the metric for this objective. Combined with the daily operating cost of the technology this gives the per-item cost.

5.4.c.(5) Objective: Analysis Time The ultimate implementation of this technology will involve on-the-fly analysis and classification. The time for this type of implementation will be limited to the time spent reviewing the data acquired from an anomaly, and possibly the time taken as the survey is continued and the next anomaly is found. The inversion routines currently in use for Pedemis are currently not efficient enough to allow this type of real time analysis and classification. However, we are trying to work toward this goal.

In this demonstration, we will spent a few seconds per anomaly to make a real time decision after cued interrogation mode #1 according to the decision process outlined in Sec. 4.5. This real time decision will be based on the field values and from the JD analysis from the initial, centered data shot.

Nevertheless, we will track the post survey inversion and analysis time for this demonstration.

5.4.d Data Analysis plan

5.4.d.(1) Preprocessing The array has nine transmitters/receiver pairs. For each transmit pulse, we record the response at all of the receivers. Hence, for each target we have a 9 x 9 x N data array, where N is the number of recorded time gates. Normally we use 25 logarithmically spaced gates. In preprocessing, the recorded signals are normalized by the transmitter currents to account for any transmitter variations. Measured responses include distortions due to transmitter ringing and related artifacts out to about 0.100 millisec. Consequently we only include response beyond 0.1 ms in our analysis.

Instrument background will be subtracted out from the data response if the Rx array was in one of the standard positions, or via an equivalent source model of the instrument constructed with data acquired in Grand Junction, Co in August, 2012. The geological background response is subtracted from each target measurement using data collected in a nearby target-free region. We will inter-compare all of the background measurements to evaluate background variability and identify outliers which may correspond to measurements over non-ferrous targets.

5.4.d.(2) Target Selection for Detection Target detection will be performed in real time based on Pedemis detection window (JD, dancing arrows, signal amplitude and time decay) as detailed in Sec. 5.4.a. The calibration lanes will be surveyed with an ad hoc detection threshold based on data recently collected in Grand Junction, Colorado. A detection rule for the mogul and indirect fire areas will be defined after evaluation of the calibration lanes, where targets are located and identified.

The measured EMI signal from a target depends on its burial depth and orientation, and the sensor spatial sampling relative to the target's peak signal. Spatial sampling will depend on the sensor update rate (10 Hz), survey speed, and the horizontal offset between the receivers nearest to the peak.

We propose to use the ONVMS to quantify the effect of these parameters under the most and least favorable conditions of depth, orientation and horizontal offsets for all objects of interest. Calibration data will be collected in dynamic (detection) and static (cued interrogation) modes. The maximum EMI signal strength recorded in dynamic and static mode will be compared to define a rule between acquisition modes. The ONVMS will be used to invert the static data and derive intrinsic parameters for each target type. Then the parameters will be combined

with the ONVMS model to predict the measured EMI signal strength in static mode as a function of depth, orientation and horizontal offset for all targets of interest, and finally translated in terms of dynamic signal strength. This analysis will provide the minimum detection signal strength for each target as a function of depth.

5.4.d.(3) Parameter Estimation The preprocessed data will be used to estimate parameters of each of the targets in view of the sensor. The JD algorithm will be used to estimate the number of objects present, N. Then the ONVMS [5, 6, 54] as well as a multiple dipole model [2] will be used to estimate these parameters. Clustering algorithms to help classify ordnance types will also be used [55].

5.4.d.(4) Training For the statistical classification, we will use the data over the calibration lanes to determine the feature vectors and statistical classifier to use. The calibration lanes contain all munitions that can be encountered at the site and some clutter. Munitions are buried at various depths and orientations, thus providing the opportunity to estimate the variance of the feature vectors. Canonical analysis and experience will be used to generate linear and nonlinear combinations of feature vectors to be used in the classification. We will use features derived from polarization tensor parameters (depth, polarizability eigenvalues, polarizability or ONVMS decay rates) as well as features derived from the data (amplitude). Again, clustering based on methods in [55] will be used.

5.4.d.(5) Classification Target classification is based on a library matching procedure by trained analysts. We will use the same method, using the ONVMS model results, as we used in the recent Camp Beale and Camp Butner analyses [5] to analyze the APG data. Results from the analysts will be submitted for scoring.

5.4.d.(6) Data Product Specification The demonstration will be conducted at the APG Standardized Test Site. We used the standard reporting templates for the Blind Grid, the Open Field, and the Mogul area shown below in Figs. 5.21 and 5.22.

BLIND TEST GRID										
	Letter	Number	Response Stage	Discrimination Stage/Ranking	Classification (Use B for Blank)	TYPE	Depth (m)	Azimuth (Degrees)	Dip (Degrees)	Comments
1	A	1								
2	A	2								
3	A	3								
4	A	4								
5	A	5								
6	A	6								
7	A	7								
8	A	8								
...	...	...								

Figure 5.21: Reporting Template for APG Blind Grid.

INDIRECT FIRE										
	Northing	Easting	Response Stage	Discrimination Stage/Ranking	Classification	TYPE	Depth (m)	Azimuth (Degrees)	Dip (Degrees)	Comments
1										
2										
3										
4										
5										
6										
7										
8										
...										

Figure 5.22: Reporting Template for APG Indirect Fire Area.

5.4.e APG Results

We deployed Pedemis to Aberdeen Proving Ground in November, 2012, acquiring data over the following areas:

- calibration grid

- blind grid (400 locations)
- partial of indirect fire area
- partial of mogul area

Pedemis acquired 25 milliseconds worth of data after a 100 microsecond holdoff in 25 logarithmically time gates according the waveform in Fig. 4.30.

5.4.e.(1) Preliminary Dipole Inversion The Pedemis sensor was newly assembled and shipped to APG for its first test site validation, i.e. on actual buried targets as opposed to laboratory testing. Data were analyzed by our Gauss-Newton algorithm which has been extensively validated on several sensors and multiple environments [2]. The algorithm iteratively estimates the position, orientation, and polarizabilities of UXO within the dipole approximation and has been used here to produce the polarizabilities shown in Figure 5.23 of the 105 mm, 81 mm, 60 mm, 37 mm, and 25 mm projectiles. These targets were present in multiple grids, both calibration and blind, and ten polarizability signatures have been selected based on their correlation and amplitude match. It is seen that in all cases, the ten signatures present a clear overlap that allows for an easy identification of these specific targets, demonstrating that the new Pedemis sensor indeed collects high quality data compatible with UXO identification in real condition. For these targets, the ground truth for each cell in the blind grid remains unknown but the consistent and clean polarizabilities of Figure 5.23 indicate a proper inversion by our algorithm. In order to further validate the inverted positions as well as the applicability of the Pedemis to more challenging configurations, we proceed by generating semi-synthetic multi-target data since multi-target cells were not available at APG.

The semi-synthetic datasets are generated by letting the polarizabilities of Figure 5.23 radiate from known locations according to the dipole model [56, 57], and by adding the secondary magnetic fields from as many targets as desired. The cases studied are those of two targets (81 mm and 60 mm), three targets (81 mm, 60 mm, and 25 mm), four targets (81 mm, 60 mm, 25 mm, 37 mm), and five targets (81 mm, 60 mm, 25 mm, 37 mm, 105 mm), with the respective positions listed in Table 3. Our Gauss-Newton algorithm, adapted to multi-target inversion [2], is used to simultaneously invert for all unknowns at once, namely the positions, orientations, and polarizabilities of all targets at once, assuming the number of targets known a priori in each situation. Note that for a more direct applicability

UXO type		81 mm	60 mm	25 mm	37 mm	105 mm
True (x,y,z) [cm]		(30, -30, -35)	(-30, 30, -20)	(-10, 1, -26)	(-40, -40, -30)	(10, 10, -25)
Error [cm]	2 targets	(-0.3, -0.0, -0.1)	(-0.0, -0.0, -0.1)			
	3 targets	(-0.7, 1.2, -0.3)	(0.0, 0.0, 0.0)	(-0.0, 0.0, 0.2)		
	4 targets	(-0.7, -0.3, -0.3)	(-0.0, -0.1, 0.0)	(-0.5, 0.5, -0.2)	(-0.9, -0.5, 0.3)	
	5 targets	(-0.2, 0.0, 0.1)	(0.2, -0.3, 0.7)	(3.1, -0.5, 1.0)	(-0.3, 0.2, 0.2)	(0.0, 0.0, -0.0)

Table 3: Errors in predicted positions for up to five targets simultaneously present under the Pedemis sensor.

to in-field situations, it is possible to assume a large number of dipoles (typically five are used, i.e. assuming that there are no more than five homogeneous targets within the sensor field of view) and let the algorithm either aggregate the dipoles at true target locations or invert some dipoles with negligible polarizabilities. The inverted positions listed in Table 3 show that in all cases, and for up to five simultaneous targets, the algorithm is able to locate the targets with sub-centimeter accuracy (except for an error of about 3 cm on the 25 mm projectile in the five-target configuration). The polarizabilities, not shown here, are all in excellent agreement with the ground truth of Figure 5.23 as expected.

This section reports on the data collection protocol of the newly assembled Pedemis sensor by G&G Sciences Inc. as well as some resulting target identification inversions from data collected at the Aberdeen Proving Ground Standardized UXO Technology Demonstration Site of the United States Army Environmental Command. The results selected for this section all corresponded to relatively strong target signals and hence were processed following protocols (1) and (2b): a first sensing using a single transmitter to judge on the signal quality followed by sensing using all transmitters. The results show that signatures of similar targets are very consistent from cell to cell, allowing for an easy classification. However, not all cells at APG produced clear signatures, some being seeded with frag, clutter, or nothing. For those cases, we followed protocols (1) and (2a): a similar initial sensing using a single transmitter followed by a deep sensing using only several selected transmitters in order to save operating time. The presentation of these results is beyond the scope of this section and the statistical processing of the complete set of inversion results follows (and in [38]).

Finally, we have also shown that the dataset of the Pedemis sensor may be compatible for up to five targets inversions, although such conclusions would have to be corroborated by actual measurement data. Yet, knowing that multi-target

inversion remains possible is an important sensor feature when surveying more challenging sites where several UXO are buried in close proximity to one another or when a UXO is surrounded by clutter items.

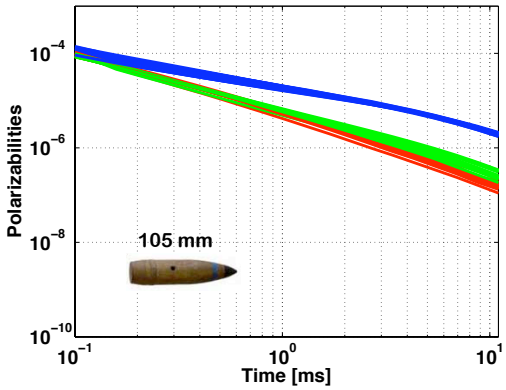

(a) 105 mm projectile.

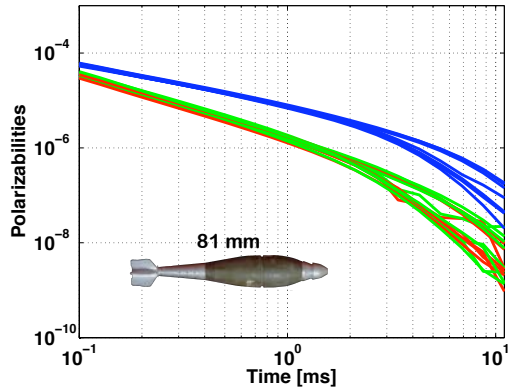

(b) 81 mm projectile.

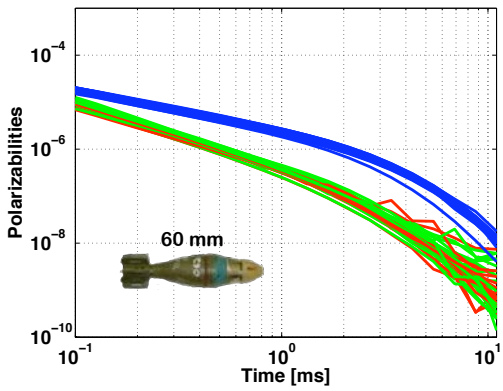

(c) 60 mm projectile.

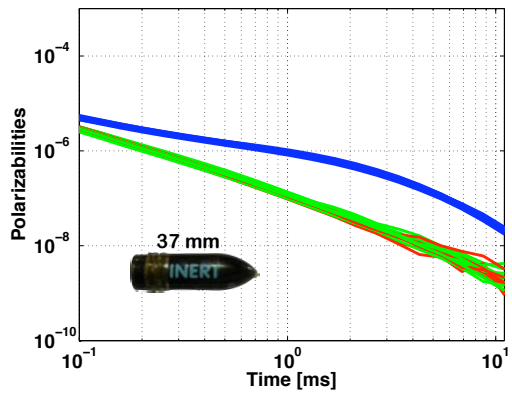

(d) 37 mm projectile.

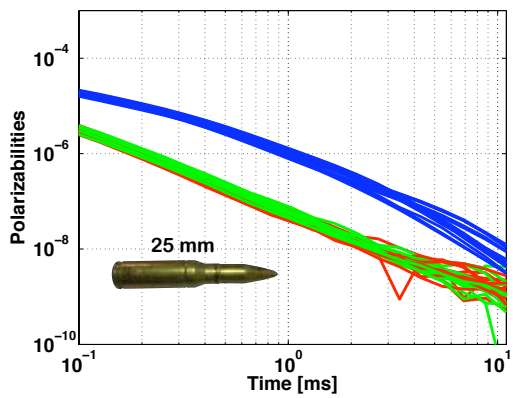

(e) 25 mm projectile.

Figure 5.23: Selection of time dependent polarizabilities of several similar targets from both the calibration and the blind grids. The three curves in each figure represent the diagonalized polarizability tensor with the strongest component (blue) corresponding to the principal axis of the UXO (along their longest physical dimension) and the two similar weakest components corresponding to the secondary axes (of similar magnitudes because of the body of revolution shape of the UXO). All inversions have been obtained with protocols (1) and (2b).

5.4.e.(2) APG Official Scored Results We followed the protocol described in Sec. 5.4.a for acquiring cued data at APG. At each new location for cued interrogation, we would first take an initial CIM1 data shot which lasted for 36 seconds. Based on prior work, we knew that data from a single transmitter is insufficient to resolve all three polarizabilities (or ONVMS equivalent) of a target. However, the real time feedback from CIM1 allowed us to move into a full interrogation via CIM2 or CIM3.

There are three stages of scoring for APG:

- Detection (or response) stage (something there or not)
- Discrimination stage (UXO or clutter)
- Classification Stage (which type of UXO)

Figures 5.24 and 5.25 show the results for the detection stage at the APG blind grid. To summarize, we found all the UXO present (the "1.00" in the top left of the grid), we found all but 3 (shallow small pieces) of the official clutter in the blind grid ("0.98"), and found 29 extra pieces of clutter ("0.14"). Note that all the numbers on the lower half of the grid in Figs. 5.24 and 5.26 should be moved one line upward. For full APG results, see Sec. C.1.

Results from the discrimination stage from the blind grid are shown in Figs. 5.26 and 5.27. As a summary, we found all the UXO in the blind grid with only four false positives (clutter that we called UXO). These scores are the best to date for any instrument at APG.

Results from the classification stage are shown in Figs. 5.28 and 5.29. Note that there is some confusion from official at APG on the type of 105mm ordnance in the blind grid, so these low percentages of 7 and 13% are probably too low. Also note that we forgot to take into account the finite thickness of the Tx array when we reported estimated depths to APG, so the mean and standard deviation in Fig. 5.29 should be smaller by 0.045cm.

Example groups of total ONVMS from different ordnance are shown in Figs. 5.30 and 5.31. There were several cases where we had to use a two target ONVMS inversion in order to correctly discriminate and classify the targets in the blind grid. This could have been due to an unofficial piece of clutter, geological noise, or a complicated ordnance such as the 105mm HEAT round at shallow depth. Slides 22-24 in Appendix D give some examples of these cases.

Response Stage				
Munitions[a] Scores	**Pd^{res}: by type**			
	All Types	**105-mm**	**81/60-mm**	**37/25-mm**
	1.00 1.00 0.98	1.00 1.00 0.93	1.00 1.00 0.93	1.00 1.00 0.93
0 to 4D	1.00	1.00	1.00	1.00
4D to 8D	1.00	1.00	1.00	1.00
8D to 12D	1.00	1.00	1.00	1.00
Clutter Scores	**P_{cd}**			
By Depth[b]	**All Mass**	**0 to 0.25 kg**	**>0.25 to 1 kg**	**>1 to 8 kg**
All Depth	0.99 0.98	0.95	1.00	1.00
0 to 0.15 m	0.95			
0.15 to 0.3 m	0.97	0.94	1.00	1.00
0.3 to 0.6 m	1.00	1.00	1.00	1.00
				Background Alarm Rat
	P_{ba}^{res}: 0.14			

Figure 5.24: APG detection results.

Full results for the IDF and mogul areas are included in Appendix C.1. Though APG reported that there were no UXO in the IDF area we surveyed, the data shots we took there are shown in Figs. 5.32 and 5.33.

Similarly, the dynamic and CIM data we acquired in the mogul area is shown graphically in Fig. 5.34.

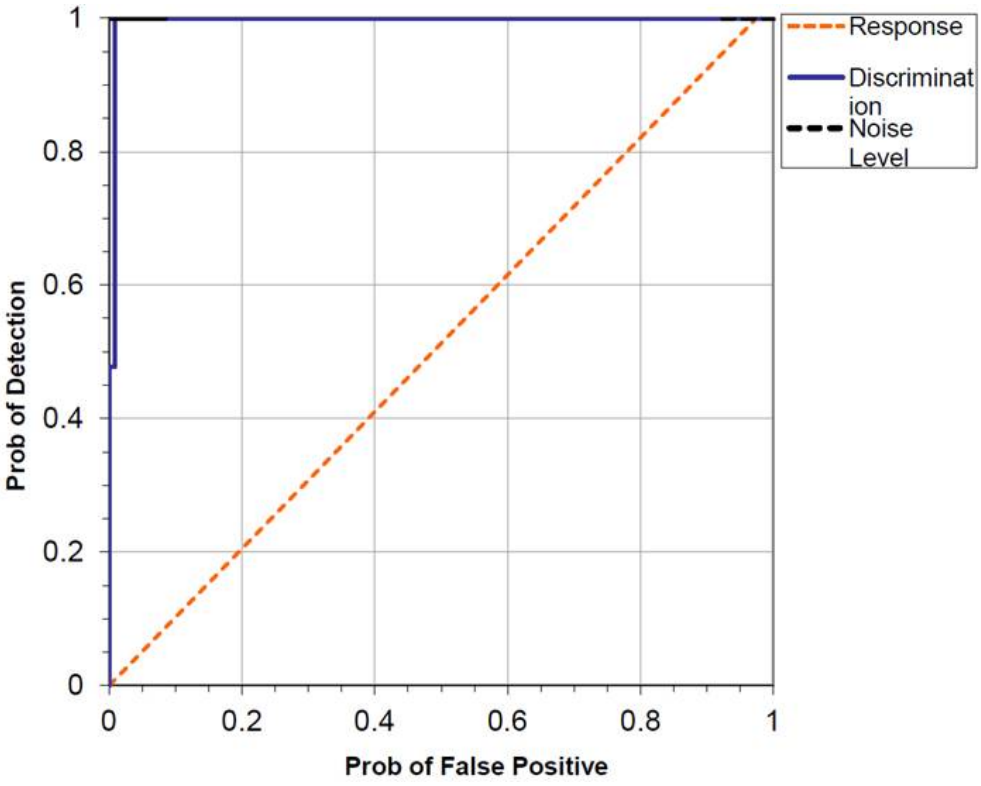

Figure 5.25: APG detection stage results ROC curve.

	Response Stage				Discrimination Stage			
Munitions[a] Scores	**Pd^{res}: by type**				**Pd^{disc}: by type**			
	All Types	**105-mm**	**81/60-mm**	**37/25-mm**	**All Types**	**105-mm**	**81/60-mm**	**37/25-mm**
	1.00 1.00 0.98	1.00 1.00 0.93	1.00 1.00 0.93	1.00 1.00 0.93	1.00 1.00 0.98	1.00 1.00 0.93	1.00 1.00 0.93	1.00 1.00 0.93
0 to 4D	1.00	1.00	1.00	1.00	1.00	1.00	1.00	1.00
4D to 8D	1.00	1.00	1.00	1.00	1.00	1.00	1.00	1.00
8D to 12D	1.00	1.00	1.00	1.00	1.00	1.00	1.00	1.00
Clutter Scores	**P_{cd}**				**P_{fp}**			
By Depth[b]	**All Mass**	**0 to 0.25 kg**	**>0.25 to 1 kg**	**>1 to 8 kg**	**All Mass**	**0 to 0.25 kg**	**>0.25 to 1 kg**	**>1 to 8 kg**
All Depth	0.99 0.98	0.95	1.00	1.00	0.07 0.03	0.00	0.04	0.20
0 to 0.15 m	0.95				0.02			
0.15 to 0.3 m	0.97	0.94	1.00	1.00	0.02	0.00	0.02	0.17
0.3 to 0.6 m	1.00	1.00	1.00	1.00	0.13	0.00	0.14	0.25
Background Alarm Rates								
	P_{ba}^{res}: 0.14				**P_{ba}^{disc}:** 0.00			

Figure 5.26: Results for the blind grid for Pedemis at APG in November, 2012. Note that results numbers in the lower half of the table are one line too low.

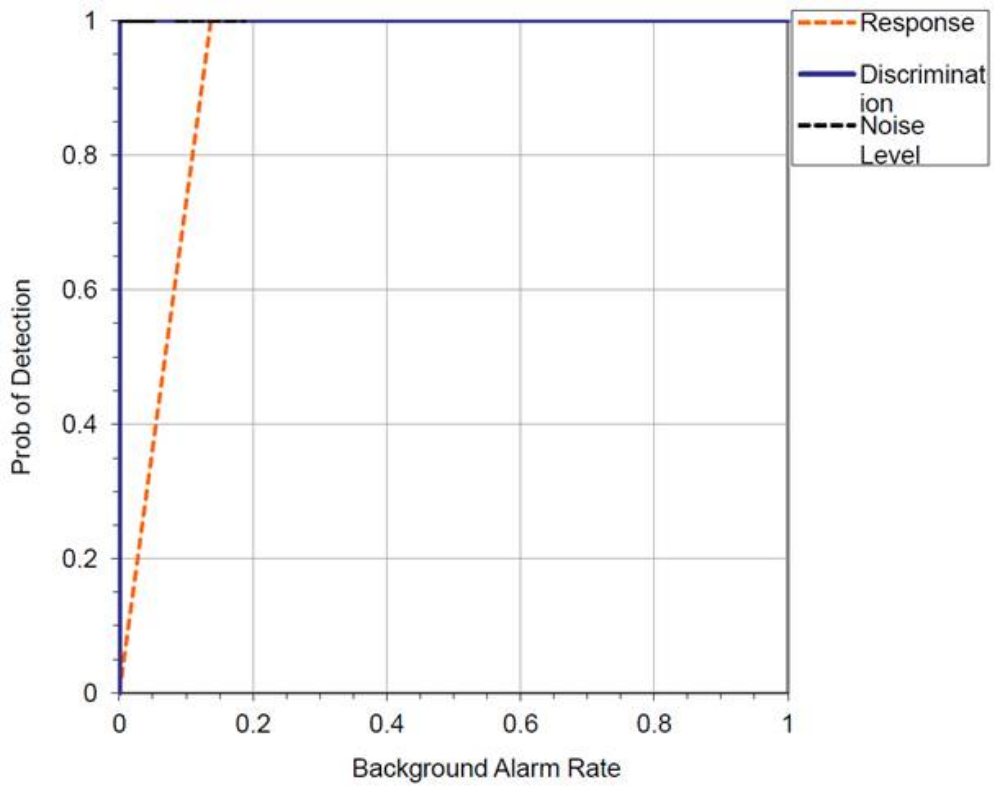

Figure 5.27: APG discrimination stage results ROC curve.

TABLE 8a. BLIND GRID CORRECT TYPE CLASSIFICATION OF TARGETS CORRECTLY DISCRIMINATED AS MUNITIONS

Size	Percentage Correct
25mm	100%
37mm	100%
60mm	100%
81mm	80%
105mm	7%
105 artillery	13%
Overall	67%

Figure 5.28: APG classification results by ordnance type.

TABLE 9a. BLIND GRID MEAN LOCATION ERROR AND STANDARD DEVIATION

	Mean	Standard Deviation
Northing	N/A	N/A
Easting	N/A	N/A
Depth	0.072	0.063

Figure 5.29: APG location error, mean and standard deviation.

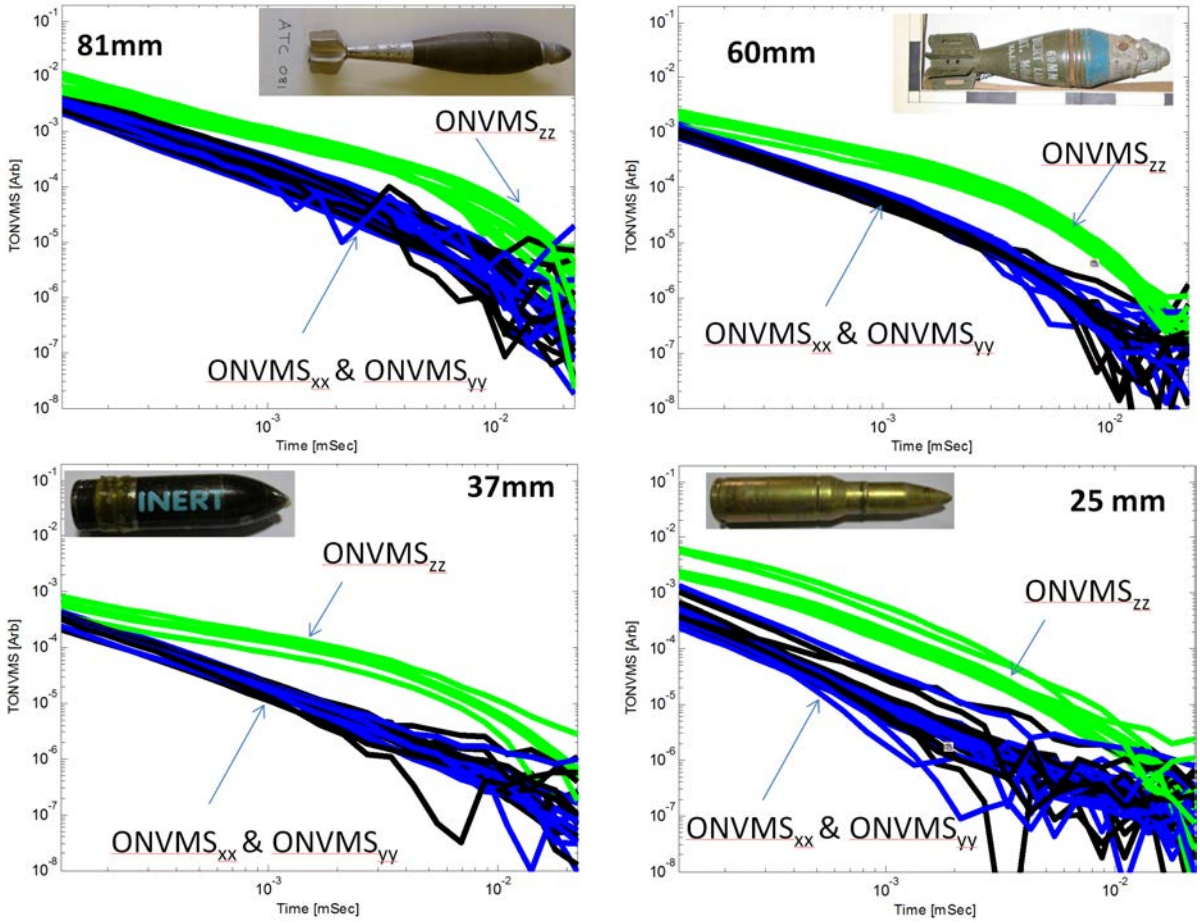

Figure 5.30: TONVMS results for 81mm, 60mm, 37mm, and 25mm ordnance in the blind grid at APG.

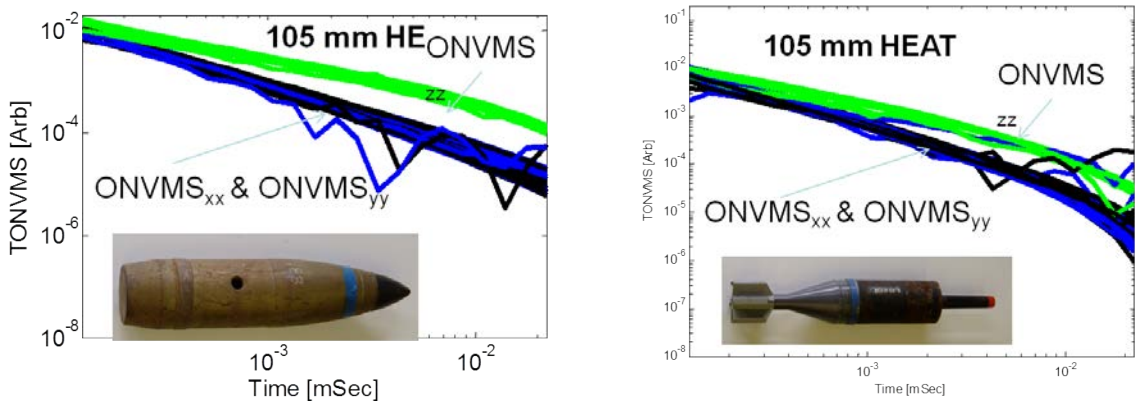

Figure 5.31: TONVMS results for 105mm HE and 105mm HEAT ordnance in the blind grid at APG.

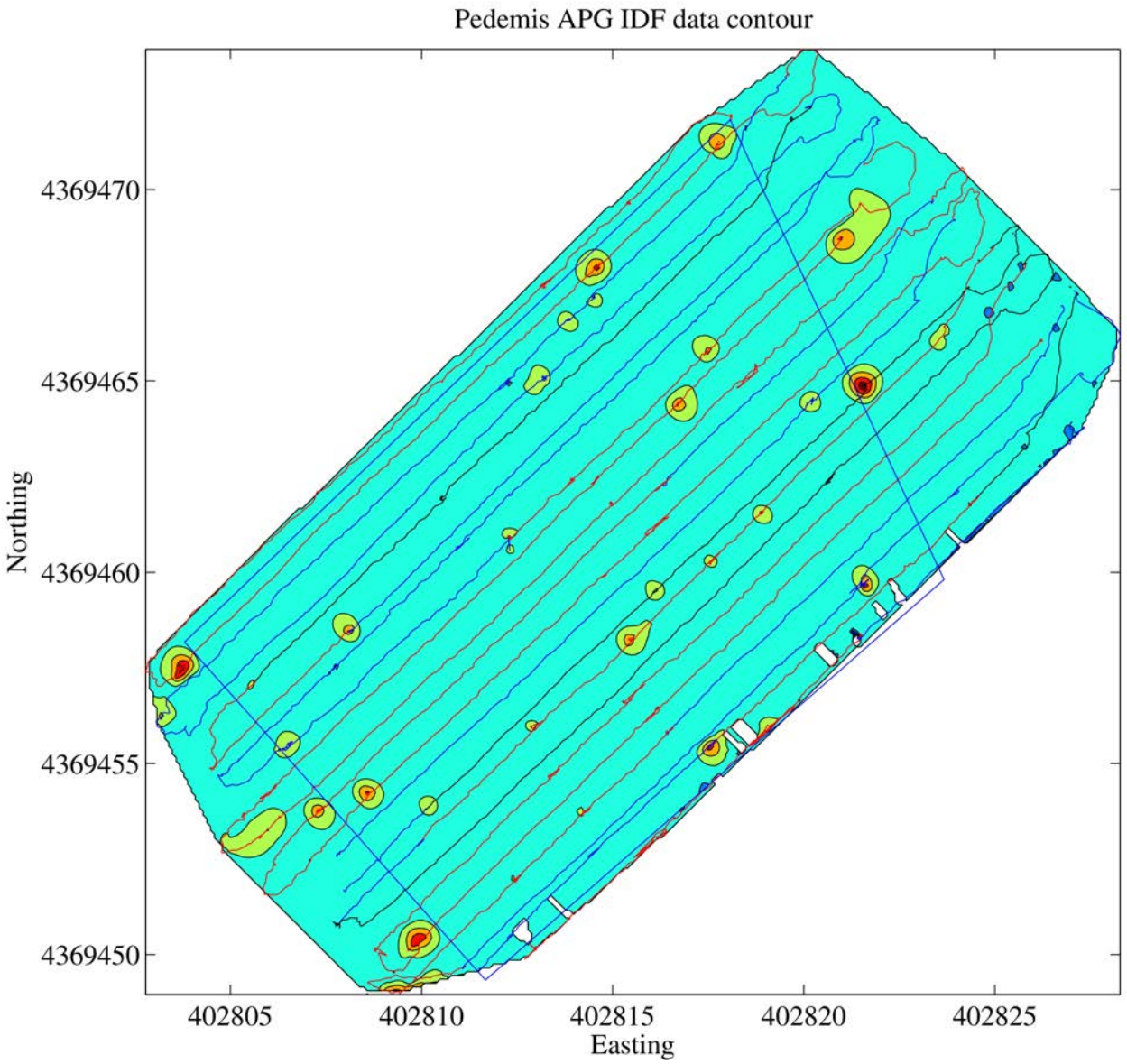

Figure 5.32: Contour map of data acquired in the IDF area by Pedemis.

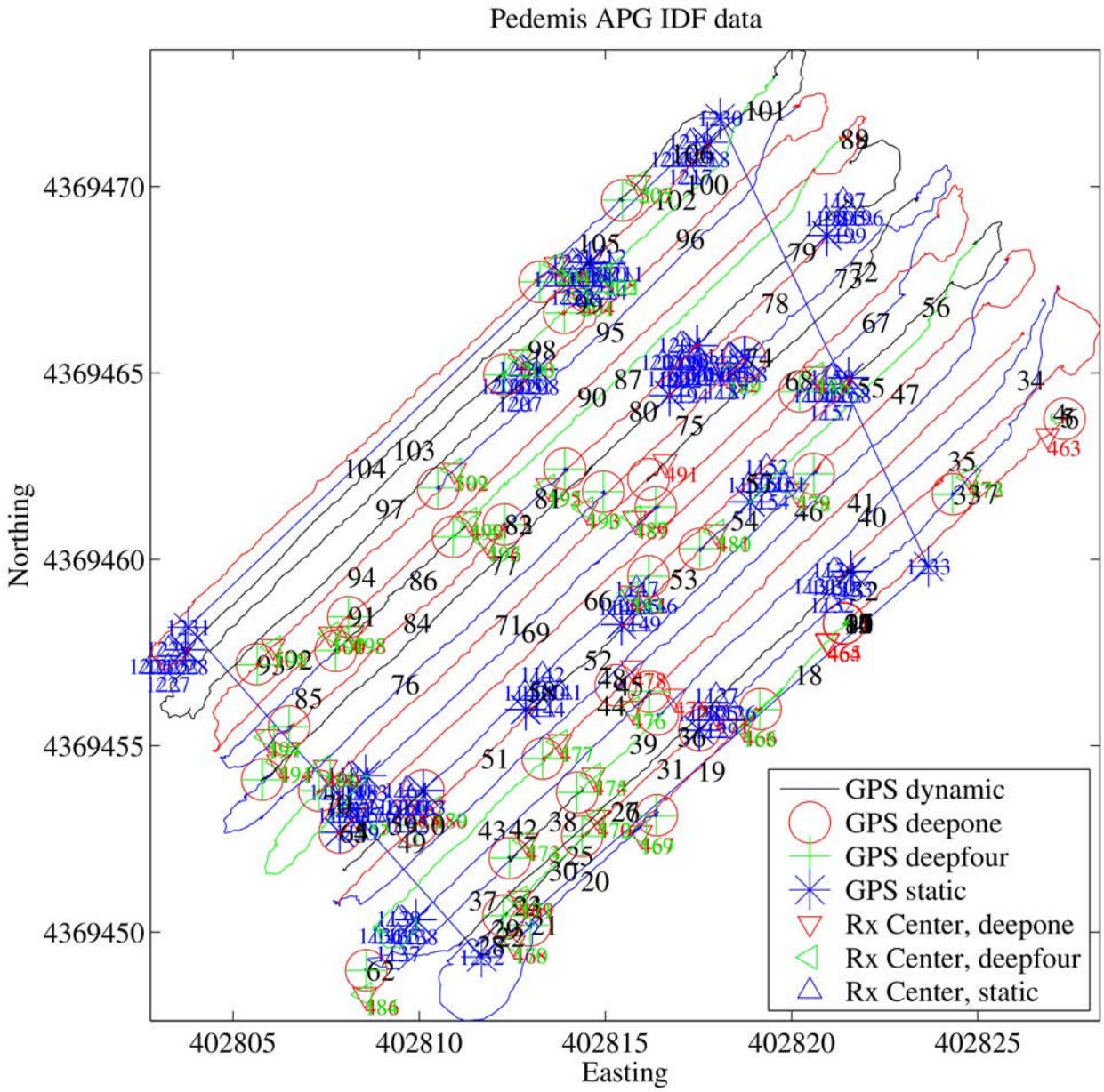

Figure 5.33: Data acquired in the IDF area by Pedemis.

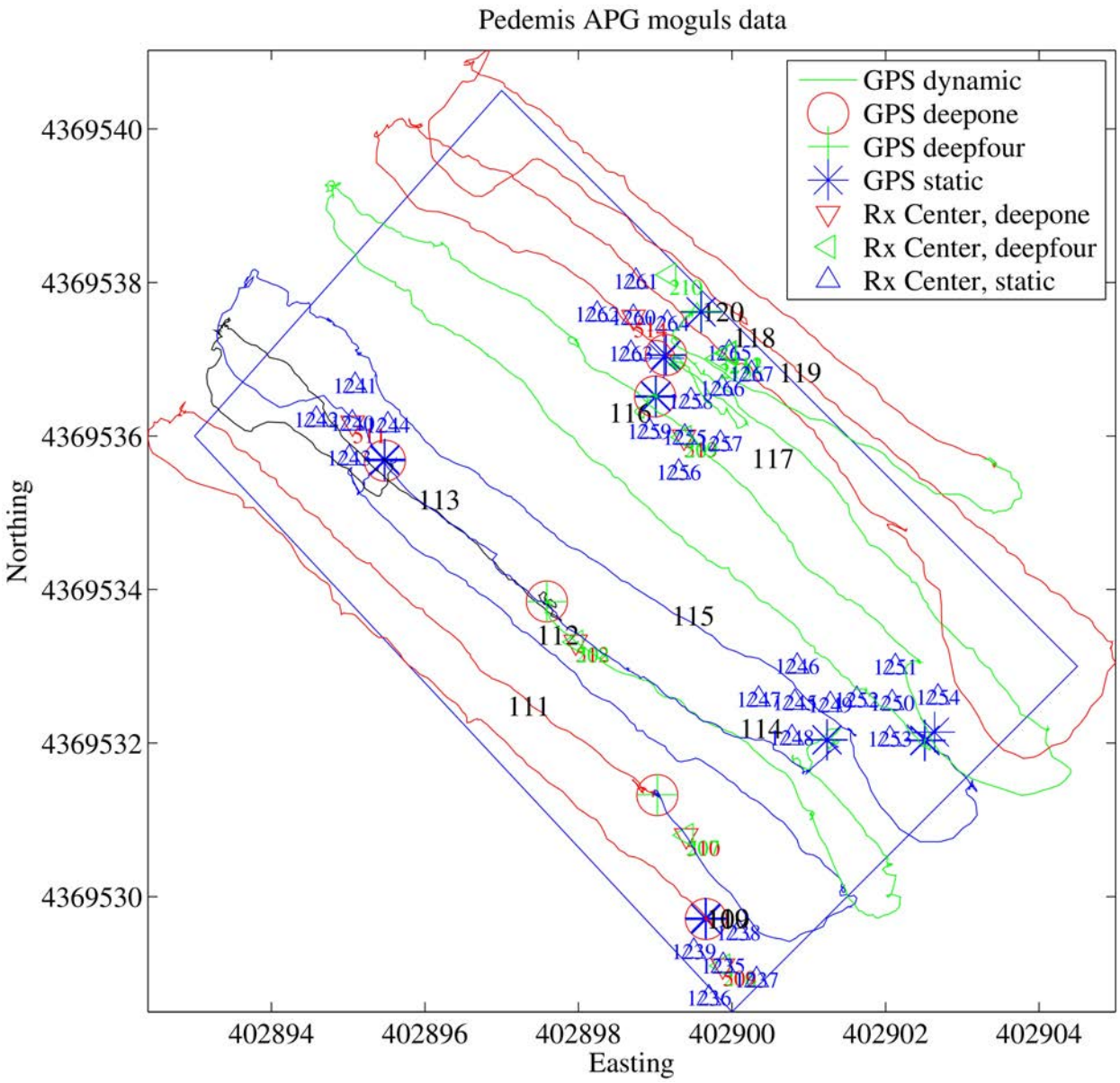

Figure 5.34: Data acquired in the mogul area by Pedemis.

6 Conclusions and Implications for Future Research/Implementation

Pedemis has been fabricated, tested, and deployed over the course of SERDP project MR-1712. Pedemis is a flexible platform that is man-portable, but also acquires high quality data is several interrogation modes. Specifically, Pedemis has the following advantages over other advanced EMI instruments:

- Potential one pass solution
- Hardware
  - 2-person portable design
  - Flexible (2-person portable, carted, sledded)
  - 1.2x1.2m, 3x3 Tx, 3x3 vector Rx (compromise between 2 and 5)
  - decoupled Rx (data diversity, spatial coverage)
  - Lighter, updated electronics
  - Integral positioning system
  - GPS and digital compass
  - Wide swath width and spatial coverage
- Software and processing
  - Real-time feedback to expert operators (field plots, arrows, and JD)
  - Data suited to advanced models (JD, ONVMS, MUSIC)
  - Flexible DAQ modes (detection, interrogation, deep detection, wide interrogation)
  - EM3D or LabVIEW interface

Results at Aberdeen Proving Ground demonstrated the capability of Pedemis to interrogate unknown anomalies. Pedemis is a new, advanced, EMI instrument with several deployment modes, data acquisition flexibility, lighter and less power hungry electronics, and achieves excellent results at standardized sites.

References

[1] Juan Pablo Fernandez, Benjamin Barrowes, Alex Bijamov, Tomasz Grzegorczyk, Nicolas Lhomme, Kevin O'Neill, Irma Shamatava, and Fridon Shubitidze. MPV-II: an enhanced vector man-portable emi sensor for uxo identification. volume 8017, page 801707. SPIE, 2011. doi: 10.1117/12.884085. URL http://link.aip.org/link/?PSI/8017/801707/1. iv, 6, 7, 10, 17, 22

[2] Tomasz M. Grzegorczyk, Benjamin E. Barrowes, Fridon Shubitidze, Juan Pablo Fernandez, and Kevin O'Neill. Simultaneous identification of multiple unexploded ordnance using electromagnetic induction sensors. IEEE Transactions on Geoscience and Remote Sensing, 2011. ISSN 01962892. URL http://dx.doi.org/10.1109/TGRS.2011.2108302. 4, 6, 55, 59, 85, 87

[3] Fridon Shubitidze, Juan Pablo Fernandez, Irma Shamatava, Benjamin E. Barrowes, and Kevin O'neill. Joint diagonalization applied to the detection and discrimination of unexploded ordnance. Geophysics, 77(4):WB149 – WB160, 2012. ISSN 00168033. URL http://dx.doi.org/10.1190/geo2011-0387.1. 4, 6, 52, 78

[4] F. Shubitidze, I. Shamatava, J.P. Fernandez, B.E. Barrowes, K. O'Neill, and A. Bijamov. Onvms applied to a new advanced portable emi system data. pages 145 – 148, Tbilisi, Georgia, 2012. 4, 6, 121

[5] Fridon Shubitidze, Ben Barrowes, Irma Shamatava, Juano Pablo Fernndez, and Kevin O'Neill. The orthonormalized volume magnetic source technique applied to live-site uxo data: Inversion and classification studies. SEG Special Issue, September 2011. 4, 6, 52, 79, 85

[6] F. Shubitidze, D. Karkashadze, J. P. Fernandez, B. E. Barrowes, K. O'Neill, Grzegorczyk, and I. Shamatava. Applying a volume dipole distribution model to next-generation sensor data for multi-object data inversion and discrimination. Detection and Sensing of Mines, Explosive Objects, and Obscured Targets Xv, 7664, 2010. doi: 10.1117/12.850651. 4, 6, 52, 79, 85

[7] F. Shubitidze, B. Barrowes, J. P. Fernández, and K. O'Neill. Combined NSMC and Pseudo-Spectral Finite-Difference Method for Inverting a Buried Object Location. Symposium on the Application of Geophysics to Engineering and Environmental Problems, 2007 . 4, 6, 79

[8] F. Shubitidze, B. Barrowes, J. P. Fernández, Irma Shamatava, and K. O'Neill. NSMC for UXO discrimination in cases with overlapping signatures. SPIE, 2007. 4, 6, 79

[9] F. Shubitidze, B. E. Barrowes, K. O'Neill, I. Shamatava, K. Sun, and K.D. Paulsen. Total normalized surface magnetic charge for UXO discrimination. NATO Advanced Study Institute "Imaging for Detection and Identification", 23 July–5 August 2006. Ciocco, Italy. 4, 6, 79

[10] F. Shubitidze, B. Barrowes, and K. O'Neill. Normalized surface magnetic charge for UXO discrimination: multiple objects. SERDP Partners Symposium, November 2006. Poster. 4, 6, 79

[11] F. Shubitidze, K. O'Neill, B. Barrowes, J. P. Fernández, I. Shamatava, K. Sun, and K.D. Paulsen. Application of the normalized surface magnetic charge model to UXO discrimination in cases with overlapping signals. J. Appl. Geophys., 61(3-4):292–303, Mar. 2007. 4, 6, 79

[12] F. Shubitidze, K. O'Neill, I. Shamatava, K. Sun, , and K. D. Paulsen. Total magnetic charge for fast screening of highly contaminated UXO sites. In proceedings of 2005 IEEE international symposium on Antennas and Propagation and USNC/CN/URSI North American Radio Science meeting, on CD, 2005. 4, 6, 79

[13] F. Shubitidze, K. O'Neill, I. Shamatava, K. Sun, and K.D. Paulsen. Total magnetic charge for fast screening of highly contaminated UXO sites. 2005 IEEE Antennas and Propagation Society International Symposium (IEEE Cat. No. 05CH37629), vol. 3A:856 – 9, 2005. 4, 6, 79

[14] Fridon Shubitidze, Kevin O'Neill, Irma Shamatava, Keli Sun, and Keith Paulsen. Combined differential evolution and surface magnetic charge model algorithm for discrimination of UXO from non-UXO items: Simple and general inversions. Proceedings of SPIE - The International Society for Optical Engineering, 5794(Part I):346 – 357, 2005. ISSN 0277-786X. 4, 6, 79

[15] L. R. Pasion. A unified approach to uxo discrimination using the method of auxiliary sources. Technical report, 2006. 4, 6, 79

[16] B. E. Barrowes, K. O'Neill, T. M. Grzegorczyk, X. Chen, and J. A. Kong. Broadband analytical magnetoquasistatic electromagnetic induction solution for a conducting and permeable spheroid. IEEE Trans. on Geoscience and Remote Sensing, 42(11):2479–2489, 2004. 4, 6

[17] B. E. Barrowes, K. O'Neill, T. M. Grzegorczyk, and J. A. Kong. On the asymptotic expansion of the spheroidal wave function and its eigenvalues for complex size parameter. Studies in Applied Mathematics, 113(3):271–301, Oct. 2004. 4, 6

[18] Chi On Ao, Henning Braunisch, Kevin O'Neill, and Jin Au Kong. Quasi-magnetostatic solution for a conducting and permeable spheroid with arbitrary excitation. IEEE Trans. Geosci. Remote Sensing, 40:887–897, Apr. 2002. 4, 6

[19] Henning Braunisch, Chi On Ao, Kevin O'Neill, and Jin Au Kong. Magnetoquasistatic response of conducting and permeable prolate spheroid under axial excitation. IEEE Trans. Geosci. Remote Sensing, 39:2689–2701, Dec. 2001. 4, 6

[20] X. Chen, K. O'Neill, B. E. Barrowes, T. M. Grzegorczyk, , and Jin Au Kong. Application of a spheroidal mode approach with differential evolution in inversion of magneto-quasistatic data for UXO discrimination. Inverse Problems, 20(6):27–40, 2004. 4, 6

[21] F. Shubitidze, K. O'Neill, K. Sun, and I. Shamatava. Application of broadband EMI responses to infer buried object's aspect ratio. International Geoscience and Remote Sensing Symposium (IGARSS), 3:1542 – 1545, 2002. 4, 6

[22] Benjamin E. Barrowes, Kevin O'Neill, Tomasz M. Grzegorczyk, and J. A. Kong. Broadband, Analytic Electromagnetic Induction (EMI) Response from Spheroidal Objects for Arbitrary Excitation. Progress in Electromagnetics Research Symposium (PIERS), October 2003. 4, 6

[23] I. J. Won, D. A. Keiswetter, D. Hansen, E. Novikova, and T. M. Hall. Gem-3: a monostatic broadband electromagnetic induction sensor. Jour. Envir. Eng. Geophysics, 2(1):53–64, 1997. 5

[24] J. Duncan McNeill and Miro Bosnar. Application of TDEM techniques to metal detection and discrimination: a case history with the new Geonics EM-63 fully time-domain metal detector. Technical Note TN-32. Missisauga, ON: Geonics LTD (http://www.geonics.com), 2000. 5

[25] W. P. Delaney and D. Etter. Report of the defense science board task force on unexploded ordnance. Final tech. rep. a079914, Defense Sci. Board, Washington DC, 2003. 5

[26] S.D. Billings. Discrimination and classification of buried unexploded ordnance using magnetometry. IEEE Trans. Geosci. Remote Sens. (USA), 42(6):1241 – 51, 2004. ISSN 0196-2892. 5

[27] Yan Zhang, Leslie Collins, Haitao Yu, Carl E. Baum, and Lawrence Carin. Sensing of unexploded ordnance with magnetometer and induction data: Theory and signal processing. IEEE Trans. Geosci. Remote Sensing, 41: 1005–1015, May 2003. 5

[28] Fridon Shubitidze, Irma Shamatava, Alex Bijamov, Ben Barrowes, and Kevin O'Neill. Camp butner uxo data inversion and classification using advanced emi models. 2010. SERDP-MR-1572. 6

[29] L. Pasion. Uxo discrimination using full coverage and cued interrogation data sets at camp butner, nc. SERDP-ESTCP Partners Symposium, 2010. 6

[30] Mark Prouty. Draft demonstration plan: Detection and classification with the MetalMapper™ at former Camp San Luis Obispo. San Jose, CA: Geometrics, Inc. (http://www.geometrics.com), 2009. 6

[31] H. Nelson, D. A. Steinhurst, B. Barrow, T. Bell, N. Khadar, B. SanFilipo, and I. J. Won. Enhanced UXO discrimination using time-domain electromagnetic induction. Final report to the ESTCP program office (DOD) Arlington VA for project MM-0601, Naval Research Laboratory, 2007. URL http://oai.dtic.mil/oai/oai?&verb=getRecord&metadataPrefix=html&identifier=ADA469893. Accession Number : ADA469893. 6, 10

[32] MR-201165, 2011. URL http://www.serdp.org/Program-Areas/Munitions-Response/Land/Live-Site-Demonstrations/MR-201165/MR-201165. 6

[33] J.P. Fernandez, B. Barrowes, K. O'Neill, I. Shamatava, and F. Shubitidze. A vector handheld frequency-domain sensor for uxo identification. In Proceedings of the SPIE - The International Society for Optical Engineering, volume 7303, pages 73030W (12 pp.) –, USA, 2009. URL http://dx.doi.org/10.1117/12.818812. 6

[34] F. Shubitidze, B. Barrowes, I. Shamatava, J. P. Fernández, and K. O'Neill. Combining NSMC and High Quality MPV-TD Data for UXO Discrimination. Proc. IEEE Int. Geosci. Remote Sensing Symp. (IGARSS), 2008. 7, 17

[35] Fridon Shubitidze, Juan Pablo Fernández, Benjamin E. Barrowes, Irma Shamatava, and Kevin O'Neill. Normalized Surface Magnetic Source model applied to Camp Sibert data. In Applied Computational Electromagnetics Symposium (ACES), Monterey, CA, Mar. 2009. 8

[36] W. M. Wynn, C. P. Frahm, P. J. Carroll, R. H. Clark, J. Wellhoner, and M. J. Wynn. Advanced superconducting gradiometer/magnetometer arrays and a novel signal processing technique. IEEE Transactions on Magnetics, MAG-11(2):701 – 707, 1975. URL http://dx.doi.org/10.1109/TMAG.1975.1058672. 8

[37] Benjamin E. Barrowes, Fridon Shubitidze, Tomasz M. Grzegorczyk, Pablo Fernndez, and Kevin O'Neill. Pedemis: a portable electromagnetic induction sensor with integrated positioning. SPIE, pages 835702–835702–10, 2012. doi: 10.1117/12.918321. URL +http://dx.doi.org/10.1117/12.918321. 8, 121

[38] Benjamin E. Barrowes, Tomasz M. Grzegorczyk, Fridon Shibitidze, Pablo Fernndez, and Kevin O'Neill. The pedemis instrument: operation and apg field results. pages 870903–870903–11, 2013. doi: 10.1117/12.2014964. URL +http://dx.doi.org/10.1117/12.2014964. 8, 36, 88, 121

[39] William A. SanFilipo, Stephen J. Norton, and I. J. Won. Precision local positioning of an EMI sensor using the transmitter as a beacon. In 2007 SERDP-ESTCP Partners in Environmental Technology Technical Symposium & Workshop, Washington, DC, Dec. 2007. 30

[40] Nicolas Lhomme, Benjamin E. Barrowes, and David C. George. EMI sensor positioning using a beacon approach. In Russell S. Harmon, John H. Holloway, Jr., and J. Thomas Broach, editors, Detection and Sensing of Mines, Explosive Objects, and Obscured Targets XVI, volume 8017 of Proceedings of SPIE, pages 8017–0C, Bellingham, WA, Apr. 2011. 30

[41] Juan Pablo Fernández, Benjamin E. Barrowes, Kevin O'Neill, Irma Shamatava, and Fridon Shubitidze. A vector handheld frequency-domain sensor for UXO identification. In Russell S. Harmon, J. Thomas Broach, and John H. Holloway, Jr., editors, Detection and Sensing of Mines, Explosive Objects, and Obscured Targets XIV, volume 7303 of Proceedings of SPIE, pages 7303–0W, Bellingham, WA, Apr. 2009. 30

[42] Juan Pablo Fernández, Benjamin E. Barrowes, Nicolas Lhomme, Alex Bijamov, Tomasz Grzegorczyk, Kevin O'Neill, Irma Shamatava, and Fridon Shubitidze. MPV-II: an enhanced vector man-portable EMI sensor for UXO identification. In Russell S. Harmon, John H. Holloway, Jr., and J. Thomas Broach, editors, Detection and Sensing of Mines, Explosive Objects, and Obscured Targets XVI, volume 8017 of Proceedings of SPIE, pages 8017–06, Bellingham, WA, Apr. 2011. 30

[43] William R. Smythe. Static and Dynamic Electricity. McGraw-Hill, New York, 3rd edition, 1968. 30

[44] Lloyd Nicholas Trefethen. Spectral Methods in Matlab. SIAM, Philadelphia, PA, 2000. 30

[45] Edward Mills Purcell. Electricity and Magnetism. Cambridge Univ. Press, Cambridge, UK, 2nd edition, 2011. 35

[46] Edward B. Rosa. The self and mutual inductances of linear conductors. Bulletin of the Bureau of Standards, 4 (2):301–344, 1908. 35

[47] Frederick W. Grover. Inductance Calculations: Working Formulas and Tables. Dover, New York, 1962. 35

[48] E. Durand. Magnétostatique. Masson, Paris, 1968. 35

[49] F. F. Martens. Über die gegenseitige Induktion ponderomotorische Kraft zwischen zwei stromdurchflossenen Rechtecken. Ann. Phys. (Leipzig), 29:959–970, 1909. 38

[50] George A. Campbell. Mutual inductances of circuits composed of straight wires. Phys. Rev., 5(6):452–458, 1915. 38

[51] T. M. Grzegorczyk and B. E. Barrowes. Real-time processing of electromagnetic induction dynamic data using kalman filters for unexploded ordnance detection. Geoscience and Remote Sensing, IEEE Transactions on, (99): 1–13, 2012. ISSN 0196-2892. doi: 10.1109/TGRS.2012.2222032. 47

[52] I. Shamatava, F. Shubitidze, R. Joabava, B.E. Barrowes, K. O'Neill, and A. Bijamov. Application of the onvms model to discriminate challenging uxo targets. pages 141 – 144, Tbilisi, Georgia, 2012. 52

[53] Aberdeen proving ground soil survey report. Technical report, APG, October, 1998. 74

[54] Fridon Shubitidze, Juan Pablo Fernndez, Benjamin E. Barrowes, Irma Shamatava, Alex Bijamov, Kevin O'Neill, and David Karkashadze. The orthonormalized volume magnetic source model for discrimination of unexploded ordnance. TGRS, approved for publication 2012. 79, 85

[55] Alex Bijamov. Numerical Methods in Electromagnetics: Evanescent Nanometry for DNA Sequencing, and EM Induction for UXO Detection and Discrimination. PhD thesis, Dartmouth College, 2011. 79, 85

[56] John David Jackson. Classical Electrodynamics. Wiley, New York, 2nd edition, 1975. 87

[57] T. H. Bell, B. J. Barrow, and J. T. Miller. Subsurface discrimination using electromagnetic induction sensors. IEEE Trans. on Geoscience and Remote Sensing, 39(6):1286–1293, June 2001. 87

[58] Juan Pablo Fernández, Benjamin E. Barrowes, Tomasz M. Grzegorczyk, Nicolas Lhomme, Kevin O'Neill, and Fridon Shubitidze. A man-portable vector sensor for identification of unexploded ordnance. IEEE Sensors Journal, 11:2542–2555, Oct. 2011. 121

[59] Tomasz M. Grzegorczyk and Benjamin E. Barrowes. Operation of the pedemis sensor at the aberdeen proving ground standardized test site: Single and multi-target inversions. Geoscience and Remote Sensing Letters, 2013. Accepted for publication. 121

[60] Tomasz M. Grzegorczyk, Juan Pablo Fernandez, Fridon Shubitidze, Kevin O'Neill, and Benjamin E. Barrowes. Subsurface electromagnetic induction imaging for unexploded ordnance detection. Journal of Applied Geophysics, 79:38 – 45, 2012. ISSN 09269851. URL http://dx.doi.org/10.1016/j.jappgeo.2011.12.014. 121

[61] Juan Pablo Fernndez, Benjamin Barrowes, Kevin O'Neill, Irma Shamatava, and Fridon Shubitidze. Toward a real-time positioning system for a portable emi sensor. pages 870902–870902–10, 2013. doi: 10.1117/12.2016245. URL +http://dx.doi.org/10.1117/12.2016245. 121

[62] Tomasz M. Grzegorczyk, Benjamin Barrowes, David George, Fridon Shubitidze, J. P. Fernandez, and Kevin O'Neill. Rapid position estimation using electromagnetic induction data from the metalmapper in dynamic mode. volume 8017, page 801705. SPIE, 2011. doi: 10.1117/12.884059. URL http://link.aip.org/link/?PSI/8017/801705/1. 121

[63] Benjamin E. Barrowes, Fridon Shubitidze, and Steven Grant. Detection of buried conductive nonmetallic targets by electromagnetic. MSS BAMS Conference, Oct 2012. 121

A Supporting Data

A.1 G&G Sciences, Inc. Final Report

FABRICATION OF A PORTABLE BISTATIC INDUCTION SENSOR WITH INTEGRATED POSITIONING

FINAL REPORT

Contract #W913E5-10-C-0015

SERDP Project MR-1712

Submitted to

Technical Point of Contact
Dr. Benjamin Barrowes
U. S. Army Engineer R&D Center,
Cold Regions R&E Laboratory
72 Lyme Road
Hanover, NH 03755-1290
(603) 646-4312

by

G&G SCIENCES, INC.
873 23 Road
Grand Junction, CO 81505

Point of Contact: David C. George
(970) 263-9714
dgeorge@ggsciences.com
June 2012

TABLE OF CONTENTS

TABLE OF CONTENTS 2

INTRODUCTION 3

HISTORY OF THE PROJECT 4

HIGHLIGHT PICTURES 7

CONCLUSIONS 13

DRAFT

INTRODUCTION

CRREL was awarded a project by the Strategic Environmental Research and Development Program (SERDP) for the year 2010. G&G Sciences (G&G) assisted in a minor role in preparation of the proposal that won this award. The project was awarded in 2010 as project MR-1712: *Bistatic Portable Eelectromagnetic Induction Sensor with Integrated Positioning*.

G&G submitted a proposal to CRREL in February 2010 in response to ERDC BAA, Specific Research Area CRREL-1, sub-item 10: *Electromagnetic remote sensing and sub-surface detection of buried metal objects including UXOs*. Contract W913E5-10-C-0015 was awarded to G&G in April 2010 and continued through June 2013.

The objective of the project was to build and test a new metal detection system dubbed *Portable Decoupled Metal Interrogation System* (PEDEMIS). G&G's participation in the project was to assemble the hardware and to participate in field testing.

In the course of this project, the PEDEMIS was successfully designed, fabricated, and tested. A history of progress on the project and highlights of that progress are shown in this report.

DRAFT

HISTORY OF THE PROJECT

As originally proposed, G&G's participation in the first year was to have been to support CRREL scientists in system studies to create a conceptual system design. G&G's participation through the remainder of 2010 was minimal as G&G's support was not needed. The conceptual design of the system was created by CRREL scientists near the end of 2010. It is shown in Figure 1. The system was designed to use nine transmitting loops of a design that had previously been developed by G&G for a system known as TEMTADS. The system was also designed to use G&G receiving sensors known as "cubes" in several related induction systems. The novel part of the PEDEMIS, in terms of physical fabrication and use, was physically separating the receiving sensors from the transmitter loops.

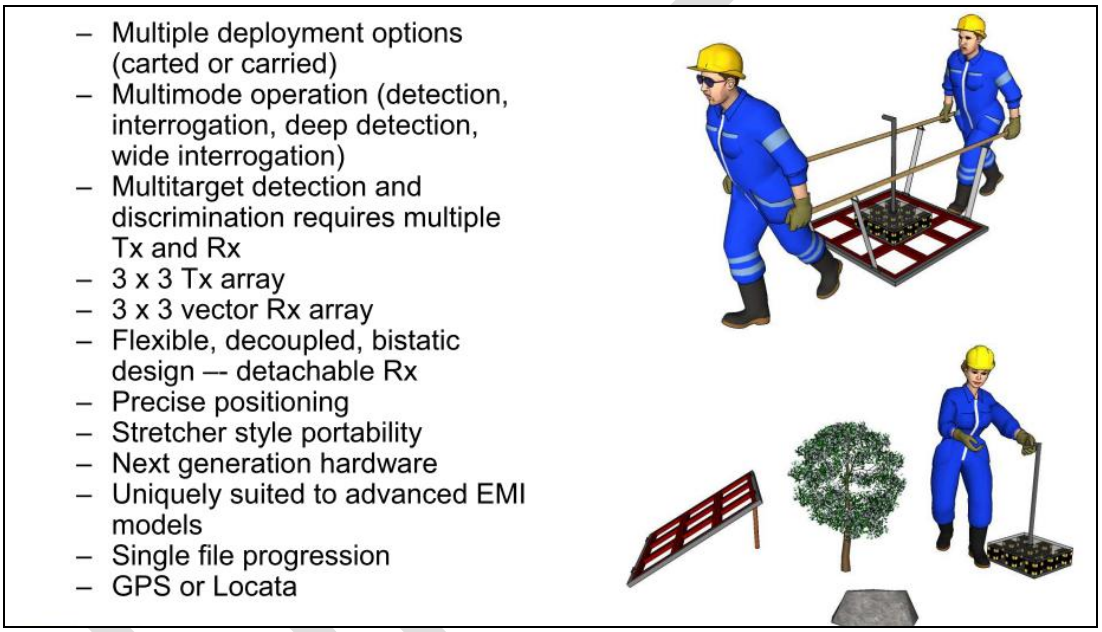

Figure 1 Conceptual design of the PEDEMIS system

In the course of the project, it was jointly determined between G&G and CRREL that this system would be fabricated using a newly available data acquisition system from National Instruments, known as Compact RIO (cRIO) and/or Compact DAQ.(cDAQ). These two systems are physically similar– they use the same acquisition modules and are packaged in similar chasses. The significant difference between the two is electrical performance (speed) and software.

The cRIO system contains a Field Programmable Gate Array (FPGA) that provides interfaces to the data acquisition modules, whereas the cDAQ system contains a dedicated processor that provides interfaces to the data acquisition modules. The FPGA is substantially faster and has more precise timing and can handle higher data rates. The FPGA requires separate software (firmware) development and this programming is difficult. The cDAQ can be programmed using software known as DAQmx that is the same software used to program previously fabricated systems known as PXI. The cDAQ system has a limitation in that it transmits data from the acquisition modules to an external computer through a solitary Universal Serial Bus (USB) cable, with no opportunity to reduce data volume, so data rate is limited to USB-2 speeds. Thus the challenge to develop a cRIO system is to develop the software/firmware to control the transmitters and to collect raw data from the data acquisition modules and to reduce its volume (decimation or gating) before transmission to a main personal computer (PC) via USB.

Since that the PEDEMIS contains nine, 3D receiving sensors, it requires 27 receiver channels. Since raw data rates need to be on the order of at least a couple hundred kilo-samples per second per channel, acquisition data

rates are on the order of 20 MBytes/s. For this speed it was jointly decided to use cRIO instead of cDAQ. With that choice, the challenge became one of developing software/firmware for a system that was compatible only with National Instruments software *LabView*. LabView provides a capability to program the FPGA in the cRIO but the complete application requires a user interface, and substantial data handling (e.g. gating with variable parameters), and substantial data interpretation/display (e.g. plotting). Thus the challenge became one of duplicating software that already existed in previous metal detection systems developed by G&G, the program EM3D. The CRREL principle investigator (PI) undertook the task to provide this programming because G&G's proposal and contract did not include this scope of work.

In July, 2011, a cRIO system was purchased from National Instruments. It included LabView development software. The PI began development of LabView software and G&G began assembly of experimental hardware. Over the next three months, transmitting loops were fabricated and receiver sensors were fabricated. For purposes of bench testing and for purposes of software/firmware, experimental, temporary hardware was assembled to operate the newly fabricated loops/sensors and the cRIO acquisition system. These electronics were laboratory modules used during development of other systems that had been based on the data acquisition systems known as '*PXI.*' They consisted of a transmitter module and a 16-channel receiver module that were prototypes of MetalMapper circuits. These modules served as 'adapter' modules to allow use of the Pedemis 3x3 Tx array, and to the 5-cube head used in the MPV2. The MPV2 was logical because it uses 8-cm cubes identical to those in the actual Pedemis receiving head, and their spatial distribution is similar to Pedemis.

In November 2011, the PI visited G&G. Evolutionary software was tested and some basic data were collected using the hardware described in the previous paragraph. This was a milestone achievement in the project. It was the first demonstration of the highly-similar geometry to that proposed for the Pedemis array and it was the first demonstration of the use of National Instruments cRIO data acquisition system.

From February to May 2012, G&G designed and fabricated electronics modules to support the PEDEMIS loop/sensor array. The modules were designed in a new form-factor compatible with the cRIO/cDAQ chasses – the designs, while not new at the schematic level, were new circuit-board layouts, new packages, and new cabling. No particular problems were encountered in the fabrication other than usual engineering developments.

During the course of testing and debugging the newly designed electronics, it became increasingly difficult for G&G to test and debug the new modules. In these systems, performance of the hardware can be determined only through use of rather complicated software because speed and dynamic range cannot be measured with usual laboratory instruments. After a frustrating effort to implement necessary routines in the LabView language, G&G determined that checkout could be done more efficiently if a separate cDAQ chassis were procured so that existing G&G software could be used.

So in June 2011, G&G procured a cDAQ chassis and modified existing software, program EM3D, to be compatible with the cDAQ acquisition hardware. This allowed operation of all of the hardware, but at a somewhat reduced data sampling rate: 200KS/s instead of 500KS/s. Between May 2012 and August 2012, G&G completed fabrication and testing of the hardware using the cDAQ chassis. While the PI continued development of LabView software, the performance of the system using the cDAQ chassis, was better than had been originally projected. In the final analysis, it was determined to use the cDAQ chassis as the final implementation of the PEDEMIS.

From June through August, G&G's activities were focused on debugging software, particularly a couple of difficult differences in coding needed to configure the system, that were different than that experienced using PXI data acquisition components. Also the progress allowed discovery and repair of multiple *bugs* in the newly fabricated hardware.

Using a variable geometry between transmitters and sensors adds a requirement that separate means needed to be created to be able to precisely determine the geometry for every measurement. CRREL scientists developed a means to determine that geometry by sensing the primary field from the transmitter loops. G&G developed software that allowed the *on-time* signals to be saved and presented as data. Previously this data had been discarded for all receiving channels.

On August 14-16, the PI again visited Grand Junction to perform data collection and tests with the new hardware/software. The tests served as a skeleton for the configuration required next – that was the planned operation of the system for Demonstration testing at Aberdeen. This was another milestone in the project.

In September, a small, dedicated processor was purchased and added to the cDAQ acquisition system. Prior to this, a G&G laboratory desktop computer had served as the PC for the data acquisition system. In September and October, the system was packaged to be transportable in preparation for tests at Aberdeen Proving Ground. An orientation sensor from Xsens Inc. was procured and added to the system. Even though previous Xsens sensors had been used without problem, this new sensor was an 'improved' model, and it posed software difficulties that were difficult to solve. These difficulties were eventually traced to Xsens software provided to drive the sensor. Eventually it was learned that G&G could modify the cable between sensor and PC so that it became a serial interface instead of a USB interface, and this allowed G&G to bypass the software package that was the problem.

In October, final plans and preparations were made for the tests at Aberdeen. These tests were originally scheduled to be the last week of October. However, the scheduled first week of testing exactly coincided with the arrival of Hurricane Sandy so plans were modified at the last moment. The tests at Aberdeen were carried out during the first two weeks of November.

G&G assisted the PI with the tests at Aberdeen. But as planned, the data was analyzed by the PI and G&G's involvement in the project was essentially complete at the end of the Aberdeen tests.

In discussions with the PI, other investigators within the SERDP and ESTCP programs, the SERDP/ESTCP program manager, it was decided that the Pedemis hardware should be modified to become a system known as 3x3x3D in order to be used for ongoing projects within the SERDP/ESTCP programs. As this final report is written, the system has been modified and is undergoing further testing within SERDP Project MR-2225.

DRAFT

HIGHLIGHT PICTURES

Highlights of progress during the project are shown in this section. Fundamental accomplishments were design and fabrication of the Pedemis Sensor array, design and assembly of the data acquisition system based on a new form factor – National Instruments cDAQ, and adaptation of existing software to acquire data using the cDAQ. Two fundamental milestones in the project were completion of the hardware and associated software, and performance of demonstration tests at Aberdeen Proving Ground.

Figures 1 showed the design that was presented to project participants. The sensor head contains a single transmitting loop wound in two sections like a sandwich with receiver 'cubes' between. This was done to allow moving the positions of the receiver cubes from inside the transmitter winding to outside the transmitter winding.

A picture of the Pedemis antenna/sensor array during fabrication and initial tests is shown in the left panel of Figure 2 and in Figures 3 and 4. The electronics assembled for the tests in November 2011 are shown in Figure 2.

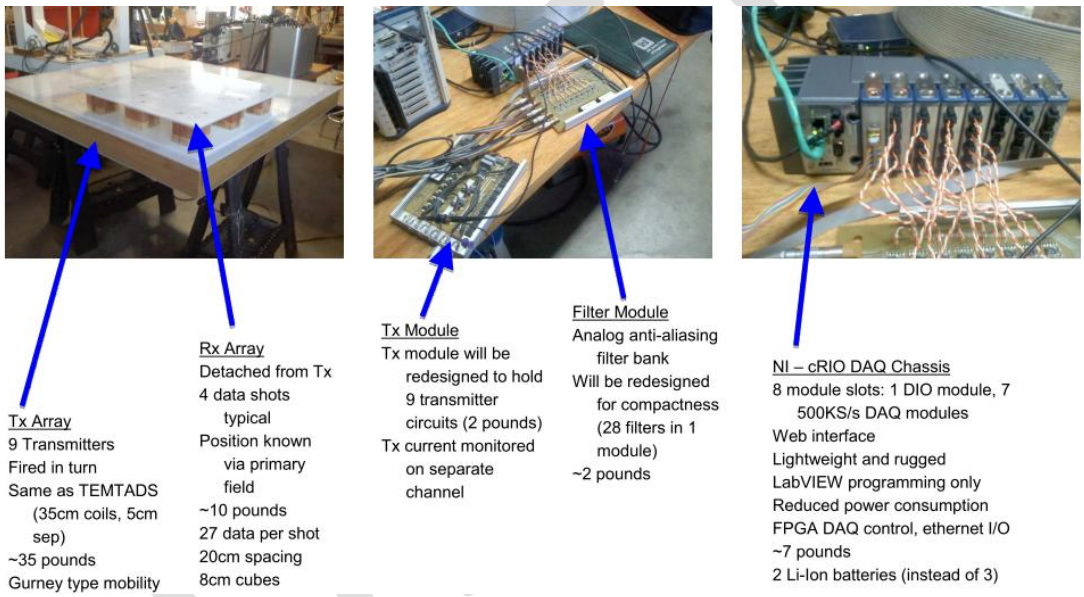

Figure 2 Hardware implemented for concept tests conducted in November, 2011

A picture of the MPV sensor array being used for the concept tests in November 2011 is shown in Figure 3. In these tests, one transmitter loop was activated at a time, and signals were received from the 5 cube sensors in the MPV head.

Figure 3 Typical setup of Tx loops and MPV2 sensors during tests made in November 2011.

A picture of the receiver cubes and the assembled receiver array is shown in Figure 4. There are nine receiver sensors arranged in a 3x3 array. Each cube produces three signals proportional the orthogonal components of their ambient dB/dt field.

DRAFT

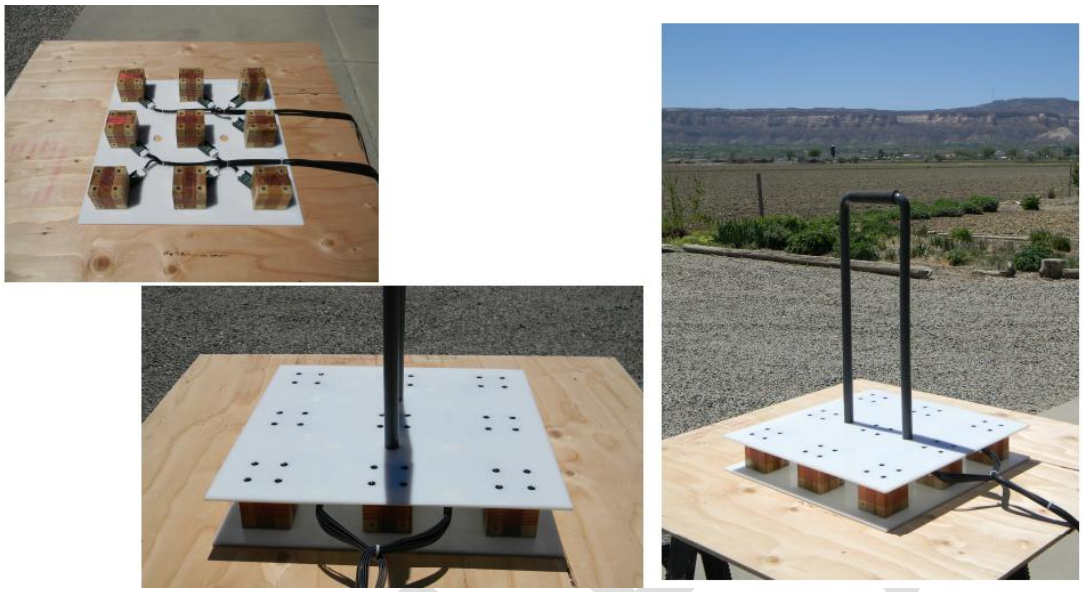

Figure 4 Pedemis Receiver Array

A picture of the transmitter loop array during construction is shown in the left half of Figure 5 and the assembled array is shown in the right half. Each of the transmitter loops are 35x35cm and their centers are spaced on a 40cm grid.

Figure 5 Pedemis Transmitter Array during and after assembly.

Electronics modules fabricated by G&G during this project are shown in Figure 6. There are two modules at the right end that contain dc-dc converters for power. The next module to the left is the master-control module for the transmitter. The next three modules each contain drivers for three transmitter loops. Finally the last three modules are receiver modules each capable of handling 12 channels. The last module is only partly loaded with electronics components since the system needed only 28 of the 36 possible channels. The assembled modules are shown in the right half of Figure 5. Heat, particularly that heat produced by transmitter switches when

continuously running the system, is conducted out of the system by conduction out of the aluminum modules. The modules are spaced to allow convection between the modules.

Figure 6 Transmitter and receiver electronics modules fabricated for Pedemis

Figure 7 shows more detailed vies of both the cRio data acquisition module and the Pedemis electronics modules. When the cRio Daq was replaced by the cDaq, the system used all of the same modules. The only difference is the permanent-chassis component on the left – this is a PowerPC CPU for the cRio system and an internal dedicated processor for cDaq.

Figure 8 shows the antenna array as it was tested in the final checkout tests in August 2012.

Figure 7 Close-up details of the cRio data acquisition system with the Pedemis electronics modules.

Figure 8 Typical setup for experiments conducted in August 2012.

Figure 9 shows a computer screen during the August tests, to demonstrate the software that was able to be implemented. The picture shows the dancing arrows display familiar to users of the program EM3D, and it shows

a detected target under the array. The display also shows a *data timeout* message indicating a problem that existed at that time in the software driving the cDaq acquisition system.

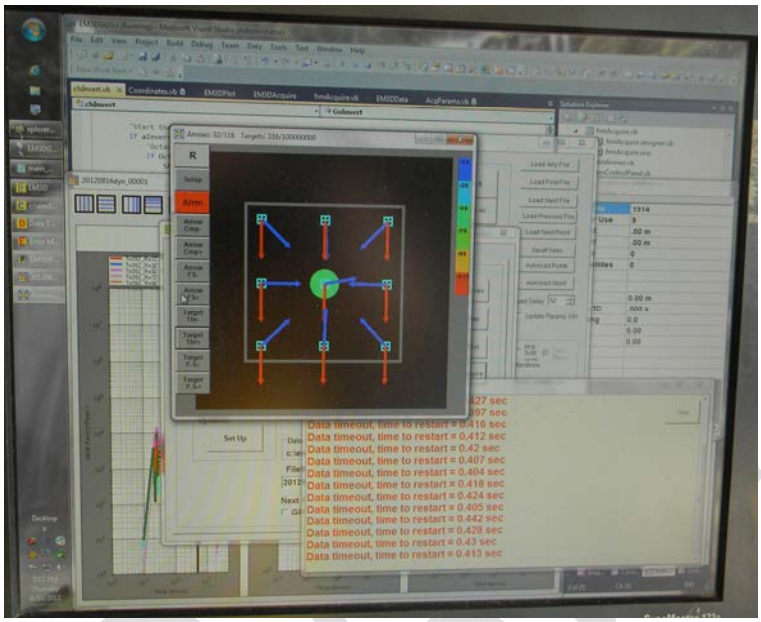

Figure 9 Computer screen picture of the target detection algorithm demonstrated during tests in August 2012. The algorithm was able to be implemented because of the change to the cDAQ system so that previously developed software could be used.

DRAFT

CONCLUSIONS

- The Pedemis system was successfully designed, fabricated, tested, and demonstrated.
- The performance of the Pedemis antenna array is contained in work performed by the principal investigator.
- The data acquisition system based on the National Instruments cDAQ form factor now provides a substantial advance in field ability for the current generation of advanced metal-detection induction systems – weight, ruggedness, power requirements.

DRAFT

B List of Scientific/Technical Publications

Publications written with full or partial funding from this project are [4, 37, 38, 58–63].

C Other Supporting Materials

C.1 Official APG Results

SECTION 4. TECHNICAL PERFORMANCE RESULTS

4.1 ROC CURVES USING ALL MUNITIONS CATEGORIES

The probability of detection for the response stage (P_d^{res}) and the discrimination stage (P_d^{disc}) versus their respective probability of clutter detection or probability of false positive within each area are shown in Figures 3 through 8. The probabilities plotted against their respective background alarm rate within each area are shown in Figures 9 through 14. Both figures use horizontal lines to illustrate the performance of the demonstrator at two demonstrator-specified points: at the system noise level for the response stage, representing the point below which targets are not considered detectable, and at the demonstrator's recommended threshold level for the discrimination stage, defining the subset of targets the demonstrator would recommend digging based on discrimination. Note that all points have been rounded to protect the GT.

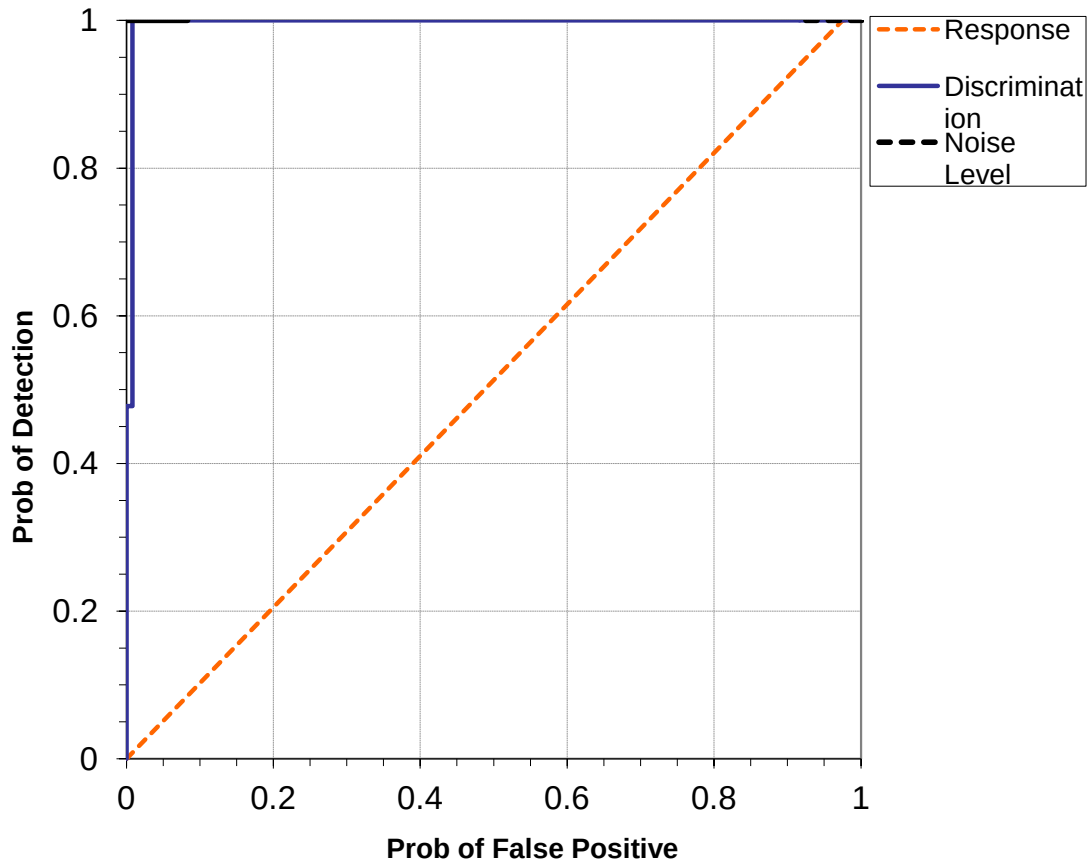

Figure 3. PEDEMIS/handheld blind grid probability of detection for response and discrimination stages versus their respective probability of false positive.

Not covered

Figure 4. PEDEMIS/handheld open field (direct fire) probability of detection for response and discrimination stages versus their respective probability of false positive.

Not covered

Figure 5. PEDEMIS/handheld open field (indirect fire) probability of detection for response and discrimination stages versus their respective probability of false positive.

Not covered

Figure 6. PEDEMIS/handheld open field (legacy) probability of detection for response and discrimination stages versus their respective probability of false positive.

Not covered

Figure 7. PEDEMIS/handheld wooded probability of detection for response and discrimination stages versus their respective probability of false positive.

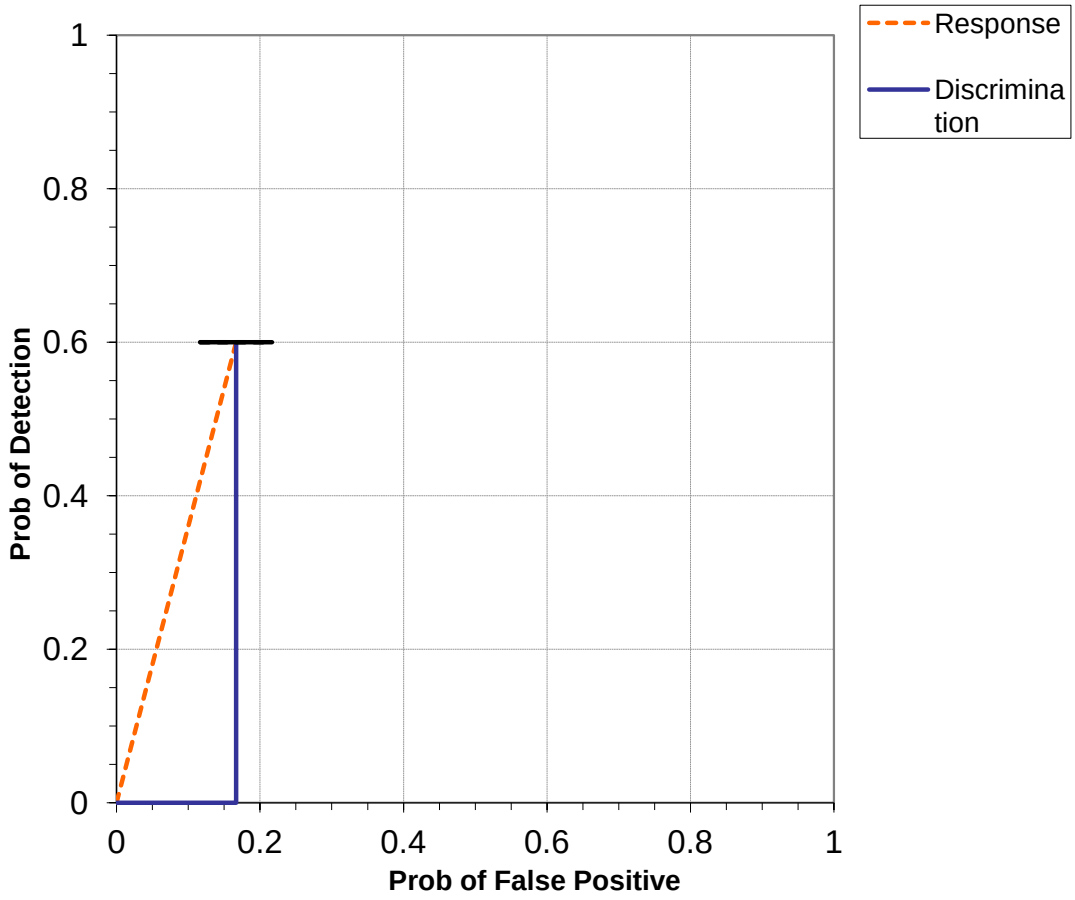

Figure 8. PEDEMIS/handheld mogul probability of detection for response and discrimination stages versus their respective probability of false positive.

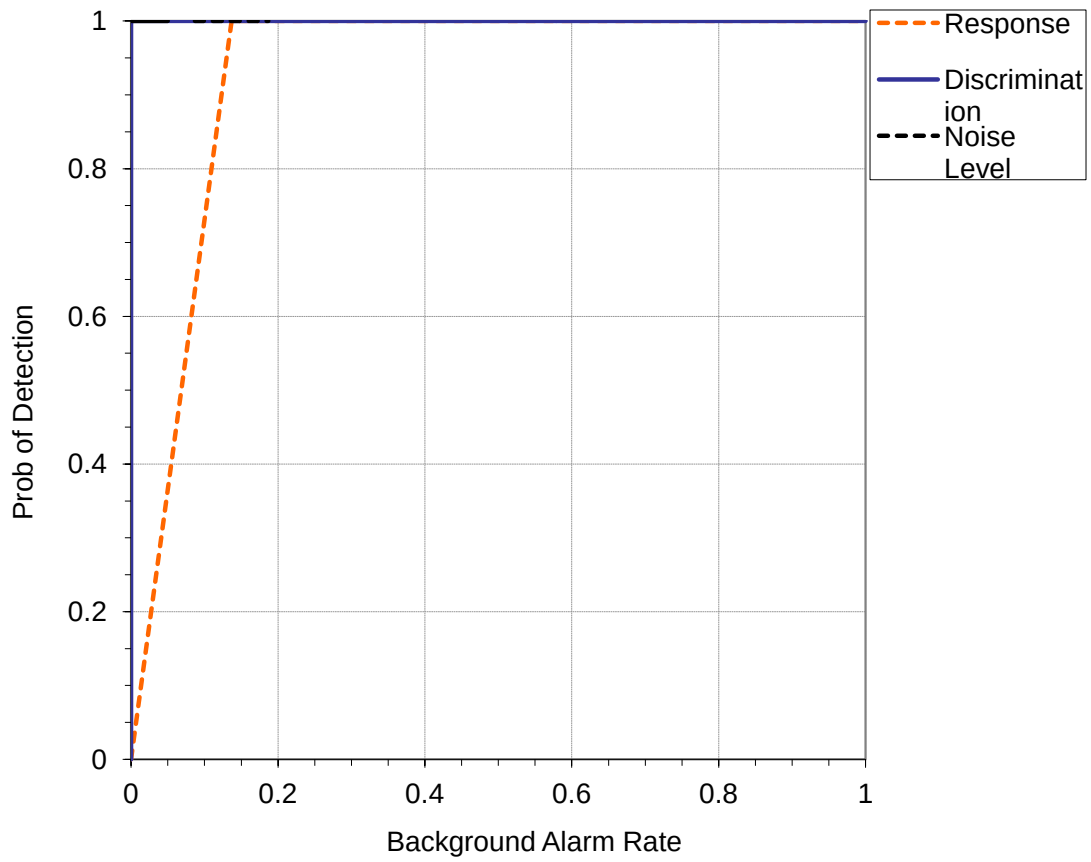

Figure 9. PEDEMIS/handheld blind grid probability of detection for response and discrimination stages versus their respective probability of background alarm.

Not covered

Figure 10. PEDEMIS/handheld open field (direct fire) probability of detection for response and discrimination stages versus their respective background alarm rate.

Not covered

Figure 11. PEDEMIS/handheld open field (indirect fire) probability of detection for response and discrimination stages versus their respective background alarm rate.

Not covered

Figure 12. PEDEMIS/handheld open field (legacy) probability of detection for response and discrimination stages versus their respective background alarm rate.

Not covered

Figure 13. PEDEMIS/handheld wooded probability of detection for response and discrimination stages versus their respective background alarm rate.

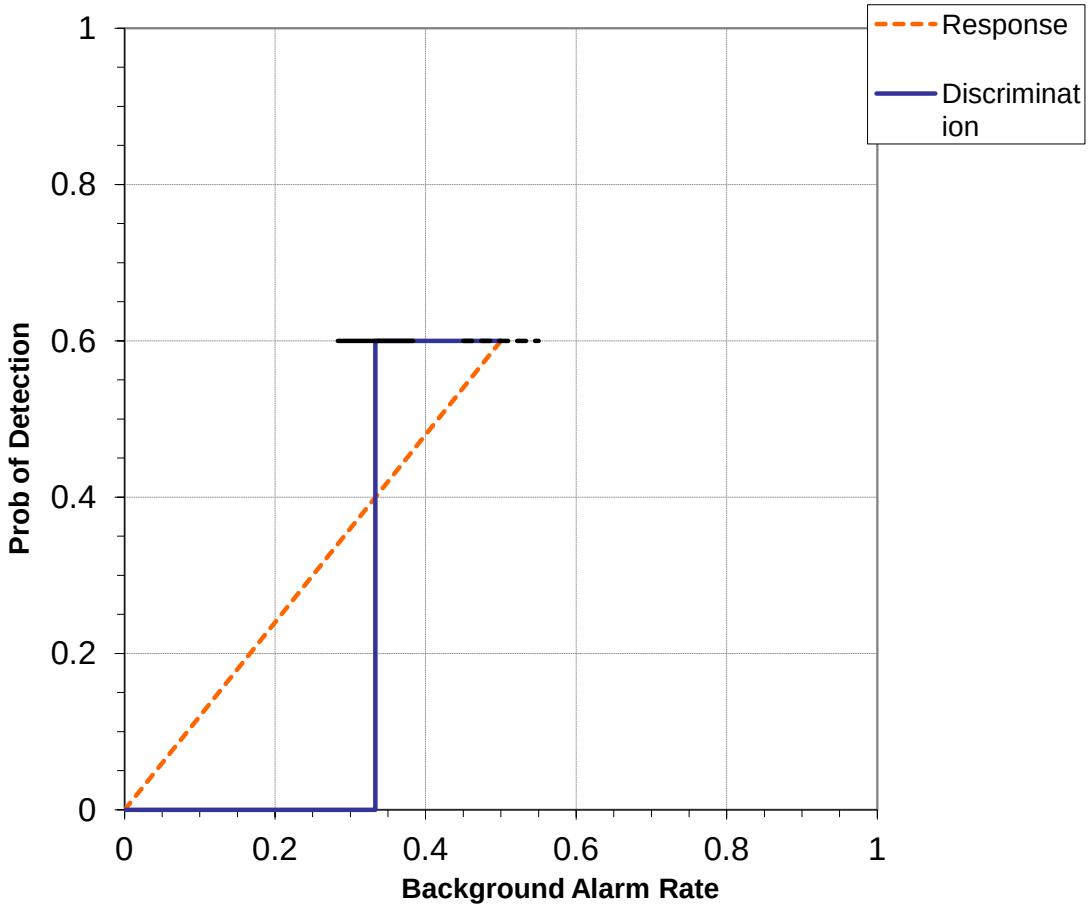

Figure 14. PEDEMIS/handheld mogul probability of detection for response and discrimination stages versus their respective background alarm rate.

4.2 PERFORMANCE SUMMARIES

Results for each of the testing areas are presented in Tables 6 (for labor requirements, see section 5). The response stage results are derived from the list of anomalies above the demonstrator-provided noise level. The results for the discrimination stage are derived from the demonstrator's recommended threshold for optimizing munitions related cleanup by minimizing false alarm digs and maximizing munitions recovery. The lower and upper 90-percent confidence limits on P_d, P_{cd}, and P_{fp} were calculated assuming that the number of detections and false positives are binomially distributed random variables.

TABLE 6a. BLIND GRID TEST AREA RESULTS

	Response Stage				**Discrimination Stage**			
Munitions[a] Scores	**Pd^{res}: by type**				**Pd^{disc}: by type**			
	All Types	**105-mm**	**81/60-mm**	**37/25-mm**	**All Types**	**105-mm**	**81/60-mm**	**37/25-mm**
	1.00 1.00 0.98	1.00 1.00 0.93	1.00 1.00 0.93	1.00 1.00 0.93	1.00 1.00 0.98	1.00 1.00 0.93	1.00 1.00 0.93	1.00 1.00 0.93
0 to 4D	1.00	1.00	1.00	1.00	1.00	1.00	1.00	1.00
4D to 8D	1.00	1.00	1.00	1.00	1.00	1.00	1.00	1.00
8D to 12D	1.00	1.00	1.00	1.00	1.00	1.00	1.00	1.00
Clutter Scores	**P_{cd}**				**P_{fp}**			
By Depth[b]	**All Mass**	**0 to 0.25 kg**	**>0.25 to 1 kg**	**>1 to 8 kg**	**All Mass**	**0 to 0.25 kg**	**>0.25 to 1 kg**	**>1 to 8 kg**
All Depth	0.99 0.98	0.95	1.00	1.00	0.07 0.03	0.00	0.04	0.20
0 to 0.15 m	0.95				0.02			
0.15 to 0.3 m	0.97	0.94	1.00	1.00	0.02	0.00	0.02	0.17
0.3 to 0.6 m	1.00	1.00	1.00	1.00	0.13	0.00	0.14	0.25
Background Alarm Rates								
	P_{ba}^{res}: 0.14				**P_{ba}^{disc}:** 0.00			

[a]In cells with offset data entries, the numbers to the left are the result and the two numbers to the right are an upper and lower 90-percent confidence interval for an assumed binomial distribution.
[b]All depths are measured to the center of the object.

TABLE 6b. OPEN FIELD DIRECT FIRE TEST AREA RESULTS (not covered)

	Response Stage				Discrimination Stage			
Munitions[a] Scores	P_d^{res}: *by type*				P_d^{disc}: *by type*			
	All Types	**105-mm**	**81-mm**	**60-mm**	**All Types**	**105-mm**	**81-mm**	**60-mm**
	-- -- --	-- -- --	-- -- --	-- -- --	-- -- --	-- -- --	-- -- --	-- -- --
By Density								
High	--	--	--	--	--	--	--	--
Medium	--	--	--	--	--	--	--	--
Low	--	--	--	--	--	--	--	--
By Depth[b]								
0 to 4D	--	--	--	--	--	--	--	--
4D to 8D	--	--	--	--	--	--	--	--
8D to 12D	--	--	--	--	--	--	--	--
Clutter Scores	P_{cd}				P_{fp}			
By Mass								
By Depth[b]	**All Mass**	**0 to 0.25 kg**	**>0.25 to 1 kg**	**>1 to 8 kg**	**All Mass**	**0 to 0.25 kg**	**>0.25 to 1 kg**	**>1 to 8 kg**
All Depth	-- -- --	--	--	--	-- -- --	--	--	--
0 to 0.15 m	--	--	--	--	--	--	--	--
0.15 to 0.3 m	--	--	--	--	--	--	--	--
0.3 to 0.6 m	--	--	--	--	--	--	--	--
Background Alarm Rates								
	BAR^{res}: --				**BAR^{disc}: --**			
Groups								
Found	--				--			
Identified	--				--			
Coverage	--				--			

[a]In cells with offset data entries, the numbers to the left are the result and the two numbers to the right are an upper and lower 90-percent confidence interval for an assumed binomial distribution.
[b]All depths are measured to the center of the object.

TABLE 6c. OPEN FIELD INDIRECT FIRE TEST AREA RESULTS (Partial Coverage)

	Response Stage				Discrimination Stage			
Munitions[a] Scores	P_d^{res}: *by type*				P_d^{disc}: *by type*			
	All Types	**105-mm**	**81-mm**	**60-mm**	**All Types**	**105-mm**	**81-mm**	**60-mm**
	-- -- --	-- -- --	-- -- --	-- -- --	-- -- --	-- -- --	-- -- --	-- -- --
By Density								
High	--	--	--	--	--	--	--	--
Medium	--	--	--	--	--	--	--	--
Low	--	--	--	--	--	--	--	--
By Depth[b]								
0 to 4D	--	--	--	--	--	--	--	--
4D to 8D	--	--	--	--	--	--	--	--
8D to 12D	--	--	--	--	--	--	--	--
Clutter Scores	P_{cd}				P_{fp}			
By Mass								
By Depth[b]	**All Mass**	**0 to 0.25 kg**	**>0.25 to 1 kg**	**>1 to 8 kg**	**All Mass**	**0 to 0.25 kg**	**>0.25 to 1 kg**	**>1 to 8 kg**
All Depth	-- -- --	--	--	--	-- -- --	--	--	--
0 to 0.15 m	--	--	--	--	--	--	--	--
0.15 to 0.3 m	--	--	--	--	--	--	--	--
0.3 to 0.6 m	--	--	--	--	--	--	--	--
Background Alarm Rates								
	BAR[res]**:** --				**BAR**[disc]**:** --			
Groups								
Found	--				--			
Identified	--				--			
Coverage	--				--			

[a]In cells with offset data entries, the numbers to the left are the result and the two numbers to the right are an upper and lower 90-percent confidence interval for an assumed binomial distribution.
[b]All depths are measured to the center of the object.

TABLE 6d. OPEN FIELD LEGACY TEST AREA RESULTS (not covered)

	Response Stage				Discrimination Stage			
Munitions[a] Scores	P_d^{res}: *by type*				P_d^{disc}: *by type*			
	All Types	**Small**	**Medium**	**Large**	**All Types**	**Small**	**Medium**	**Large**
	-- -- --	-- -- --	-- -- --	-- -- --	-- -- --	-- -- --	-- -- --	-- -- --
	By Depth[b]							
0 to 4D	--	--	--	--	--	--	--	--
4D to 8D	--	--	--	--	--	--	--	--
8D to 12D	--	--	--	--	--	--	--	--
> 12D	--	--	--	--	--	--	--	--
Clutter Scores	P_{cd}				P_{fp}			
	By Mass							
By Depth[b]	**All Mass**	**0 to 0.25 kg**	**>0.25 to 1 kg**	**>1 to 10 kg**	**> 10 kg**	**All Mass**	**0 to 0.25 kg**	**>0.25 to 1 kg**	**>1 to 8 kg**	**< 10kg**
All Depth	-- -- --	--	--	--	--	-- -- --	--	--	--	--
0 to 0.15 m	--	--	--	--	--	--	--	--	--	--
0.15 to 0.3 m	--	--	--	--	--	--	--	--	--	--
0.3 to 0.6 m	--	--	--	--	--	--	--	--	--	--
> 0.6 m	--	--	--	--	--	--	--	--	--	--
	Background Alarm Rates									
	BAR[res]**:**				**BAR**[disc]**:**					
	Groups									
Found	--				--					
Identified	--				--					
Coverage	--				--					

[a]The two numbers to the right of the all types munitions result are an upper and lower 90-percent confidence interval for an assumed binomial distribution.
[b]All depths are measured to the center of the object.

TABLE 6e. WOODED TEST AREA RESULTS (not covered)

	Response Stage				Discrimination Stage			
Munitions[a] Scores	P_d^{res}: *by type*				P_d^{disc}: *by type*			
	All Types	**Small**	**Medium**	**Large**	**All Types**	**Small**	**Medium**	**Large**
	-- -- --	-- -- --	-- -- --	-- -- --	-- -- --	-- -- --	-- -- --	-- -- --
	By Depth[b]							
0 to 4D	--	--	--	--	--	--	--	--
4D to 8D	--	--	--	--	--	--	--	--
8D to 12D	--	--	--	--	--	--	--	--
> 12D	--	--	--	--	--	--	--	--
Clutter Scores	P_{cd}				P_{fp}			
	By Mass							
By Depth[b]	**All Mass**	**0 to 0.25 kg**	**>0.25 to 1 kg**	**>1 to 10 kg**	**> 10 kg**	**All Mass**	**0 to 0.25 kg**	**>0.25 to 1 kg**	**>1 to 8 kg**	**< 10kg**
All Depth	-- -- --	--	--	--	--	-- -- --	--	--	--	--
0 to 0.15 m	--	--	--	--	--	--	--	--	--	--
0.15 to 0.3 m	--	--	--	--	--	--	--	--	--	--
0.3 to 0.6 m	--	--	--	--	--	--	--	--	--	--
> 0.6 m	--	--	--	--	--	--	--	--	--	--
	Background Alarm Rates									
	BAR[res]**:**				**BAR**[disc]**:**					
	Groups									
Found	--				--					
Identified	--				--					
Coverage	--				--					

[a]The two numbers to the right of the all types munitions result are an upper and lower 90-percent confidence interval for an assumed binomial distribution.
[b]All depths are measured to the center of the object.

TABLE 6f. MOGUL TEST AREA RESULTS (not covered)

	Response Stage				Discrimination Stage			
Munitions[a] Scores	P_d^{res}: *by type*				P_d^{disc}: *by type*			
	All Types	**Small**	**Medium**	**Large**	**All Types**	**Small**	**Medium**	**Large**
	-- -- --	-- -- --	-- -- --	-- -- --	-- -- --	-- -- --	-- -- --	-- -- --
	By Depth[b]							
0 to 4D	--	--	--	--	--	--	--	--
4D to 8D	--	--	--	--	--	--	--	--
8D to 12D	--	--	--	--	--	--	--	--
> 12D	--	--	--	--	--	--	--	--
Clutter Scores	P_{cd}				P_{fp}			
	By Mass							
By Depth[b]	**All Mass**	**0 to 0.25 kg**	**>0.25 to 1 kg**	**>1 to 10 kg**	**> 10 kg**	**All Mass**	**0 to 0.25 kg**	**>0.25 to 1 kg**	**>1 to 8 kg**	**< 10kg**
All Depth	-- -- --	--	--	--	--	-- -- --	--	--	--	--
0 to 0.15 m	--	--	--	--	--	--	--	--	--	--
0.15 to 0.3 m	--	--	--	--	--	--	--	--	--	--
0.3 to 0.6 m	--	--	--	--	--	--	--	--	--	--
> 0.6 m	--	--	--	--	--	--	--	--	--	--
	Background Alarm Rates									
	BAR^{res}:				**BAR**^{disc}:					
	Groups									
Found	--				--					
Identified	--				--					
Coverage	--				--					

[a]The two numbers to the right of the all types munitions result are an upper and lower 90-percent confidence interval for an assumed binomial distribution.
[b]All depths are measured to the center of the object.

4.3 EFFICIENCY, REJECTION RATES, AND TYPE CLASSIFICATION

Efficiency and rejection rates are calculated to quantify the discrimination ability at specific points of interest on the ROC curve: (1) at the point where no decrease in P_d is suffered (i.e., the efficiency is by definition equal to one) and (2) at the operator selected threshold. These values are presented in Tables 7a through 7d.

TABLE 7a. BLIND GRID EFFICIENCY AND REJECTION RATES

	Efficiency (E)	False Positive Rejection Rate	Background Alarm Rejection Rate
At Operating Point	1.00	0.97	1.00
With No Loss of P_d	1.00	0.99	1.00

TABLE 7b. OPEN FIELD (DIRECT) EFFICIENCY AND REJECTION RATES (not covered)

	Efficiency (E)	False Positive Rejection Rate	Background Alarm Rejection Rate
At Operating Point	--	--	--
With No Loss of P_d	--	--	--

TABLE 7c. OPEN FIELD (INDIRECT) EFFICIENCY AND REJECTION RATES (Partial Coverage)

	Efficiency (E)	False Positive Rejection Rate	Background Alarm Rejection Rate
At Operating Point	NA	0.647	0.727
With No Loss of P_d	1.00	1.00	1.00

TABLE 7d. OPEN FIELD (LEGACY) EFFICIENCY AND REJECTION RATES (not covered)

	Efficiency (E)	False Positive Rejection Rate	Background Alarm Rejection Rate
At Operating Point	--	--	--
With No Loss of P_d	--	--	--

TABLE 7e. WOODED EFFICIENCY AND REJECTION RATES (not covered)

	Efficiency (E)	False Positive Rejection Rate	Background Alarm Rejection Rate
At Operating Point	--	--	--
With No Loss of P_d	--	--	--

TABLE 7f. MOGUL EFFICIENCY AND REJECTION RATES (Partial Coverage)

	Efficiency (E)	False Positive Rejection Rate	Background Alarm Rejection Rate
At Operating Point	1.0	0	.334
With No Loss of P_d	1.0	0	.333

At the demonstrator's recommended setting, the munitions items that were detected and correctly discriminated were further scored on whether their correct type could be identified (table 8a through 8f). Correct type examples include 20-mm projectile, 105-mm HEAT projectile, and 2.75-inch Rocket. A list of the standard type declaration required for each munitions item was provided to demonstrators prior to testing. The standard types for the three example items are 20-mmP, 105H, and 2.75-inch.

TABLE 8a. BLIND GRID CORRECT TYPE CLASSIFICATION OF TARGETS CORRECTLY DISCRIMINATED AS MUNITIONS

Size	Percentage Correct
25mm	100%
37mm	100%
60mm	100%
81mm	80%
105mm	7%
105 artillery	13%
Overall	67%

Note: The demonstrator did not attempt to provide type classification (if applicable).

TABLE 8b. OPEN FIELD DIRECT FIRE CORRECT TYPE CLASSIFICATION OF TARGETS CORRECTLY DISCRIMINATED AS MUNITIONS (not covered)

Size	Percentage Correct
25mm	--
37mm	--
105mm	--
Overall	--

TABLE 8c. OPEN FIELD INDIRECT FIRE CORRECT TYPE CLASSIFICATION OF TARGETS CORRECTLY DISCRIMINATED AS MUNITIONS (not covered)

Size	Percentage Correct
60mm	NA
81mm	NA
105mm	NA
Overall	NA

TABLE 8d. OPEN FIELD LEGACY CORRECT TYPE CLASSIFICATION OF TARGETS CORRECTLY DISCRIMINATED AS MUNITIONS (not covered)

Size	Percentage Correct
Small	--
Medium	--
Large	--
Overall	--

TABLE 8e. WOODED CORRECT TYPE CLASSIFICATION OF TARGETS CORRECTLY DISCRIMINATED AS MUNITIONS (not covered)

Size	Percentage Correct
Small	--
Medium	--
Large	--
Overall	--

TABLE 8f. MOGUL CORRECT TYPE CLASSIFICATION OF TARGETS CORRECTLY DISCRIMINATED AS MUNITIONS (not covered)

Size	Percentage Correct
Small	(3 of 4) .75
Medium	(0 of 1)0
Large	NA
Overall	.60

4.4 LOCATION ACCURACY

The mean location error and standard deviations appear in Tables 9a through 9f. These calculations are based on average missed distance for munitions correctly identified during the response stage. Depths are measured from the center of the munitions to the surface. For the blind grid, only depth errors are calculated because (X, Y) positions are known to be the centers of the grid square.

TABLE 9a. BLIND GRID MEAN LOCATION ERROR AND STANDARD DEVIATION

	Mean	Standard Deviation
Northing	N/A	N/A
Easting	N/A	N/A
Depth	0.072	0.063

TABLE 9b. OPEN FIELD DIRECT FIRE MEAN LOCATION ERROR AND STANDARD DEVIATION (not covered)

	Mean	Standard Deviation
Northing	N/A	N/A
Easting	N/A	N/A
Depth	N/A	N/A

TABLE 9c. OPEN FIELD INDIRECT FIRE MEAN LOCATION ERROR AND STANDARD DEVIATION (not covered)

	Mean	Standard Deviation
Northing	NA	NA
Easting	NA	NA
Depth	NA	NA

TABLE 9d. OPEN FIELD LEGACY MEAN LOCATION ERROR AND STANDARD DEVIATION (not covered)

	Mean	Standard Deviation
Northing	--	--
Easting	--	--
Depth	--	--

TABLE 9e. WOODED MEAN LOCATION ERROR AND STANDARD DEVIATION (not covered)

	Mean	Standard Deviation
Northing	--	--
Easting	--	--
Depth	--	--

TABLE 9f. MOGUL MEAN LOCATION ERROR AND STANDARD DEVIATION (Partial Coverage)

	Mean	Standard Deviation
Northing	0.154	0.154
Easting	0.168	0.101
Depth	0.078	0.021

D Outbrief Slides

Bistatic Portable Electromagnetic Induction Sensor with Integrated Positioning

MR-1712

Benjamin Barrowes
USACE-ERDC-CRREL

SERDP Project Outbrief

May 7, 2012

SERDP
DOD • EPA • DOE

Project Team

- **Dr. Benjamin Barrowes**
  - USACE-ERDC-CRREL, **Principal Investigator**
  - Specialist in electromagnetic phenomenology and computation
- **Dr. Kevin O'Neill**
  - USACE-ERDC-CRREL
  - Electromagnetic phenomenology and signal processing expert
- **Dr. Fridon Shubitidze**
  - Dartmouth College
  - Specialist in electromagnetics, modeling & discrimination processing
- **David George**
  - G&G Sciences
  - Engineering and electronics expertise

Background – MR1712 (FY10-FY12)

- Many contaminated sites consist of non-cart-trafficable terrain
- Flexibility needed for varying circumstances (deep, dispersed, multitarget)
- Real-time feedback is needed for decisions in the field
- Positioning of receivers is critical to discrimination
- High fidelity multistatic instrument needed to utilize the capabilities of advanced models
- Need an instrument that can interrogate obstructed anomalies (e.g. vegetation, rocks)
- One pass solution is desired for surveying and interrogation

Technical Objective

Pedemis – PortablE Decoupled ElectroMagnetic Induction Sensor

- Multimodal, physically decoupled EMI sensor
- Advanced models (JD, ONVMS, MUSIC) and data collection schemes to take advantage of the new instrument's flexibility and multistatic design
- Portable EMI instrument for benign and challenging terrain
- Lightweight, power efficient, portable
- Efficient DAQ protocols
- Combines advantages of carted and handheld sensors

Pedemis Advantages

Pedemis – PortablE Decoupled ElectroMagnetic Induction Sensor

- Potential one pass solution
- Hardware
  - 2-person portable design
  - Flexible (2-person portable, carted, sledded)
  - 1.2x1.2m, 3x3 Tx, 3x3 vector Rx (compromise between 2 and 5)
  - decoupled Rx (data diversity, spatial coverage)
  - Lighter, updated electronics
  - Integral positioning system
  - GPS and digital compass
  - Wide swath width and spatial coverage
- Software and processing
  - Real-time feedback to expert operators (field plots, arrows, and JD)
  - Data suited to advanced models (JD, ONVMS, MUSIC)
  - Flexible DAQ modes (detection, interrogation, deep detection, wide interrogation)
  - EM3D or LabVIEW interface

Pedemis Transmitter and Receiver Assemblies

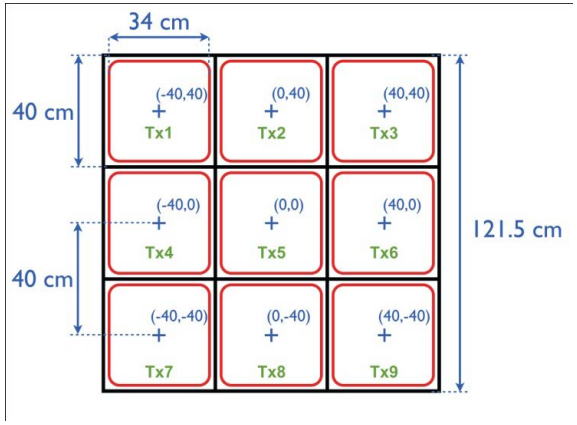

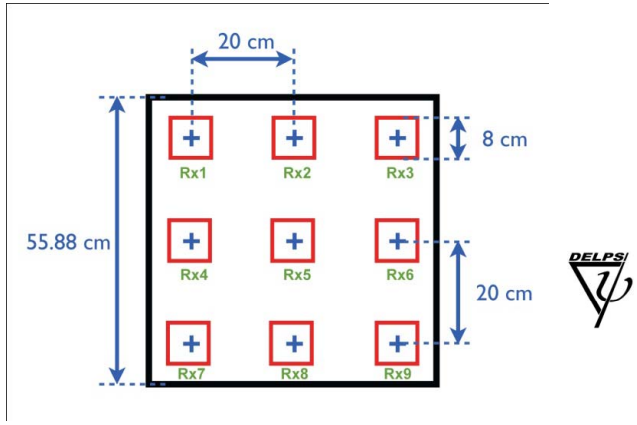

- Tradeoffs:
  - Data diversity
  - Portability (weight and size)
  - Accompanying hardware
  - Multitarget discrimination
- 1.2m x 1.2m Tx array
- TEMTADS size transmitters
- 30 lbs weight
- Transmitters fire in sequence

- 3 x 3 vector receiver array
- 9 x 9 x 3 data channels per shot
- 5 shots (center and corners) in static mode
- 8cm Rx cubes (MPV2 balsa type)
- 12cm between cubes => 48cm total
- 1-4 minute DAQ time
- Lightweight (~7 pounds)
- Selectable DAQ parameters

Pedemis Backpack Electronics

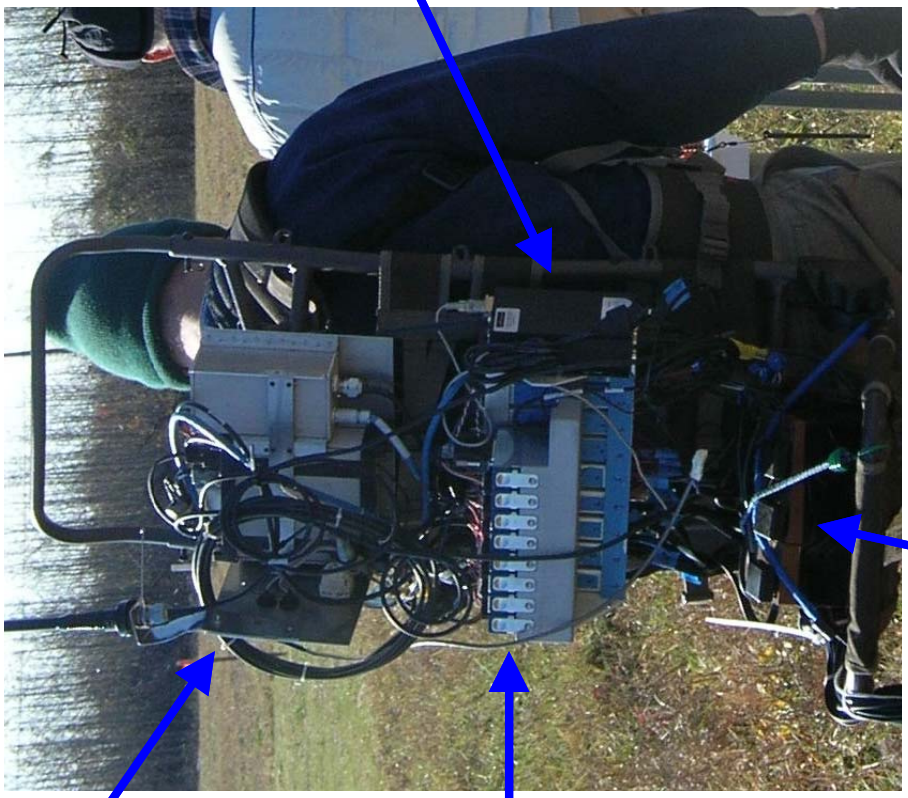

NI – cRIO DAQ Chassis
- 8 module slots: 1 DIO module, 7 DAQ modules
- Web interface
- Lightweight and rugged
- EM3D software or LabVIEW
- Reduced power consumption
- ~7 pounds
- Tx module
- Filter module

Pedemis Positioning

- Position of Rx required to collectively utilize multiple data shots
- Positioning accomplished via Rx "on-time" measurements of Tx primary field (DAQ during Tx "off-time"), no additional hardware
- Similar to MPV2 positioning but without external cubes
- Rx can be placed outside of Tx's
- All Tx's and Rx's potentially used in positioning (via postprocessing)

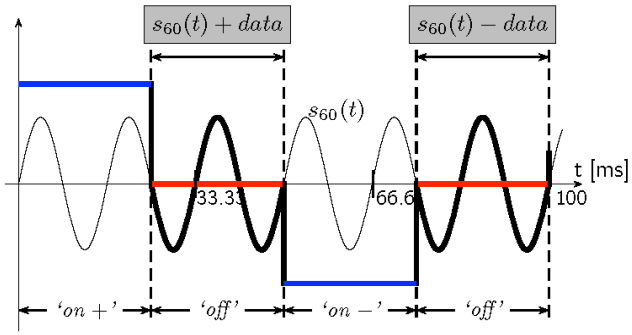

Pedemis Positioning - II

Positioning via mutual inductance

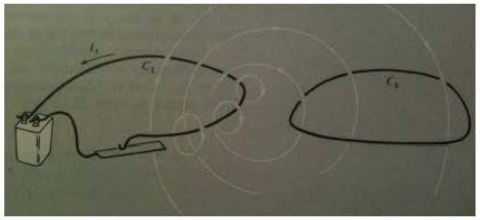

- The *mutual inductance* of two coils contains all the geometric information we seek:

$$M_{12} = \frac{\Phi_1}{i_2} = \frac{\mu_0}{4\pi} \oint\oint \frac{d\mathbf{l}_1 \cdot d\mathbf{l}_2}{|\mathbf{r}_1 - \mathbf{r}_2|} = \frac{\Phi_2}{i_1} = M_{21}$$

- There is a closed expression for M of two parallel filaments
  - Can be extended to squares
  - Only elementary functions
  - No risk of divergence
- The integration is done implicitly at full accuracy
  - No need to keep track of the number of integration points

Pedemis Operation

- Protocols developed at APG at first demo
- Can also be used in traditional mode (survey, then cued)
- Plan to automate for nonexpert users

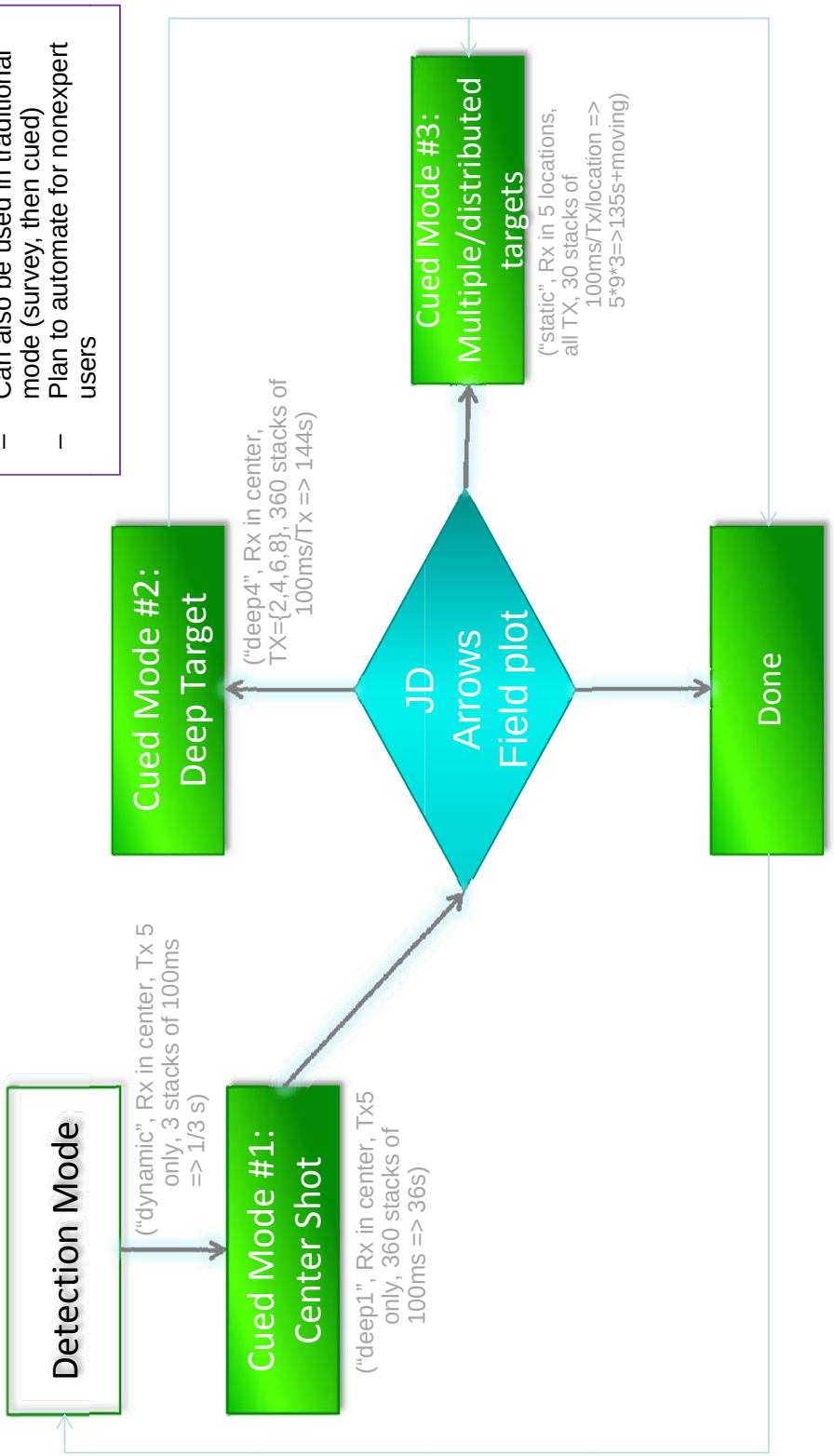

Detection Mode

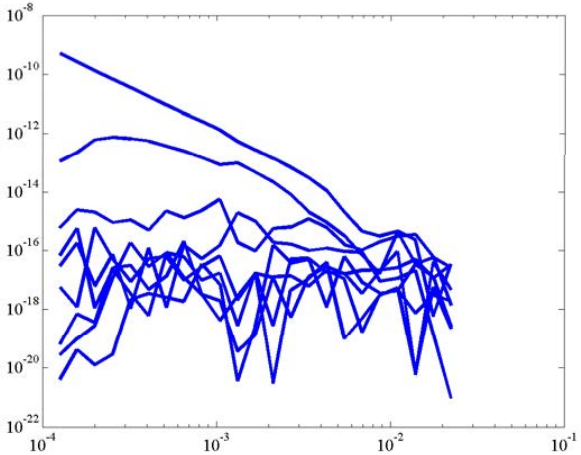

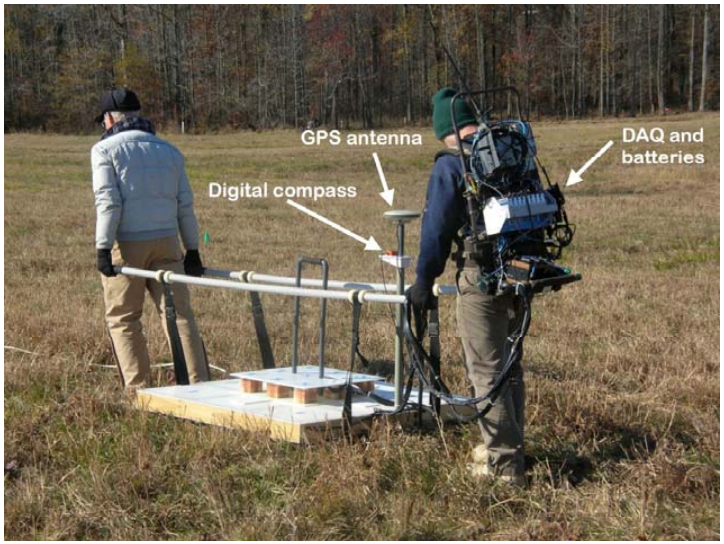

- Real-time feedback may allow immediate reduction in cued interrogations
- Wide coverage
- Spatially diverse data for models
- Single person sled possible

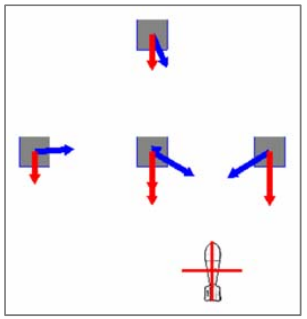

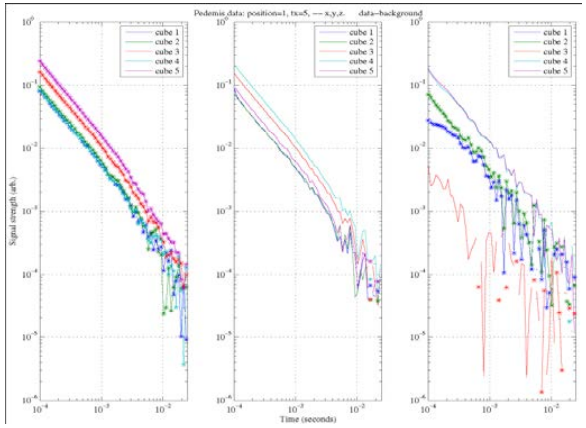

Cued Interrogation Modes

Cued #1 – "deep1"

- Pedemis set on ground
- Typical first cued interrogation
- Rx array left stationary in center
- 36 sec DAQ time

Cued #2 – "deep4"

- Tx={2,4,6,8}
- Data combined with deep1 later
- Rx array left stationary in center
- 144 sec DAQ time

Cued #3 – "static"

- Move Rx 5 times
- For multiple and/or widespread targets
- 135 sec DAQ time
- Around 12dB lower SNR

Pedemis Software and Analysis

- EM3D – DAQ control
- Joint Diagonalization – dynamic and cued#1 modes, real time
- ONVMS (orthonormalized volume magnetic source) – expert post analysis
- Rx positioning – post processing

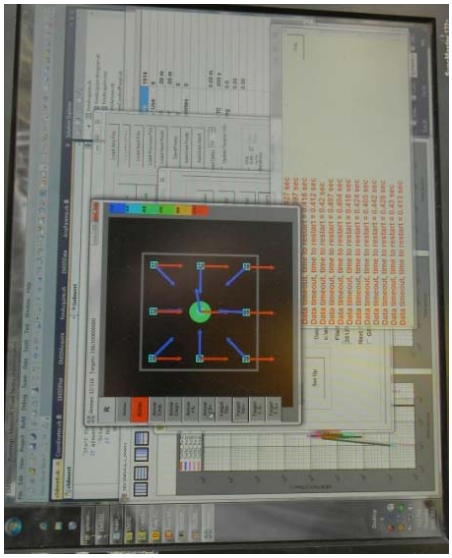

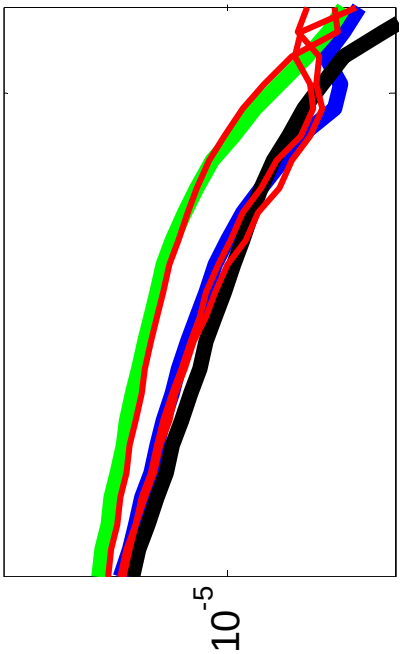

APG Results

Areas Visited

- Partial IDF area
- Partial mogul area
- Blind grid (400 cells)

DAQ Parameters

- 25ms decay
- 25 time gates
- Dynamic, deep1, deep4, and static modes

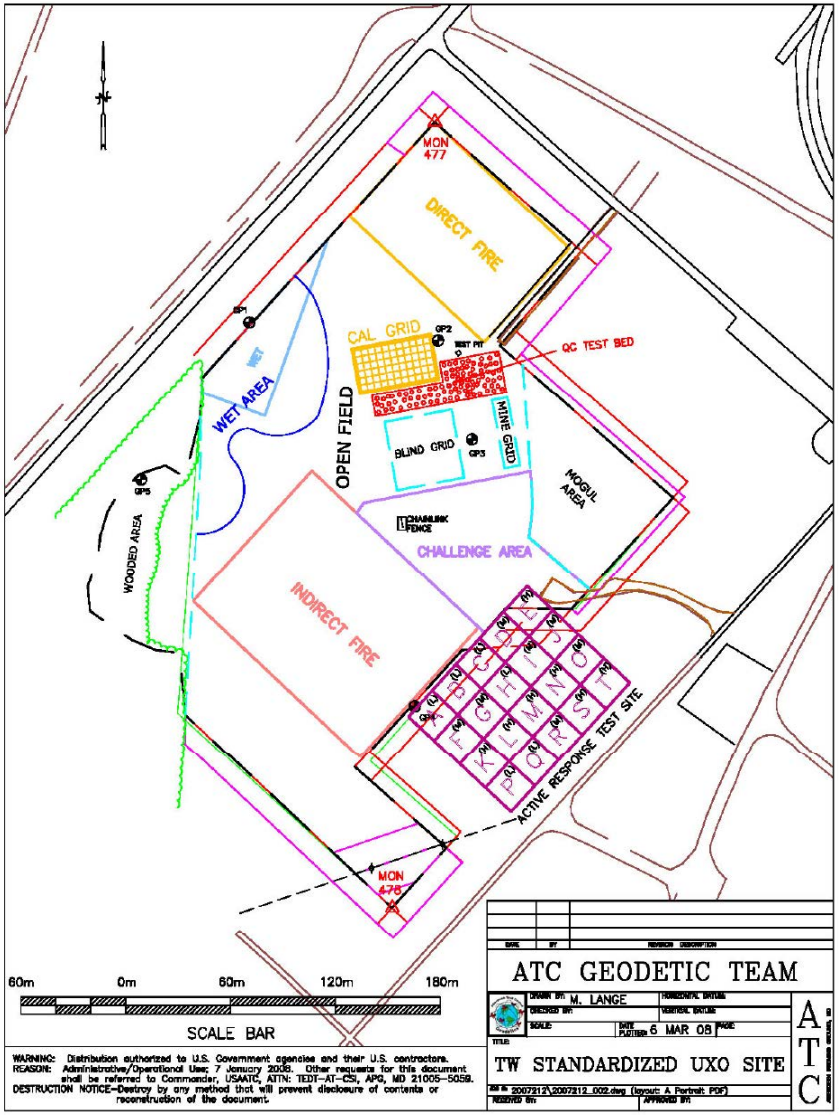

APG Results: Blind Grid

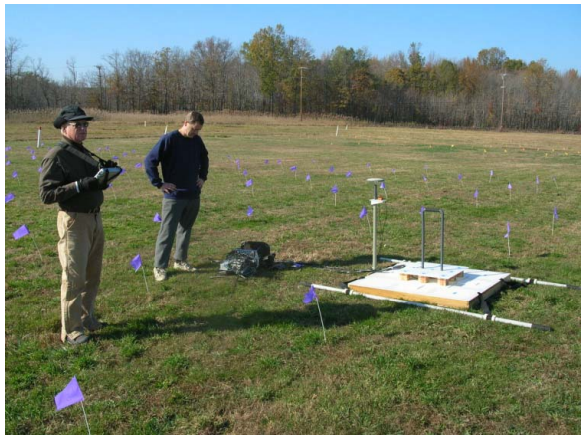

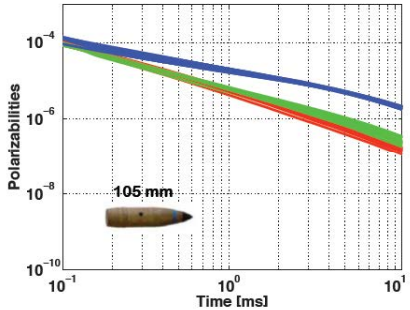

(a) 105 mm projectile.

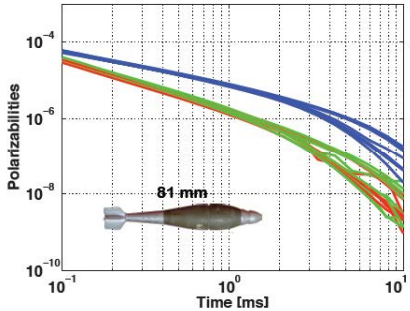

(b) 81 mm projectile.

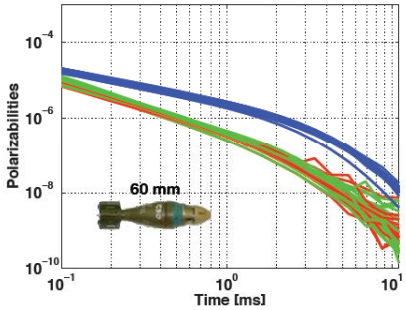

(c) 60 mm projectile.

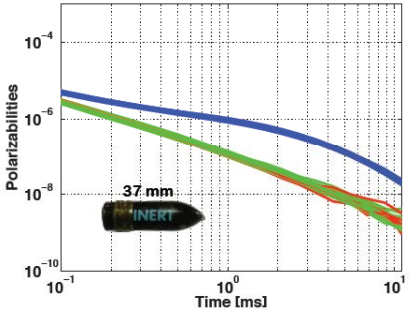

(d) 37 mm projectile.

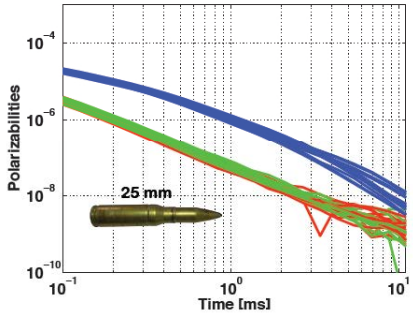

Three Stages

- Detection (or response) stage (something there or not)
- Discrimination stage (UXO or clutter)
- Classification Stage (which type of UXO)

APG Results: Blind Grid – Detection Stage

- Detection stage – found all UXO, found all official clutter except 3, "found" 29 extra pieces of clutter

Response Stage				
Munitions[a] Scores	Pd^{res}: by type			
	All Types	105-mm	81/60-mm	37/25-mm
	1.00 1.00 0.98	1.00 1.00 0.93	1.00 1.00 0.93	1.00 1.00 0.93
0 to 4D	1.00	1.00	1.00	1.00
4D to 8D	1.00	1.00	1.00	1.00
8D to 12D	1.00	1.00	1.00	1.00
Clutter Scores	P_{cd}			
By Depth[b]	**All Mass**	**0 to 0.25 kg**	**>0.25 to 1 kg**	**>1 to 8 kg**
All Depth	0.99 0.98	0.95	1.00	1.00
0 to 0.15 m	0.95			
0.15 to 0.3 m	0.97	0.94	1.00	1.00
0.3 to 0.6 m	1.00	1.00	1.00	1.00
				Background Alarm Rat
	P_{ba}^{res}: 0.14			

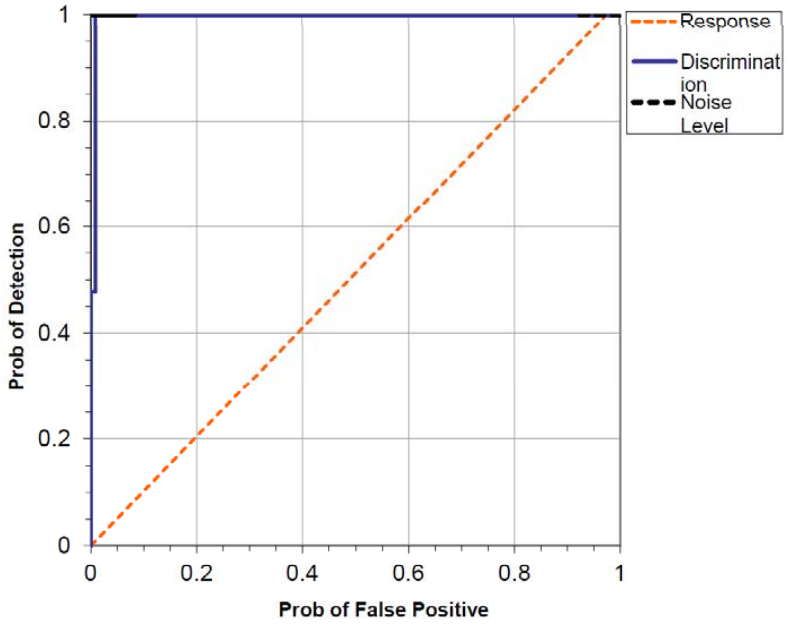

APG Results: Blind Grid – Discrimination Stage

Discrimination stage –
- discriminated all UXO with 4 false positives

TABLE 7a. BLIND GRID EFFICIENCY AND REJECTION RATES

	Efficiency (E)	False Positive Rejection Rate	Background Alarm Rejection Rate
At Operating Point	1.00	0.97	1.00
With No Loss of P_d	1.00	0.99	1.00

	Response Stage				Discrimination Stage			
Munitions[a] Scores	Pd^{res}: by type				Pd^{disc}: by type			
	All Types	105-mm	81/60-mm	37/25-mm	All Types	105-mm	81/60-mm	37/25-mm
	1.00 1.00 0.98	1.00 1.00 0.93	1.00 1.00 0.93	1.00 1.00 0.93	1.00 1.00 0.98	1.00 1.00 0.93	1.00 1.00 0.93	1.00 1.00 0.93
0 to 4D	1.00	1.00	1.00	1.00	1.00	1.00	1.00	1.00
4D to 8D	1.00	1.00	1.00	1.00	1.00	1.00	1.00	1.00
8D to 12D	1.00	1.00	1.00	1.00	1.00	1.00	1.00	1.00
Clutter Scores	P_{cd}				P_{fp}			
By Depth[b]	All Mass	0 to 0.25 kg	>0.25 to 1 kg	>1 to 8 kg	All Mass	0 to 0.25 kg	>0.25 to 1 kg	>1 to 8 kg
All Depth	0.99 0.98	0.95	1.00	1.00	0.07 0.03	0.00	0.04	0.20
0 to 0.15 m	0.95				0.02			
0.15 to 0.3 m	0.97	0.94	1.00	1.00	0.02	0.00	0.02	0.17
0.3 to 0.6 m	1.00	1.00	1.00	1.00	0.13	0.00	0.14	0.25
Background Alarm Rates								
	P_{ba}^{res}: 0.14				P_{ba}^{disc}: 0.00			

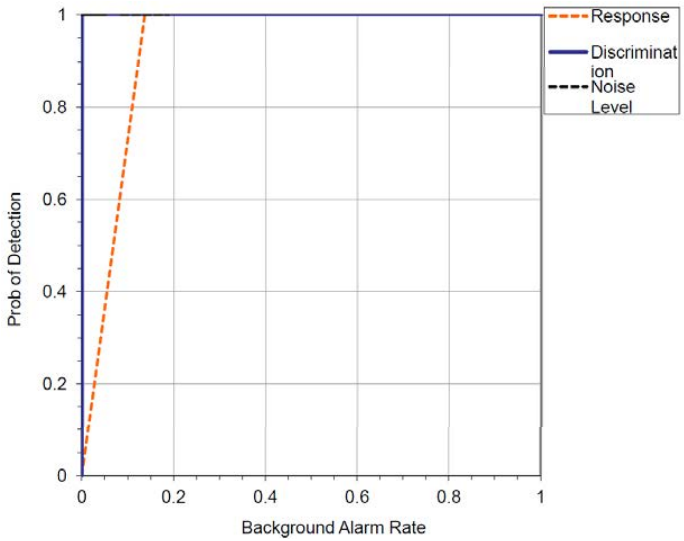

APG Results: Blind Grid – Classification Stage

- Classification Stage – misclassified two 81mm's and (maybe) a few 105mm's

TABLE 8a. BLIND GRID CORRECT TYPE CLASSIFICATION OF TARGETS CORRECTLY DISCRIMINATED AS MUNITIONS

Size	Percentage Correct
25mm	100%
37mm	100%
60mm	100%
81mm	80%
105mm	7%
105 artillery	13%
Overall	67%

TABLE 9a. BLIND GRID MEAN LOCATION ERROR AND STANDARD DEVIATION

	Mean	Standard Deviation
Northing	N/A	N/A
Easting	N/A	N/A
Depth	0.072	0.063

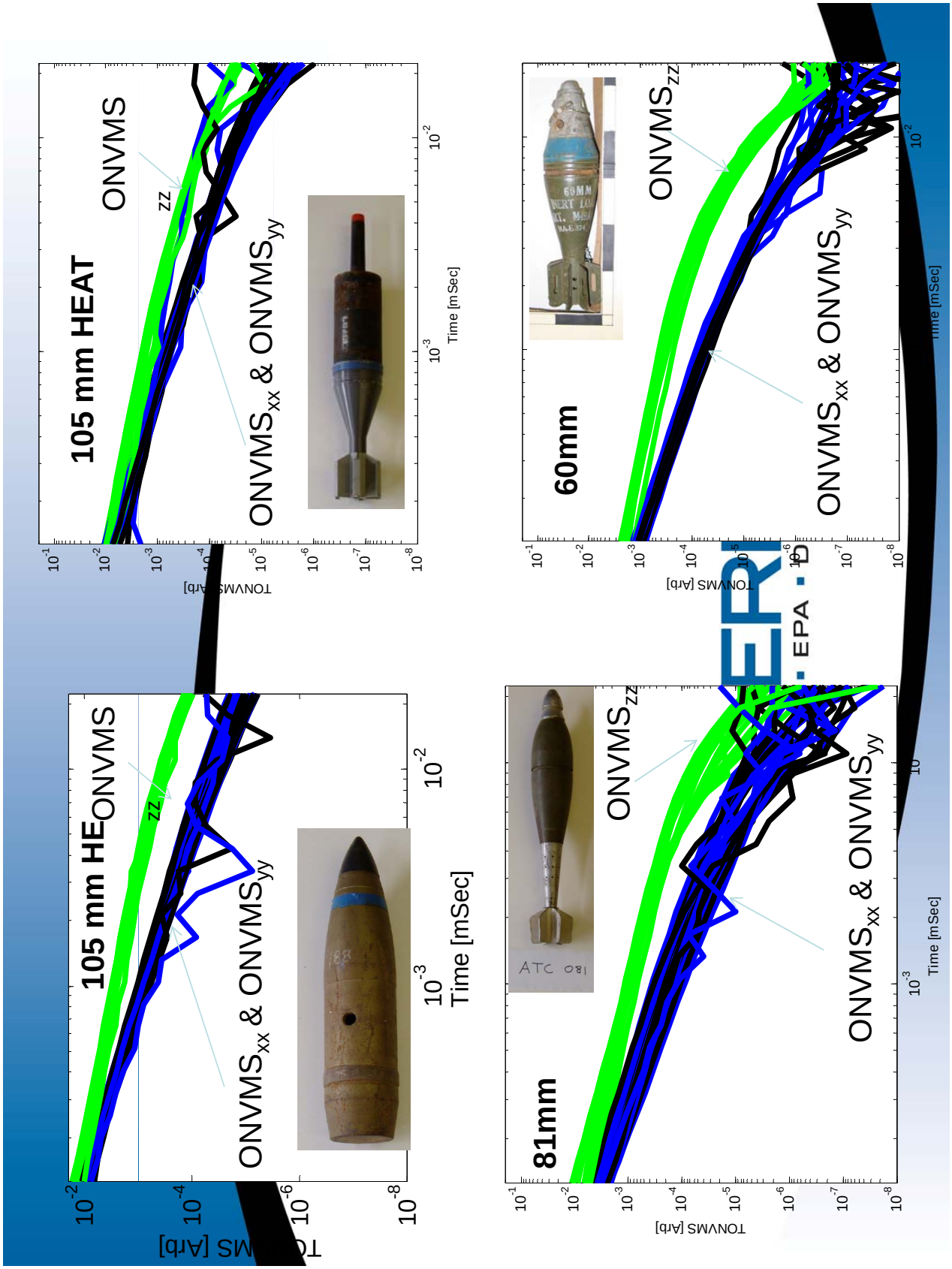
105 mm HEAT
ONVMS
zz
ONVMS$_{xx}$ & ONVMS$_{yy}$
Time [mSec]
60mm
ONVMS$_{zz}$
ONVMS$_{xx}$ & ONVMS$_{yy}$
105 mm HE
ONVMS
zz
ONVMS$_{xx}$ & ONVMS$_{yy}$
Time [mSec]
81mm
ONVMS$_{zz}$
ONVMS$_{xx}$ & ONVMS$_{yy}$
Time [mSec]
TONVMS [Arb]
EPA · D

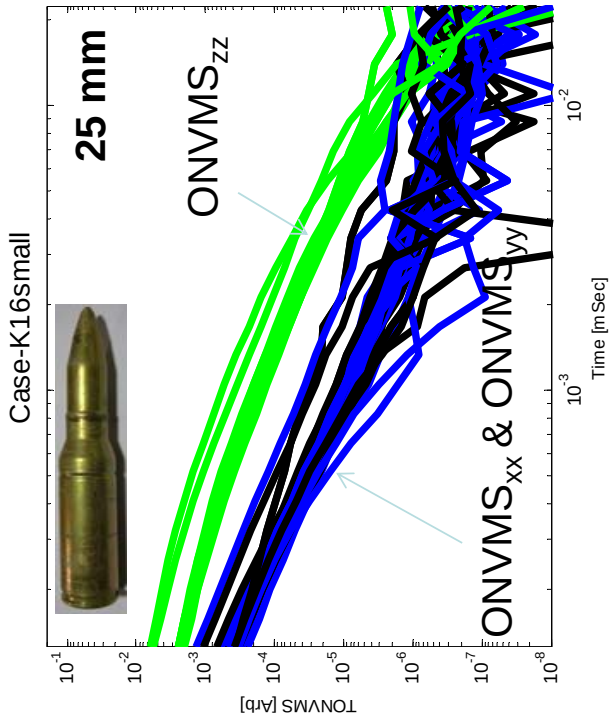
Case-K16small
25 mm
ONVMS$_{zz}$
ONVMS$_{xx}$ & ONVMS$_{yy}$
TONVMS [Arb]
Time [mSec]

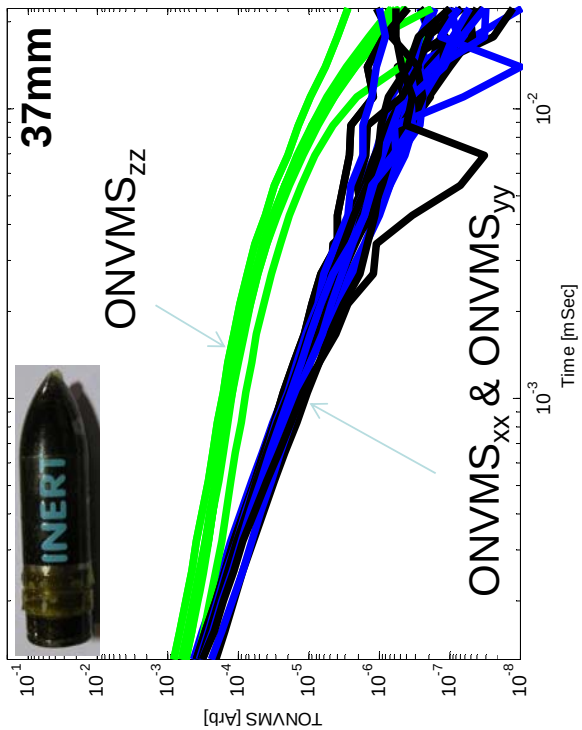
37mm
INERT
ONVMS$_{zz}$
ONVMS$_{xx}$ & ONVMS$_{yy}$
TONVMS [Arb]
Time [mSec]

APG Results: Blind Grid – Comparison

	Response Stage				Discrimination Stage			
Munitions[a] Scores	Pd^{res}: by type				Pd^{disc}: by type			
	All Types	105-mm	81/60-mm	37/25-mm	All Types	105-mm	81/60-mm	37/25-mm
	1.00 1.00 0.98	1.00 1.00 0.93	1.00 1.00 0.93	1.00 1.00 0.93	1.00 1.00 0.98	1.00 1.00 0.93	1.00 1.00 0.93	1.00 1.00 0.93
0 to 4D	1.00	1.00	1.00	1.00	1.00	1.00	1.00	1.00
4D to 8D	1.00	1.00	1.00	1.00	1.00	1.00	1.00	1.00
8D to 12D	1.00	1.00	1.00	1.00	1.00	1.00	1.00	1.00
Clutter Scores	P_{cd}				P_{fp}			
By Depth[b]	All Mass	0 to 0.25 kg	>0.25 to 1 kg	>1 to 8 kg	All Mass	0 to 0.25 kg	>0.25 to 1 kg	>1 to 8 kg
All Depth	0.99 0.98	0.95	1.00	1.00	0.07 0.03	0.00	0.04	0.20
0 to 0.15 m	0.95				0.02			
0.15 to 0.3 m	0.97	0.94	1.00	1.00	0.02	0.00	0.02	0.17
0.3 to 0.6 m	1.00	1.00	1.00	1.00	0.13	0.00	0.14	0.25
Background Alarm Rates								
	P_{ba}^{res}: 0.14				P_{ba}^{disc}: 0.00			

Pedemis APG Results

- MM faster (only 8ms of data, 20s per shot)
- Pedemis more spatial diversity
- ONVMS, JD, MUSIC on Pedemis
- Discrimination based on dynamic data can speed up Pedemis
- Can pick out more targets than MM or 2x2TEMTADS
- Pedemis can deploy to more challenging sites
- MM found 15 more pieces of clutter, missed 2 shallow UXO

MetalMapper APG Results

	Response Stage				Discrimination Stage			
Munitions[a] Scores	P_d^{res}: *by type*				P_d^{disc}: *by type*			
	All Types	105-mm	81/60-mm	37/25-mm	All Types	105-mm	81/60-mm	37/25-mm
	1.00 1.00 0.98	1.00 1.00 0.93	1.00 1.00 0.93	1.00 1.00 0.93	0.99 0.98 0.94	0.98 0.93 0.83	1.00 1.00 0.93	1.00 1.00 0.93
By Depth[b]								
0 to 4D	1.00	1.00	1.00	1.00	0.96	1.00	0.92	1.00
4D to 8D	1.00	1.00	1.00	1.00	1.00	1.00	1.00	1.00
8D to 12D	1.00	1.00	1.00	1.00	1.00	1.00	1.00	1.00
Clutter Scores	P_{cd}				P_{fp}			
By Mass								
By Depth[b]	All Mass	0 to 0.25 kg	>0.25 to 1 kg	>1 to 8 kg	All Mass	0 to 0.25 kg	>0.25 to 1 kg	>1 to 8 kg
All Depth	0.97 0.95 0.91	0.90	1.00	1.00	0.03 0.01 0.00	0.00	0.00	0.10
0 to 0.15 m	0.96	0.93	1.00	1.00	0.01	0.00	0.00	0.17
0.15 to 0.3 m	0.88	0.60	1.00	1.00	0.00	0.00	0.00	0.00
0.3 to 0.6 m	N/A	N/A	N/A	N/A	N/A	N/A	N/A	N/A
Background Alarm Rates								
	P_{ba}^{res}: 0.21				P_{ba}^{disc}: 0.02			

APG Results: Blind Grid – Deep Targets

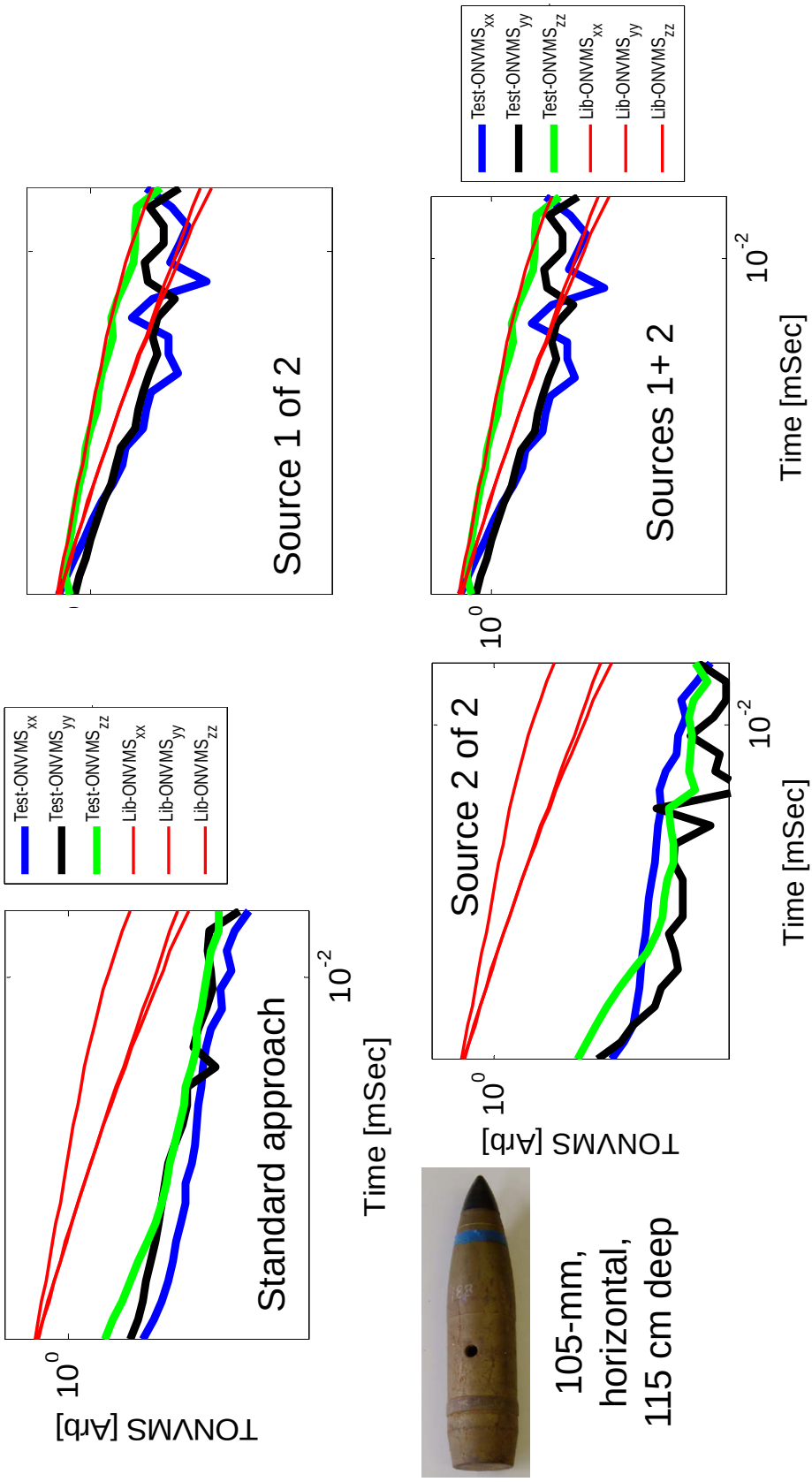

105-mm, horizontal, 115 cm deep

APG Results: Blind Grid – Complex Targets

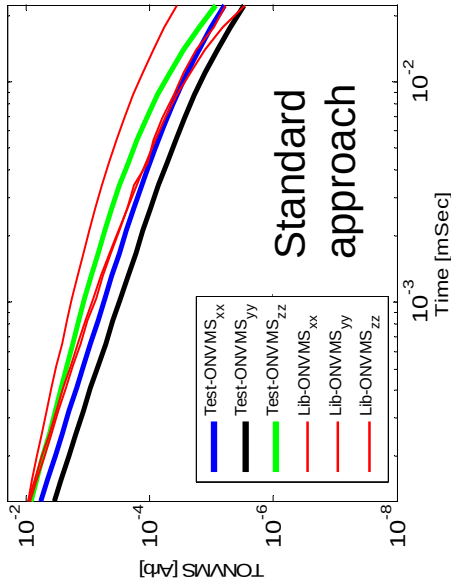

105-mm HR, horizontal, 30 cm deep

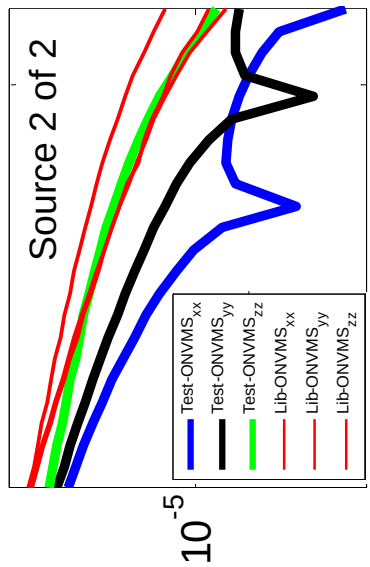

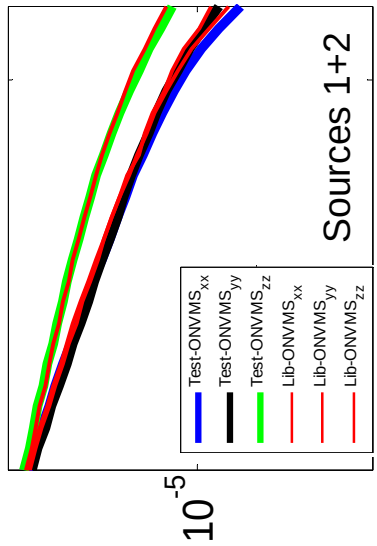

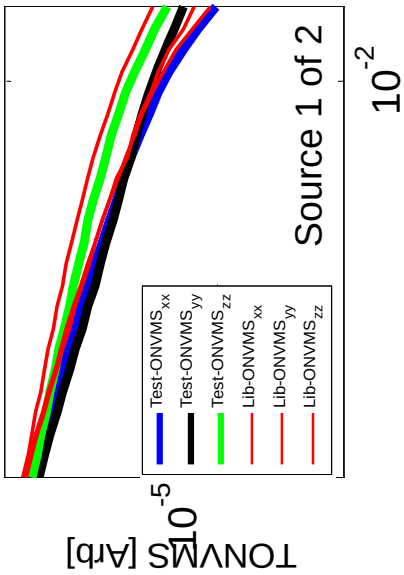

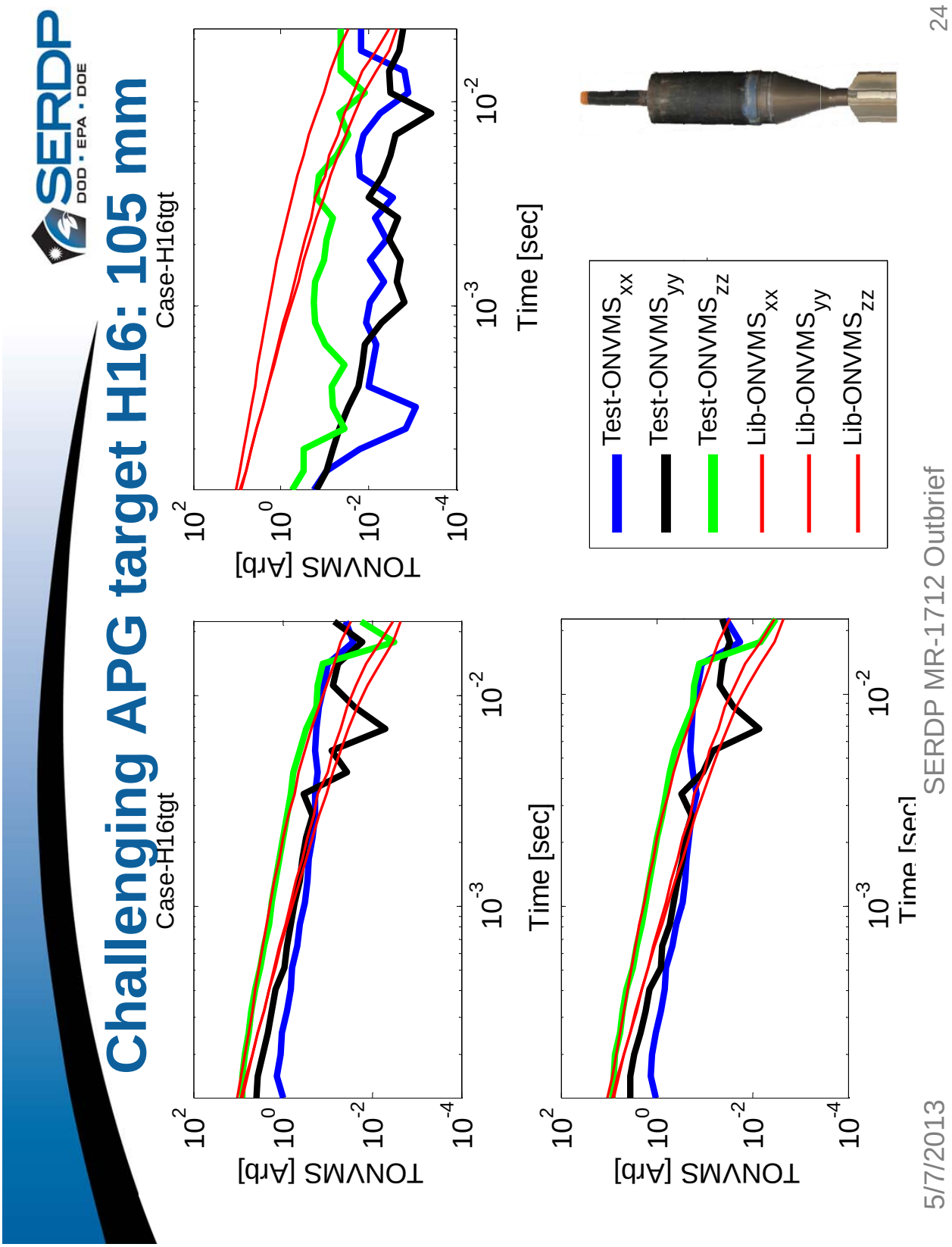
Challenging APG target H16: 105 mm
SERDP
DOD • EPA • DOE
Case-H16tgt
TONVMS [Arb]
Time [sec]
Test-ONVMS$_{xx}$
Test-ONVMS$_{yy}$
Test-ONVMS$_{zz}$
Lib-ONVMS$_{xx}$
Lib-ONVMS$_{yy}$
Lib-ONVMS$_{zz}$
5/7/2013
SERDP MR-1712 Outbrief
24

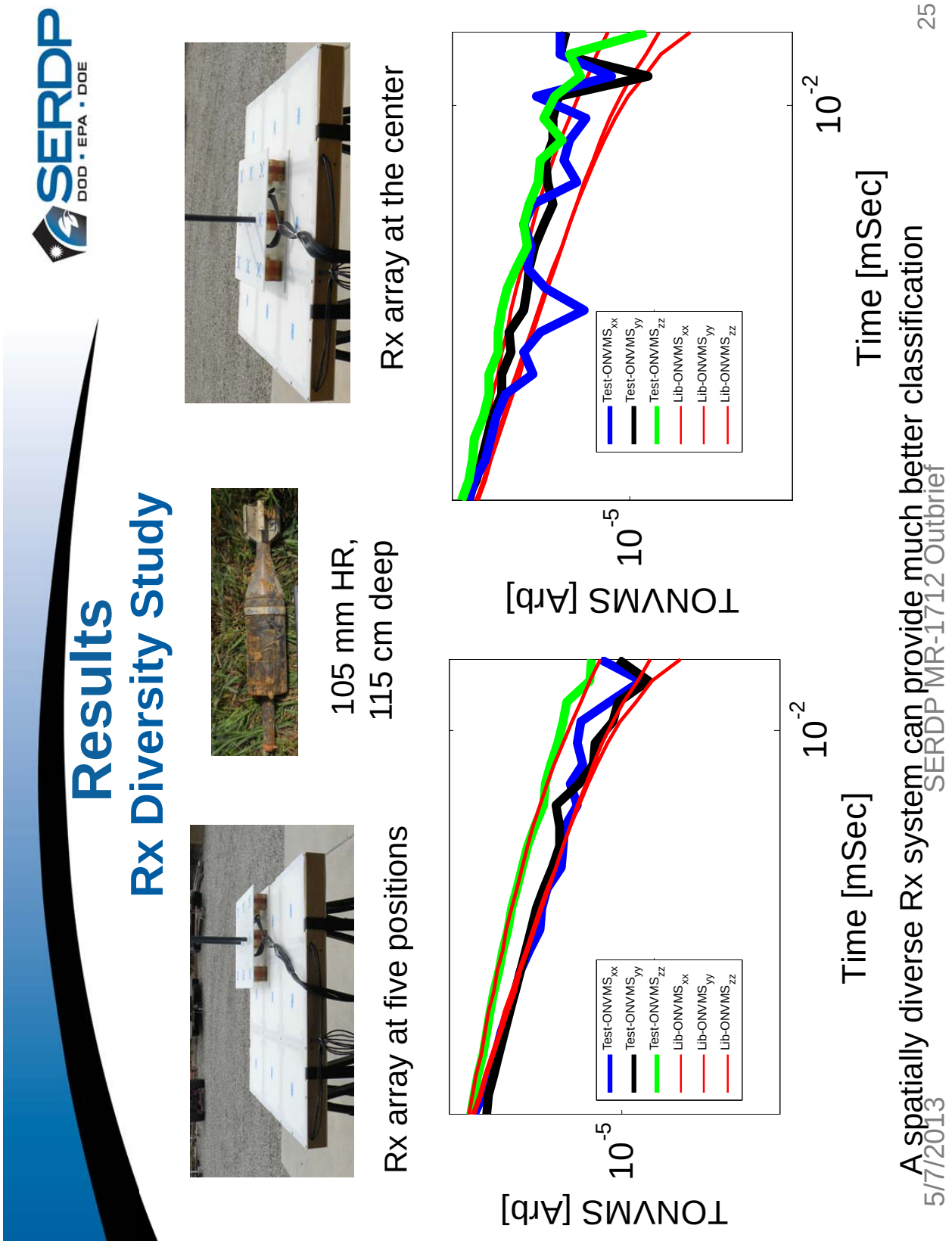
SERDP
DOD • EPA • DOE
Results
Rx Diversity Study
Rx array at five positions
105 mm HR,
115 cm deep
Rx array at the center
TONVMS [Arb]
10^{-5}
10^{-2}
Time [mSec]
Test-ONVMS$_{xx}$
Test-ONVMS$_{yy}$
Test-ONVMS$_{zz}$
Lib-ONVMS$_{xx}$
Lib-ONVMS$_{yy}$
Lib-ONVMS$_{zz}$
A spatially diverse Rx system can provide much better classification
5/7/2013
SERDP MR-1712 Outbrief
25

APG Results: Partial IDF Area

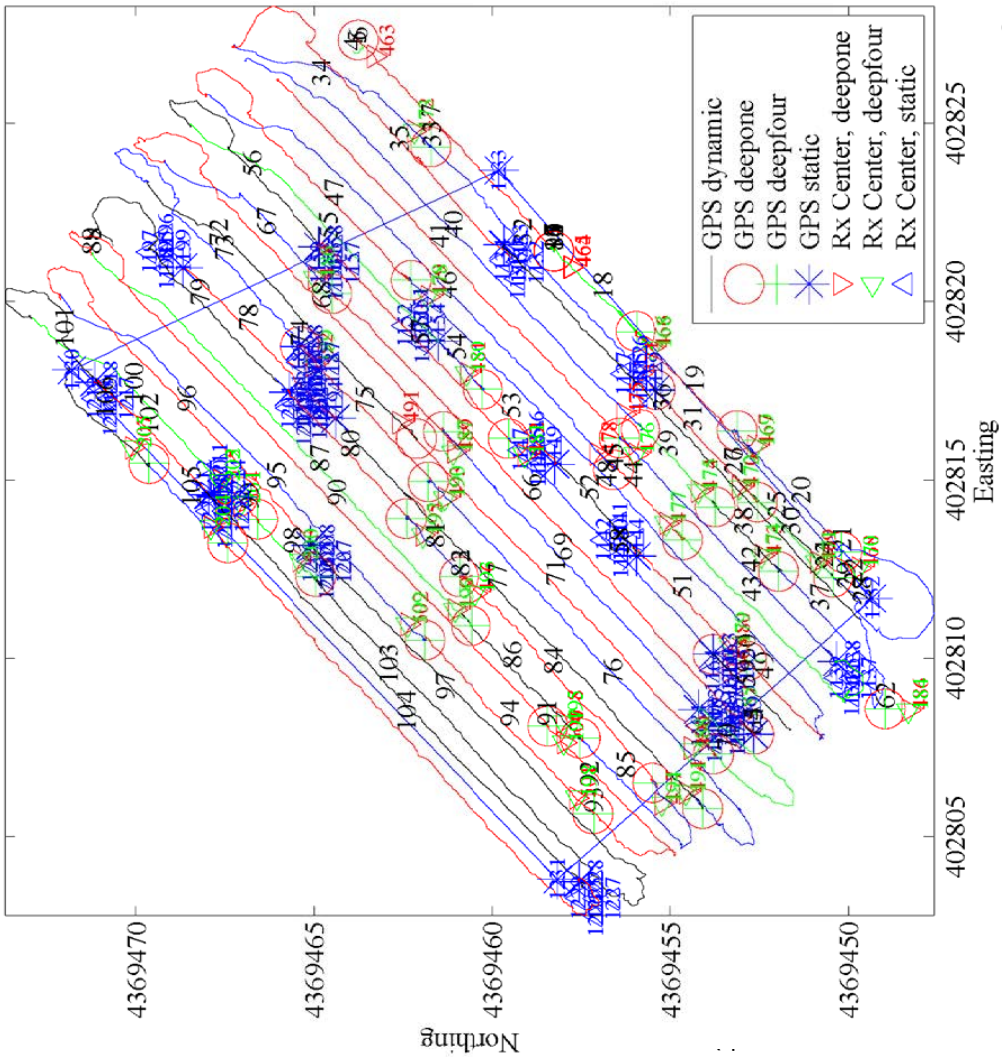

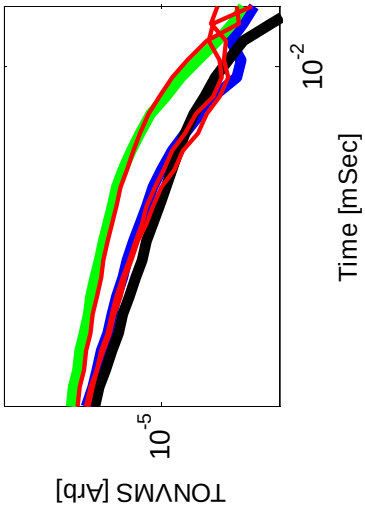

5/7/2013

APG Results: Partial Mogul Area (1 Mogul)

TABLE 8f. MOGUL CORRECT TYPE CLASSIFICATION OF TARGETS CORRECTLY DISCRIMINATED AS MUNITIONS (not covered)

Size	Percentage Correct
Small	(3 of 4) .75
Medium	(0 of 1)0
Large	NA
Overall	.60

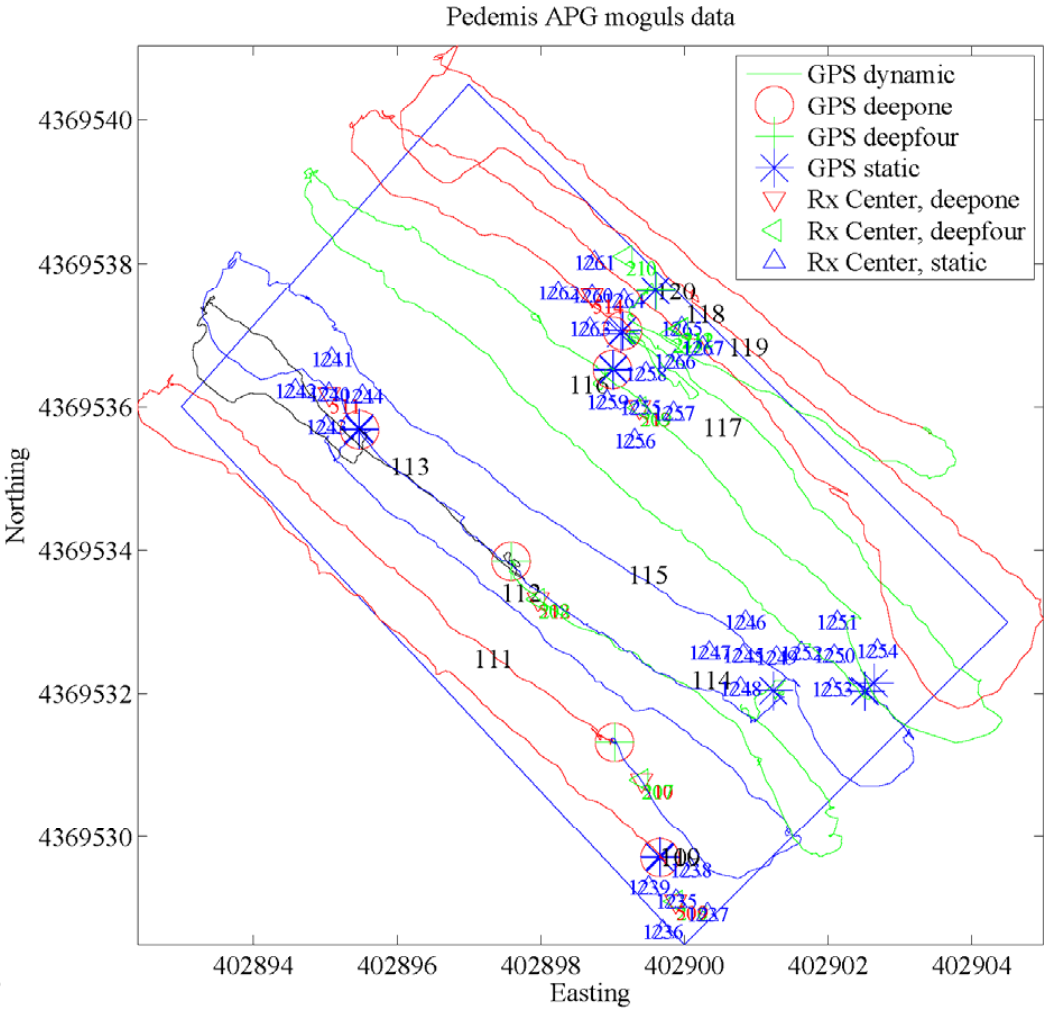

Conclusion: Pedemis Advantages

Pedemis – PortablE Decoupled ElectroMagnetic Induction Sensor

- Potential one pass solution
- Hardware
  - 2-person portable design
  - Flexible (2-person portable, carted, sledded)
  - 1.2x1.2m, 3x3 Tx, 3x3 vector Rx (compromise between 2 and 5)
  - decoupled Rx (data diversity, spatial coverage)
  - Lighter, updated electronics
  - Integral positioning system
  - GPS and digital compass
  - Wide swath width and spatial coverage (possible direct inversion of dynamic data)
- Software and processing
  - Real-time feedback to extpert operators (field plots, arrows, and JD)
  - Data suited to advanced models (JD, ONVMS, MUSIC)
  - Flexible DAQ modes (detection, interrogation, deep detection, wide interrogation)
  - EM3D or LabVIEW interface

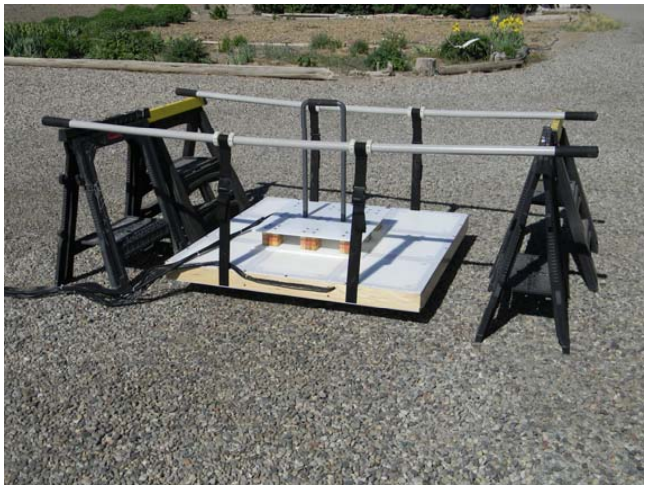

Conclusions and Summary

- Pedemis is fabricated and tested at APG
- Flexible deployment and operation options
- Portable, advanced EMI instr.
- Positioning system modeled and tested
- 3 x 3 planar Tx array
- 3 x 3 vector Rx array
- 1-4 minute cued DAQ sequence
- Advanced, real-time processing (JD and field plot)
- Lighter, more efficient hardware
- Same or better performance than carted systems
- Deployable at highly cluttered sites
- More easily deployed underwater
- Potential one pass solution
- Advanced models found all UXO at APG
- Built, tested, ready for live sites

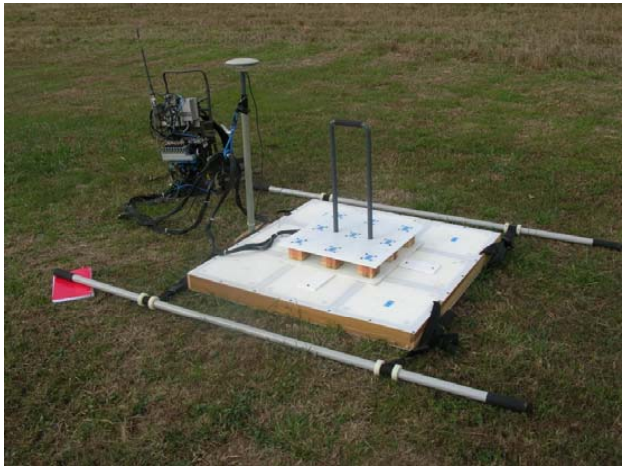

Follow-On Research

- Live site follow on including transition to production environment (ESTCP white paper under review)
- Modification of Pedemis to 3x3 in plane receivers
- Applying JD magnitude, ONVMS, and MUSIC algorithms to dynamic Pedemis data to reduce cued interrogations
- Incorporate MR-2225 results into Pedemis software
- Automate decision process without degradation (but expert review acceptable)

Possible Pedemis Modifications

3 × 3 3D PEDEMIS with fixed Rx
+ one 1.2 m × 1.2 m large loop

- Easy to modify and deploy
- Inexpensive
- Applicable for shallow and deep targets
- Good classification performance for up to 12 times the target diameter
- Decoupled configuration
  needs to be tested at challenging sites
- Can be reconfigured to
  Either configuration

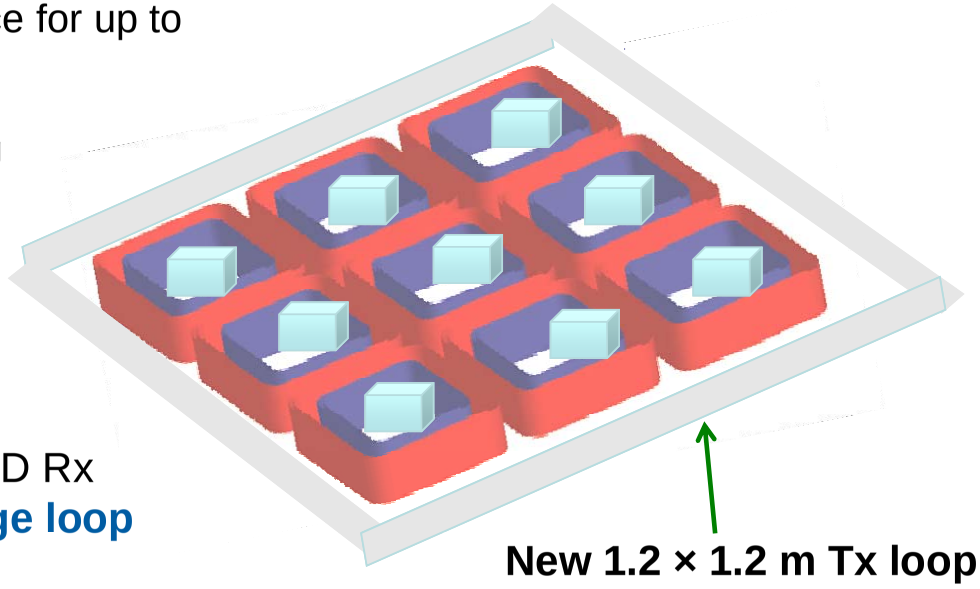

Modify PEDEMIS with fixed 3D Rx
+ one 1.2 m × 1.2 m large loop

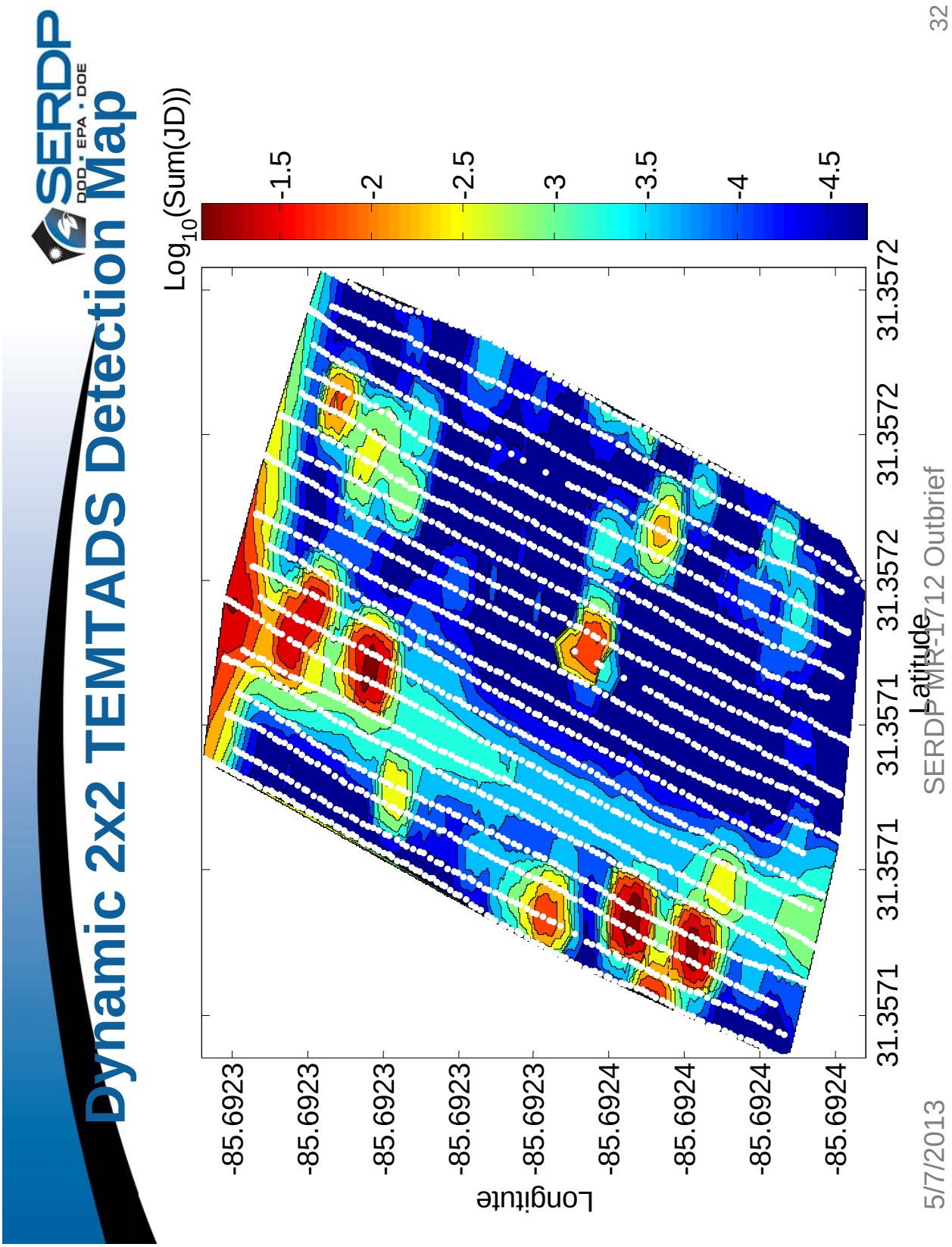
SERDP
DOD · EPA · DOE
Dynamic 2x2 TEMTADS Detection Map
Log10(Sum(JD))
-1.5
-2
-2.5
-3
-3.5
-4
-4.5
Longitude
-85.6923
-85.6923
-85.6923
-85.6923
-85.6923
-85.6924
-85.6924
-85.6924
-85.6924
Latitude
31.3571
31.3571
31.3571
31.3572
31.3572
31.3572
5/7/2013
SERDP MR-1712 Outbrief
32

Publications

- Operation of the Pedemis Sensor at the Aberdeen Proving Ground Standardized Test Site: Single and Multi-target inversions. TGRS Letters
- Oct 2011 A Man-Portable Vector Sensor for Identification of Unexploded Ordnance. IEEE Sensors
- May 1, 2012 Pedemis: a portable electromagnetic induction sensor with integrated positioning. SPIE 2012
- April 30, 2013 The Pedemis Instrument: positioning, background subtraction, and APG field results . SPIE 2013
- ONVMS APPLIED TO A NEW ADVANCED PORTABLE EMI SYSTEM DATA, DIPED, Tbilisi Georgia, September 23-25, 2012.
- April 30, 2013 Toward a real-time positioning system for a portable EMI sensor. SPIE 2013
- 04/2011 Rapid position estimation using electromagnetic induction data from the Metalmapper in dynamic mode. SPIE 2011